Politecnico di Torino

Politecnico di Torino

Master's Degree in Aerospace Engineering

A.a. 2025/2026

Graduation Session March 2026

Multidisciplinary design and optimization of a pressurized rover for lunar surface exploration

Supervisors:

Giuseppe Palaia

Rodolfo Azzara

Erasmo Carrera

Candidate:

Bruna Concetta Di Maggio

Abstract

This work presents the development of a multidisciplinary and parametric framework for the conceptual design and optimization of pressurized lunar rovers, aimed at supporting future human surface exploration missions. The implementation of rover subsystems requires a rigorous, physics-based approach that takes into account key performance factors across multiple disciplines, while also allowing for the flexible exploration of alternative designs. The proposed framework enables the sizing and preliminary evaluation of rover architectures starting from the definition of mission requirements, including the structuring of the operational timeline and the analysis of subsystem activation during different mission phases. From these inputs, the framework performs an iterative analysis using analytical and semi-empirical models, organized in a modular structure to facilitate both model extensibility and fidelity refinement. This allows for convergence between subsystem couplings and preserves the framework's scalability as additional disciplinary models are introduced or existing ones are refined. The model is designed to be mission-specific, as it can be applied to different requirements (e.g., crew size, mission days, etc.), making it a fully parametric tool for initial lunar rover studies. Thanks to these features, the framework allows for the evaluation of different mission scenarios and the quantification of the impact of design parameters on subsystem mass and power, integrating an optimization model aimed at at minimizing rover mass.

A mio padre.

Table of Contents

List of Tables

List of Figures

Glossary

DBMS
: Database Management System

ISRU
: In-Situ Resource Utilization

EVA
: Extra-Vehicular Activity

LRV
: Lunar Roving Vehicle

LIBS
: Laser-Induced Breakdown Spectroscopy

APXS
: Alpha Particle X-ray Spectrometer

NOMAD
: NASA Operational Mobile Autonomous Device

RATLER
: Robotic All Terrain Lunar Exploration Rover

LUR
: Light Utility Rover

DMLRV
: Dual Mode Lunar Roving Vehicle

MOLAB

Mobile Laboratory

RF

Rover first

SEV

Space Exploration Vehicle

PLR

Pressurized Lunar Rover

ISS

International Space Station

LC

Lunar Cruiser

RTG

Radioisotope Thermoelectric Generator

SCR

Solar Cosmic Rays

GCR

Galactic Cosmic Rays

MDO

Multidisciplinary Design Optimization

MLI

Multi-Layer Insulation

ECLSS

Environmental Control and Life Support System

CDRA

Carbon Dioxide Removal Assembly

CRS

Carbon Dioxide Reduction System

OGS

Oxygen Generator System

WPA

Water Processor Assembly

UPA

Urine Processor Assembly

LROC

Lunar Reconnaissance Orbiter Camera

PSR

Permanently Shadowed Regions

IMP

Irregular Mare Patches

SQP

Sequential Quadratic Programming

Chapter 1

Introduction

Renewed interest in crewed lunar exploration, driven by new NASA and ESA programs, is bringing the Moon back to the forefront of technological development for a sustainable human presence beyond low Earth orbit. In this context, surface mobility is a key enabling capability. Compared to previous lunar missions, future exploration architectures envision longer mission durations, more extensive traverses, and greater operational autonomy. Pressurized rovers represent the most promising solution for extended surface operations away from the habitat. However, their design constitutes a highly coupled problem: structure, power, thermal control, life support, and mobility subsystems are mutually dependent, and their interactions are strongly driven by mission requirements. The conceptual design phase is therefore crucial. However, the current literature still presents several methodological limitations. Existing studies and tools typically analyze rover subsystems separately, failing to provide a comprehensive multidisciplinary framework capable of capturing the interactions between them. As a result, the design process often lacks iterative convergence toward consistent mass budget, as well as optimization approaches capable of systematically exploring and identifying viable configurations already in the early design phases. This work addresses these gaps by developing a multidisciplinary and parametric framework for the conceptual design and optimization of pressurized lunar rovers. The proposed model adopts a multidisciplinary design methodology, commonly used in aeronautical engineering to manage tightly coupled systems within an integrated and iterative design environment. Starting from operational requirements, the framework:

- Structures the mission timeline and models subsystem activation across mission phases;
- Sizes the main subsystems using analytical and semi-empirical models;
- Iteratively manages disciplinary couplings until convergence of shared variables;

- Optimizes the configuration to minimize the overall rover mass.

The modular architecture allows the addition of new disciplines and the progressive refinement of model fidelity, making the tool suitable for the comparative evaluation of mission scenarios and for supporting the preliminary design of complex space systems.

1.1 Motivations and Context

Current international exploration architectures, particularly those associated with NASA's Artemis program and collaborations with partners such as ESA, JAXA, and the Canadian Space Agency, highlight the need for surface systems capable of supporting long-duration missions of increasing operational complexity. The Moon represents a unique natural laboratory for studying the origin and evolution of the Solar System and the Earth–Moon system, as its surface preserves geological and cosmochemical records that are inaccessible on Earth due to tectonic and erosional processes. Key scientific objectives, such as the study of lunar geology, the history of meteoritic impacts, and potential resources, require extended surface operations and versatile mobility, thereby justifying the development of pressurized rovers capable of supporting prolonged and autonomous missions [1]. The Artemis program envisions the establishment of a sustained human presence on the lunar surface through an incremental approach. Starting from the first crewed missions, the long-term goal is the development of the Artemis Base Camp at the lunar South Pole, a modular infrastructure that will progressively integrate habitats, power systems, communication infrastructure, and extended mobility capabilities. Within this architecture, pressurized rovers play a central role as mobile platforms capable of supporting long-duration exploration, scientific operations, and In-Situ Resource Utilization (ISRU) activities. ISRU refers to the extraction and processing of local materials such as water ice, oxygen, and metals, which can significantly reduce dependence on resupply from Earth and gradually shift surface operations toward a partially self-sustaining paradigm. The Moon also serves as an essential testbed for future human missions to Mars. While the Earth–Moon distance is approximately 400,000 km, Mars lies at an average distance of about 225 million km, making the recovery from potential surface system failures far more difficult. The Artemis program explicitly treats the lunar surface as a Mars-oriented analogue environment: missions are designed to test operations with small crews, surface stays of 30–45 days, and the autonomous capabilities that will be required on the Red Planet. The pressurized mobility platform is therefore conceived as a direct architectural precursor to the pressurized rover needed for Mars exploration. Consequently, the framework developed in this thesis has relevance beyond the lunar context, addressing requirements that are fundamentally shared between both

destinations [2]. To address these challenges, the design of a rover must coherently integrate multiple subsystems, including continuous life support, power and thermal management, radiation protection, and crew safety, while simultaneously meeting strict mass and power constraints. The framework developed in this thesis directly responds to these needs for autonomy and interdisciplinary integration, providing a tool for the conceptual design and optimization of pressurized rovers capable of meeting the operational requirements of modern exploration missions.

1.2 State of the art

1.2.1 Non-pressurized vs pressurized rover

Mobility systems represent a fundamental element for the exploration of the lunar surface, as they enable the operational range of missions to be extended and increase the scientific return. With a surface area of approximately 37.9 million km² and a wide variety of geological environments, including craters, basaltic plains, and polar regions, the Moon requires transportation systems that are reliable and adaptable to highly variable environmental conditions. From the perspective of pressurization, lunar rovers can be divided into two main categories. Non-pressurized rovers operate directly in the lunar vacuum environment: astronauts must wear a spacesuit while using the vehicle, or the system operates without a crew in teleoperated or autonomous mode. Pressurized rovers, on the other hand, are equipped with a sealed module maintained at controlled pressure, capable of hosting astronauts in a habitable environment or accommodating scientific instruments that require stable environmental conditions. Non-pressurized rovers can be further divided into two subcategories with different operational characteristics. Uncrewed robotic rovers can operate for months or even years without the physiological constraints associated with human presence. However, their scientific capabilities are limited by the Earth-Moon communication delay and by the difficulty of performing complex operations such as sampling or real-time geological interpretation. Crewed non-pressurized rovers, in contrast, allow astronauts to interact directly with the environment, but their operations are constrained by the duration of Extra-Vehicular Activity (EVA), typically between 6 and 8 hours, due to spacesuit autonomy, thermal management requirements, and physical fatigue [3]. This limitation significantly reduces the daily operational range and makes missions requiring prolonged stays far from the base difficult to accomplish. For long-duration missions combining human presence with extensive exploration, neither of these solutions is sufficient when considered independently. Crewed pressurized rovers have therefore been conceived to bridge this gap: the availability of a habitable internal environment allows the crew to travel, rest, and work without wearing a spacesuit, reserving EVA activities for tasks that require direct interaction with the environment, such as sampling or

instrument deployment. This approach significantly increases the time available for scientific activities and enables access to geologically interesting areas that would otherwise be unreachable within a single extravehicular activity.

Historic and Conceptual Unpressurized Lunar Rovers

The first mobility system used on the lunar surface was the Lunar Roving Vehicle (LRV), developed by NASA and employed during the Apollo 15, 16, and 17 missions between 1971 and 1972. The LRV remains the only crewed lunar rover to have operated directly on the Moon. Designed under strict mass and volume constraints to fit inside the Lunar Module, it featured a foldable aluminum-alloy structure that could be automatically deployed once extracted from the stowage compartment. In operational configuration, the LRV had a mass of approximately 210 kg and could carry two astronauts, scientific instruments, and geological samples for a total payload of about 490 kg. Propulsion was provided by four independent electric motors powered by non-rechargeable primary batteries, and the wheels were wire-mesh with titanium chevrons, ensuring traction on the lunar regolith. During Apollo 17, the rover reached a maximum speed of about 17 km/h and covered 20.1 km in a single traverse. However, the operational range was limited by the "walk-back" rule, which restricted travel to the distance astronauts could walk back in case of a vehicle failure, effectively limiting excursions to approximately 7.6 km from the Lunar Module. Despite these constraints, the LRV greatly enhanced scientific productivity, allowing Apollo 15 to collect 77 kg of geological samples and Apollo 16 to collect 97 kg. Its main limitation, however, was operational: all activities had to be performed in spacesuits during EVA, as the vehicle provided no environmental protection or autonomy beyond the duration of the EVA. [4] Building on the Apollo experience, several unpressurized rover concepts were proposed to support both robotic precursor missions and early crewed operations. Unmanned prototypes like NASA Operational Mobile Autonomous Device (NOMAD), developed by Carnegie Mellon University, demonstrated long-distance autonomous traversal in extreme terrestrial analogs such as the Atacama Desert and Antarctica. NOMAD's four-wheel drive and autonomous navigation enabled obstacle avoidance without human control, covering over 200 km in challenging terrain. Its limitations included small size, limited payload, and low operational speed (1.8 km/h), highlighting trade-offs inherent in compact autonomous designs. The Robotic All Terrain Lunar Exploration Rover (RATLER) family, developed by Sandia National Laboratories, explored lightweight, scalable, and highly maneuverable platforms for teleoperated tasks. Although versatile and capable of long-distance traversal, RATLER-class rovers lacked crew accommodation and were limited to robotic roles such as surveillance, material transport, or environmental monitoring. For early crewed missions, Boeing's Light Utility Rover (LUR) and the Dual Mode Lunar Roving

Vehicle (DMLRV) combined compactness with human transport capability. The LUR could support two astronauts for 8 hours, transporting equipment or materials, but short operational duration limited mission scope. The DMLRV extended the Apollo dual-use approach by adding a trailer for teleoperation after crew departure, powered by a radioisotope source to allow operation during the lunar night. Despite these improvements, limitations remained: partial radiation protection, modest cargo capacity, limited speed, and operational duration. [4] In summary, historic and conceptual unpressurized rovers excelled in simplicity, teleoperation, and early mission support, but were inherently limited in terms of crew protection, operational range, payload, and duration. These limitations clearly demonstrate the need for pressurized lunar rovers.

Pressurized Lunar Rover Concepts

Pressurized lunar rovers represent a crucial step toward sustainable and extended exploration of the Moon. By providing a mobile, shirt-sleeve environment, they allow astronauts to operate for prolonged periods while reducing reliance on extravehicular activity (EVA). Over the decades, several concepts have explored different approaches to balance crew safety, mobility, autonomy, and mission versatility. Early studies, such as NASA's Mobile Laboratory (MOLAB) in the 1960s and Boeing's Rover first (RF) in the 1990s, aimed to provide a compact, two-person habitat with short-term scientific capabilities. MOLAB laid the groundwork for mobile lunar laboratories, but it remained limited in range and flexibility. The Boeing RF, also called Rover First, introduced the innovative idea of landing directly on its wheels, eliminating the need for a separate lander and enabling teleoperated operations between crewed missions. However, its small size constrained crew capacity to two astronauts and limited operational range to about 80 km, making it suitable primarily for short sorties rather than extended exploration. In the early 1990s, the Virginia Tech/USRA studies advanced Pressurized Lunar Rover (PLR) design significantly. Their first concept featured a cylindrical module supported by six large wheels and a radioisotope power source, capable of carrying four astronauts for up to fourteen days with a nominal range of 500 km. While this design offered greater mobility and energy independence, the mass and complexity of the trailer system posed challenges for deployment and terrain negotiation. A second, dual-module concept incorporated a flexible tunnel connecting two pressurized cylinders, allowing articulated motion and improved adaptability to rough terrain. This configuration increased potential range to 2,000 km and operational versatility, but added structural complexity and weight, highlighting the trade-offs inherent in extending both capacity and autonomy. Later designs, such as the NASA Space Exploration Vehicle (SEV), focused on enhancing mobility and reducing EVA preparation time. The SEV introduced a twelve-wheel chassis

with independent and pivoting wheels, enabling lateral crab-style movements and improved maneuvering on steep terrain. Its suitport system allowed astronauts to don spacesuits directly from the vehicle in less than ten minutes, minimizing lunar dust contamination and reducing EVA setup time. The modular design allowed the pressurized cabin to detach from the mobility chassis and be used across different mission scenarios, including both surface exploration and in-space operations.[32] Most recent concepts, such as Toyota/JAXA's Lunar Cruiser (LC), demonstrate integration of lessons learned from earlier studies. With a pressurized cabin exceeding 13 m^2, fuel-cell energy systems, autonomous navigation for polar regions and the capacity to support two to four astronauts for weeks.[31]

Rover	Mission	Pr.	Crew	Mass (kg)	Range (km)	Speed (km/h)	Power system
Unpressurized							
Apollo LRV	Lunar	No	2	210	7.6	17	Primary batteries
NOMAD	Terr.	No	0	725	>200	1.8	Gasoline generator
RATLER	Lunar	No	0	–	–	–	Fuel cell
LUR	Lunar	No	2	984	–	–	Batteries/ Fuel cell
DMLRV	Lunar	No	2	–	–	–	RTG
Pressurized							
MOLAB / RF	Lunar	Yes	2	4300	80	1	Fuel cell
PLR v1	Lunar	Yes	4	6200	500	18	RTG
PLR v2	Lunar	Yes	4	7000	2000	29.4	Dynamic isotope system
SEV	Lunar	Yes	2-4	∼3000	>200	10	Fuel cell / Batteries
LC	Lunar	Yes	2-4	–	–	–	Fuel cell

Table 1.1: Summary of lunar rovers

1.3 Lunar environment

The Moon represents an environment radically different from that of Earth. Differences in fundamental physical characteristics such as gravity, atmosphere, temperature, and radiation directly determine the design requirements of any system intended to operate on the lunar surface. This chapter describes the main environmental factors relevant to the design of a pressurized lunar rover, with reference to data collected during the Apollo missions and to the consolidated technical literature.

1.3.1 Effects of Lunar Gravity

The lunar gravitational environment is characterized by an average gravitational acceleration of about $1.62\,\mathrm{m/s^2}$, corresponding to approximately one sixth of that on Earth. This condition significantly affects both the mechanical properties of the regolith, the granular material covering the lunar surface, and the interaction between the terrain and exploration vehicles. The lower gravitational acceleration influences the compaction state of the soil. Because particle weight is reduced, the vertical stresses within the ground are significantly lower than under terrestrial conditions. As a result, the regolith generally exhibits a more porous and less consolidated structure, which directly affects the way the soil responds to loads applied by vehicles and its bearing capacity during rover traversal. The reduced weight of a rover on the Moon also modifies the pressure transmitted to the ground. Although the lower load limits local soil compaction, it simultaneously decreases the normal force between the wheels and the terrain, a parameter that is fundamental for traction generation. Rover mobility therefore strongly depends on wheel–soil interaction. Under lunar conditions, the reduced normal force can limit traction and increase the likelihood of slipping, particularly on soft terrain or inclined surfaces. In addition, the granular nature of the regolith may promote wheel sinkage, potentially limiting the rover's ability to overcome obstacles or traverse slopes. Vehicle stability is also influenced by the low-gravity environment. While the rover's weight decreases, its mass remains unchanged and therefore its inertia is unaffected. During acceleration, braking, or steering maneuvers, the dynamic forces associated with motion may become relatively more significant compared to the force keeping the vehicle in contact with the ground. This can increase sensitivity to terrain irregularities and, in some cases, lead to partial loss of wheel–ground contact when negotiating obstacles. Understanding rover–regolith interaction under reduced-gravity conditions is therefore a key aspect in the design of mobility systems for lunar surface exploration.[5]

1.3.2 Temperature and Thermal Cycles

The thermal environment of the Moon is characterized by extremely wide variations in surface temperature, primarily due to the lack of a significant atmosphere and the long duration of the lunar day. In the absence of an atmosphere capable of distributing heat through convective processes or retaining thermal energy, the lunar surface experiences strong temperature fluctuations between the daytime and nighttime periods.

Measurements made during the Apollo missions, particularly at the Apollo 15 and Apollo 17 landing sites, provided direct data on surface temperatures. Maximum temperatures of approximately 374 K (about 101 °C) were recorded during the lunar day, while minimum temperatures reached around 92 K (−181 °C) at night. Comparable values had previously been estimated from Earth-based observations, which indicated maximum temperatures near 390 K and minimum temperatures around 104 K. Over the course of the lunar day, surface temperature can increase by about 280 K from the period immediately before sunrise to lunar noon. This heating is mainly due to direct solar radiation striking the surface without atmospheric attenuation. In addition, peak noon temperatures vary slightly over the year due to changes in the distance between the Moon and the Sun, with differences of a few kelvin between aphelion and perihelion. Surface temperatures also depend on latitude and local illumination conditions. Equatorial regions experience the most pronounced thermal excursions, whereas higher latitudes have lower average temperatures. In some permanently shadowed polar areas, such as deep craters near the poles, temperatures can drop to extremely low values on the order of a few tens of kelvin. An indicative estimate of surface temperatures in different lunar regions is reported in Table 1.2. The data highlight how temperatures can vary significantly between equatorial regions, illuminated polar areas, and permanently shadowed polar craters.

Location	Average temperature (K)	Monthly range (K)
Shadowed Craters	40	–
Other Polar Areas	220	±10
Equatorial Front	254	±140
Equatorial Back	256	±140
Equatorial Limb	255	±140
Mid-Latitudes	220–255	±110

Table 1.2: Estimated lunar surface temperatures in different regions

These extreme thermal cycles have a significant impact on surface materials and infrastructure intended for use on the Moon. The surface regolith, composed of very fine particles with a high surface-to-mass ratio, tends to heat up and cool down rapidly during the diurnal cycle, while larger rock blocks retain heat longer during the lunar night. From an engineering perspective, these extreme temperature fluctuations are therefore a critical factor in the design of systems for lunar exploration. Structures, electronic components and mobility systems must be designed to operate under conditions of severe thermal stress and to withstand repeated heating and cooling cycles throughout the long lunar days.[5]

1.3.3 Terrain and Regolith

The surface of the Moon has an extremely complex morphology, dominated by two main types of terrain: the highlands and the maria. The highlands represent the oldest regions of the lunar crust and are distinguished by a heavily cratered and irregular landscape characterised by mountain ranges, fault-block chains, hilly plains and areas crossed by systems of ridges and depressions. Elevations can exceed 2000 m above the surrounding plains, with local terrain inclinations reaching up to 40°. The *maria*, from the Latin for "seas", are basaltic plains formed by ancient volcanic eruptions that filled large impact basins, giving these regions a more uniform and relatively flat appearance, although still interrupted by craters, ejecta ridges and tectonic furrows. This morphological diversity directly affects the mobility of lunar rovers: common obstacles include impact craters, ejecta ridges, steep slopes and fields of boulders and debris. The ability to navigate autonomously and overcome such obstacles is therefore a fundamental requirement in the design of any mobility system intended for lunar exploration. The two terrain types also differ quantitatively and qualitatively. In the plains of the *maria*, visited by the Apollo 11 and Apollo 12 missions, impact structures range in diameter from a few decimetres to several hundred metres, with walls that are generally gentle and covered by fine soil. The main exception is the area surrounding younger craters, where concentrations of angular boulders are commonly observed. In contrast, the highlands exhibit a crater density two to three times higher than that of the *maria*, with structures reaching diameters of up to one kilometre and depths of 100–200 m. The walls of the most recent craters may reach inclinations of 40°–45°, often covered by loose material and scattered boulders, conditions that sometimes prevented rovers from approaching them during the Apollo missions. At higher elevations, mountain ranges are also present, typically characterised by average inclinations of 25°–30°, with local slopes exceeding 30°, as documented at the Apollo 15 and Apollo 17 landing sites.

The entire lunar surface is covered by a continuous layer of regolith, a granular material produced by billions of years of meteorite impacts. Grain sizes are highly

variable, with typical values ranging from 45 to 100 μm. The particles generally have irregular shapes, sharp edges and often contain a glassy component, characteristics that give the lunar soil abrasiveness. A critical factor for operations on the lunar surface is the finest fraction of this material: lunar dust. Its hazard is not only related to the extremely small grain size but also to its electrostatic behaviour. In the absence of an atmosphere, solar ultraviolet radiation generates electric charges on surface particles, which can mobilise the dust and cause it to move near the terminator, the boundary between illuminated and shadowed regions. The strong adhesion of this material to exposed surfaces has been documented quantitatively: measured values are approximately 10^4 dyn/cm^2 on painted surfaces and 2–3 $\times 10^3$ dyn/cm^2 on metal surfaces. These values indicate that once deposited, the particles are extremely difficult to remove by simple mechanical means and tend to penetrate deeper into fabrics and materials subjected to friction. Dust contamination can compromise the operation of moving mechanisms, degrade the optical properties of exposed surfaces and reduce the efficiency of thermal control systems such as radiators and low-emissivity coatings. For a pressurised rover, managing this phenomenon therefore represents a major engineering challenge, requiring dedicated solutions to protect mechanical, optical and thermal systems as well as to ensure crew safety.[5]

1.3.4 Meteorites

The Moon's surface is constantly bombarded by meteoroids, solid bodies of natural origin travelling through interplanetary space at extremely high speeds. In the absence of a protective atmosphere, even small particles strike the surface with sufficient energy to cause significant damage. Impact velocities near the Moon range between 13 and 18 km/s; meteoroids with a diameter of less than approximately 1 mm, commonly classified as micrometeorites, constitute the most frequent component of the flux. The meteorite flux is not uniform: small meteoroids (smaller than 1 μm) show an increase in frequency coming from the direction of the Sun, whilst larger ones (greater than 1 μm) arrive predominantly from the direction of the Earth's orbital motion. Consequently, the side of the Moon facing the direction of orbital motion is more exposed to the higher-energy meteoroids. From a protection perspective, a thickness of 2–3mm of resistant composite material is generally sufficient to shield against micrometeorites of milligram mass. Meteoroids of around one gram, on the other hand, can produce centimetre-scale craters, with a depth comparable to the diameter, and in brittle materials the fracturing may extend further, with possible damage to critical components. The probability of a meteoroid of this mass striking an astronaut during a year of cumulative extravehicular activity is very low, estimated at between 10^{-6} and 10^{-8}. For permanent or temporary lunar infrastructure, the overall risk depends on the exposed surface

area, the duration of the mission and the criticality of the components: whilst an impact on a large, inert structure may have limited consequences, the same event on a small life-support system could be catastrophic. To reduce the risk, protection systems can combine high-strength shielding materials, distributed layers of protection and redundancy of critical components, designed according to the layout of the base and the functions of each exposed element.[5]

1.3.5 Radiation Environment

The Moon is situated in an extremely hostile radiation environment, dominated by three main sources of ionising radiation: the solar wind, high-energy particles associated with solar flares Solar Cosmic Rays (SCR) and Galactic Cosmic Rays (GCR). The absence of a significant global magnetic field and a protective atmosphere means that the lunar surface is directly exposed to this radiation, without any form of natural shielding. The energies and fluxes of the particles striking the Moon span several orders of magnitude: from photons and ions in the solar wind at around 1 keV/nucleon, up to GCR particles with energies exceeding 10 GeV/nucleon.

The solar wind is a continuous flow of plasma (mainly protons and electrons) emitted from the solar corona at typical speeds of between 300 and 700 km/s and with proton fluxes generally ranging from 10^8 to 8×10^8 protons/cm$^2 \cdot$ s. Its energies are so low that it is stopped within the first micrometre of the lunar surface, thus posing no direct danger to astronauts or rovers; however, the solar wind is responsible for the sputtering erosion of the surface layers of regolith grains and represents the main source of volatile elements such as hydrogen, carbon, nitrogen and noble gases trapped in the upper layer of the lunar soil.

SCR, on the other hand, are high-energy particles accelerated during solar flares, which reach the Earth-Moon system within a timeframe ranging from a few minutes to a few hours after the event. Their danger is closely linked to solar activity: most events occur in the periods close to the peak of the 11-year cycle. SCR fluxes are highly variable: during periods of solar minimum they are practically absent, whilst in rare high-intensity events they can reach values many times higher than the galactic background. An astronaut exposed on the surface during one of these extreme events could receive a debilitating or lethal dose within a few days. The prediction of such events and the availability of an underground shelter reachable in approximately 30 minutes are considered essential requirements for long-duration human exploration.

GCR are high-energy particles originating from outside the solar system, with energies typically ranging from 0.1 to over 10 GeV/nucleon. Unlike SCR, GCR are a continuous and relatively predictable source: their flux varies over the solar cycle, with peak values reached during solar minimum periods, when the magnetic fields of the solar wind shield incoming galactic particles entering the solar system

less effectively. GCR are the most penetrating source: light nuclei, mainly protons and alpha particles, trigger cascades of secondary particles, particularly neutrons, which penetrate several metres deep into the regolith. Heavy nuclei are stopped within the first few centimetres, but locally induce very high radiation doses, visible as traces in lunar rock minerals and potentially harmful to sensitive electronic components.

From a protection standpoint, the solutions that can be adopted vary depending on the source. A shield of approximately 2 m of compact regolith (corresponding to approximately 400 g/cm^2) represents the minimum requirement for a lunar habitat; to ensure complete protection from rare solar events of maximum intensity, a thickness of approximately 3.5 m is required. For rovers, managing radiation risk means the need for continuous monitoring systems, shielding of critical electronic components, and planning routes that minimise exposure time during periods of high solar activity. Exposure to ionising radiation therefore represents one of the main design constraints for long-duration human missions, with implications for both the health of astronauts and the reliability of on-board systems.[5]

Chapter 2

Methodology

2.1 Iterative methodology and interdependence of subsystems

The methodology adopted for the rover's design is based on an iterative approach aimed at converging the overall mass of the system. The objective is to obtain a consistent estimate of the final mass, taking into account the main subsystems and their interactions. The design methodology adopted in this work follows a Multidisciplinary Design Optimization (MDO) approach inspired by aeronautical design philosophy [6], which is based on two key principles:

- Multidisciplinary approach, in which all subsystems such as structure, propulsion, life support systems, thermal control, mobility and energy are considered in an integrated manner;
- Use of different levels of fidelity, starting with simplified models for rapid assessments and moving on to more complex numerical models for detailed analyses;
- Integration of optimization within the iterative design process, enabling convergence toward an optimal configuration while satisfying multidisciplinary constraints.

It is important to emphasise that the design method adopted, while inspired by the typical approach of aeronautical engineering, must be appropriately adapted to the space context. In fact, the design concerns subsystems that may have functional similarities with those used in aeronautics, but which operate according to different physical principles or in profoundly different environmental conditions. The absence of atmosphere, the almost total vacuum, the high temperature variations and the reduced lunar gravitational acceleration substantially modify the design criteria.

In this context, the pressurisation of the habitable module is a design necessity directly imposed by the presence of the crew and the lunar environment. The impossibility of human survival in vacuum conditions requires the creation of a structure capable of guaranteeing a stable pressurised volume, sized not only with respect to the internal-external pressure differential, but also with respect to the mechanical loads associated with the launch phases and the stresses induced by motion on the lunar surface, although the latter are not analysed in this work. To enable the rover to move on the lunar surface, a mobility system has been designed, conceived as an electric all-wheel drive system with distributed actuation on the wheels. Its sizing is strongly influenced by the lunar environment, in particular by the reduced acceleration of gravity compared to that of Earth. The energy system has been designed to power the electric motors and all on-board subsystems, ensuring the operational autonomy required by the mission profile. The architecture adopted involves the use of solar panels for power generation in lighting conditions and batteries as a storage system. The type and duration of the mission determine the overall energy requirements and guide the sizing of both the storage system and the photovoltaic surface. Thermal control plays a critical role in the lunar environment, which is characterised by high temperature variations and the absence of convection. When there is a crew on board, the system must ensure conditions that are compatible with both the operation of the subsystems and the presence of humans inside the pressurised volume. The thermal management strategy is closely linked to the structural configuration, through the use of Multi-Layer Insulation (MLI) and the integration of radiant surfaces designed to dissipate the heat generated internally by the electronic subsystems, the crew and the residual dissipation of the multi-layer insulation.

Finally, the presence of astronauts on board for a certain period of time requires the design of a Environmental Control and Life Support System (ECLSS) capable of ensuring safe and continuous environmental conditions throughout the mission. This study considered two alternative configurations: a non-regenerative solution, based on the use of consumable resources stored on board, and a regenerative solution, obtained by adapting technologies and architectures derived from the ISS experience to the specific context of the lunar mission. The comparison between the two configurations highlights the impact in terms of mass, volume and power requirements. The joint analysis of these subsystems highlights how each of them cannot be sized independently but must be considered within an integrated design process. For this reason, the systemic approach adopted is particularly effective in the case of a pressurised lunar rover, as it allows us to:

- understand how each subsystem influences the others;
- quickly explore different design architectures before resorting to more detailed and computationally burdensome models;

- implement an iterative and consistent process until converging towards a balanced final configuration.

This study is part of the high-level preliminary design phase, during which it is essential to quickly explore different system architectures and evaluate design choices using physically based but computationally efficient models. This allows the most promising configurations to be identified before proceeding to more advanced design phases, characterised by high-fidelity models and greater engineering detail.

2.2 Iterative cycle

An initial estimate of the fixed mass is calculated outside the convergence cycle. This mass includes subsystems that depend mainly on the geometric characteristics of the rover, mission parameters and environmental conditions, such as the primary structure and the ECLSS. Added to these masses are those of the astronauts, space suits, scientific payload, avionics, cockpit, seats, floor, sleeping quarters, hygiene facilities and workstations. Once the fixed mass has been established, which serves as input for the iterative cycle, the relative tolerance threshold that will regulate the convergence criterion of the process is determined. Based on this estimate, the subsystems whose sizing depends on the rover mass are then dimensioned. The mobility system determines the traction forces and the corresponding power requirements as a function of the vehicle weight, which directly depends on the total rover mass. These power requirements propagate to the energy generation and storage system, which includes photovoltaic arrays and batteries sized according to the expected mission power profile. The active thermal control system is also dimensioned at this stage, with the required radiator area and associated mass calculated through an energy balance. Finally, the masses of all subsystems are summed to obtain an updated estimate of the total rover mass. Convergence is verified by comparing the relative variation between the updated mass and that of the previous estimate, defined as

$$\varepsilon = \frac{|M_{i+1} - M_i|}{M_i}$$

If the convergence condition is not satisfied, the updated mass is used as the new initial estimate and the iteration continues until the predefined tolerance or maximum number of iterations is reached. At the end of the cycle, once the convergence condition has been satisfied, the final values of the subsystems and the total mass are obtained

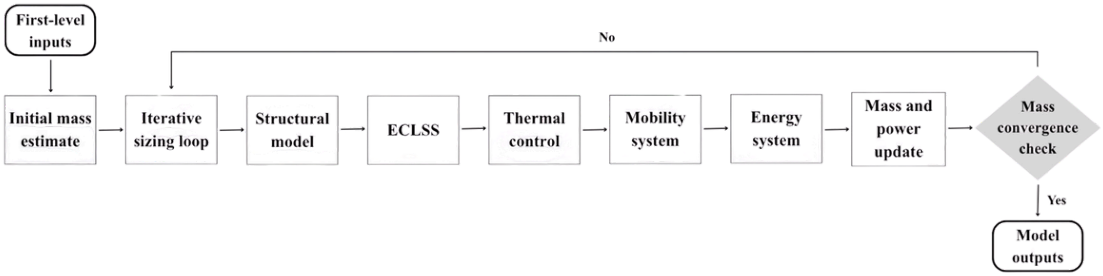

Figure 2.1: Flow diagram of the mass convergence cycle

2.3 Requirements, constraints and mission profile

The design of the pressurized rover is driven by a set of requirements derived from the mission objectives, the lunar environment, and the constraints imposed by human spaceflight standards. These requirements define the boundary conditions for the sizing of all subsystems and provide the reference framework for the subsequent design and optimisation phases. The requirements are organised into four categories. Operational requirements (Table 2.2) define the functional capabilities of the rover. Environmental requirements (Table 2.3) specify the external conditions the system must withstand. Performance and habitability requirements (Table 2.1 and 2.4) set the minimum standards for structural integrity, thermal control, and crew living conditions. Finally, energy requirements (Table 2.5) establish the constraints on the power and energy systems, with particular attention to eclipse conditions and emergency protocols.

ID	Requirement
R-PERF-01	The structure shall withstand a pressurization load P_{press}.
R-PERF-02	The thermal control system shall dissipate the mission-related heat loads.
R-PERF-03	The thermal control system shall maintain the internal rover temperature at $T_{\text{rover,int}}$ regardless of the external thermal environment, ensuring crew comfort and subsystem operability throughout the entire mission duration.
R-PERF-04	The ECLSS shall sustain crew life for the entire mission duration t_{mission}, sized for N_{crew} crew members.

Table 2.1: Performance requirements.

ID	Requirement
R-OP-01	The system shall enable scientific exploration of the lunar surface.
R-OP-02	The system shall support missions lasting t_{mission} on the lunar surface.
R-OP-04	The rover shall transport N_{crew} crew members in a pressurized environment.
R-OP-05	The rover shall carry a payload m_{payload}.
R-OP-06	The rover shall cover an average distance d_{av} per mission day, up to a maximum of d_{max} from the base.
R-OP-07	The rover shall achieve an average speed v_{avg} and a maximum speed v_{max} in emergency situations.
R-OP-08	The rover shall include N_{wheels} wheels with all-wheel drive.
R-OP-9	The rover shall support a minimum of N_{EVA} extravehicular activities, each lasting up to t_{EVA} hours.
R-OP-10	The rover shall be capable of returning to the base autonomously in emergency conditions, covering a distance of up to d_{max} at maximum speed v_{max} on battery power alone.
R-OP-11	The mobility system shall provide sufficient traction and driving force to navigate terrain slopes up to θ_{max} under lunar gravity conditions.

Table 2.2: Operational requirements.

ID	Requirement
R-ENV-01	The system shall operate in vacuum.
R-ENV-02	The system shall withstand lunar thermal excursions between $T_{\text{ext,cold}}$ and $T_{\text{ext,hot}}$.
R-ENV-04	The system shall operate under lunar gravity $g_{\text{moon}} = 1.62\ \text{m/s}^2$.
R-ENV-05	The outer shell shall provide protection against micrometeorite impacts consistent with the lunar surface flux environment.

Table 2.3: Environmental requirements.

ID	Requirement
R-HAB-01	The pressurised volume shall meet the minimum habitable volume per crew member.
R-HAB-02	The floor area shall provide a minimum usable surface of $A_{\min}$.
R-HAB-03	The clear height above the floor shall be at least 2 m over at least 75% of the usable floor area.

Table 2.4: Habitability requirements.

ID	Requirement
R-ENG-01	The primary power source shall provide continuous energy throughout the mission duration.
R-ENG-02	The energy storage system shall cover the rover's power needs in partial or total eclipse conditions.
R-ENG-03	The energy system shall be capable of supplying the rover's power requirements in emergency protocols.

Table 2.5: Energy requirements.

2.3.1 Mission Profile

The mission profile defines the temporal and operational division of the rover's activities. It has been designed as a typical 24-hour day, organised into a timeline that integrates all essential activities: sleep, driving, extravehicular activities and recharging stops. For a preliminary estimate, it is assumed that the phases have the same duration every day, thus making the daily cycle repeatable and simplifying the assessment of energy consumption. This structure allows human, energy and operational constraints to be met, as well as making power consumption estimable and consistent for the entire duration of the mission. In the model, the duration of the individual phases is a first-level input: some values are taken from references in the literature, while others depend on the operational context and are determined on the basis of additional parameters. The breakdown into phases is as follows:

- Sleep: this phase is dedicated to the psychophysiological recovery of the astronauts. The duration of this phase is set according to the guidelines of the *NASA-STD-3001, Vol. 1* standard [7], which provides for a dedicated interval of 8.5 hours;

- Driving: this involves moving the rover between pre-established waypoints. In this phase, energy requirements are dominated by the power required by the locomotion motors to overcome the resistance to the rover's movement on the ground, while the other subsystems contribute to a lesser extent. The duration of the phase depends on mission parameters, such as the average travel speed and the total distance to be covered in an operational day;

- EVA: this block represents the main fieldwork phase. The requirements of NASA document *EVA-EXP-0042* [8] show that xEVA suits have a capacity of up to 8 hours and the duration of the phase is typically planned for 6 ± 2 hours;[3]

- Rest/Recharge: this phase represents the moment of the operational day when the rover stops to restore the battery power consumed during the driving phase, depending on the available lighting conditions. At the same time, it is dedicated to the astronauts' activities, such as meals or other daily needs, thus integrating the energy and operational constraints of both the vehicle and the crew.

This preliminary and simplified breakdown of the mission profile allows for initial quantitative estimates of energy consumption and evaluation of the performance of the rover's main subsystems. It provides an initial operational framework that allows for the identification of any critical issues and the calibration of design parameters. In the subsequent phases of the study (Chapter 4), the mission profile will be further refined and managed through more complex and realistic operational scenarios that will allow various mission simulations to be carried out.

2.3.2 Mission parameters

This section lists the main mission parameters of the pressurised rover, organised into three main categories: operational, environmental and temporal. The operational parameters listed in Table 2.6 represent the functional capabilities of the rover during the mission, including mobility performance, travel range and transportable payload. The temporal parameters, summarised in Table 2.7, define the overall duration of the mission and the time relative to the individual operational phases. The environmental parameters, shown in Table 2.8, describe the thermal conditions inside and outside the rover. In particular, the external temperatures presented are those relating to extreme design cases, defined as hot case and cold case, which represent the most severe environmental conditions in terms of maximum and minimum thermal load present in the lunar environment, respectively. It is essential to define these two scenarios for the sizing of active and passive thermal control systems. The mission parameters represent the data that form the basis for

subsequent analyses, which are fundamental for energy sizing, operational planning and the design of the rover's subsystems.

Parameter	Symbol	Unit	Description
Number of astronauts	N_{crew}	-	Number of crew members.
Average speed	v_{avg}	km/h	Average speed of the rover during activities.
Maximum speed	v_{max}	km/h	Maximum speed in emergency situations.
Average range	d_{av}	km	Distance that can be covered in one mission day.
Payload mass	m_{payload}	kg	Payload carried by the rover.
Maximum range	d_{max}	kg	Maximum distance that can be reached from the base during the entire mission.

Table 2.6: Rover operating parameters

Parameter	Symbol	Unit	Description
Mission duration	t_{mission}	days	Total duration of the mission.
Hours of darkness	t_{eclipse}	h	Hours without sunlight during the mission.
Hours of driving	t_{guide}	h	Hours dedicated to the driving phase.
Hours of sleep	t_{sleep}	h	Hours dedicated to crew rest.
EVA hours	t_{EVA}	h	Hours dedicated to extravehicular activities.
Stop hours	t_{stop}	h	Remaining hours for stop activities.

Table 2.7: Mission time parameters

Parameter	Symbol	Unit	Description
External temperature (hot case)	$T_{\text{ext,hot}}$	K	External temperature in the hottest case.
External temperature (cold case)	$T_{\text{ext,cold}}$	K	External temperature in the coldest case.
Internal rover temperature	$T_{\text{rover,int}}$	K	Nominal internal temperature of the habitable volume.

Table 2.8: Mission environmental parameters

2.3.3 Subsystem status

The status of the subsystems is described in relation to the different operational phases into which the mission has been divided. The modes considered are as follows: *OFF* (subsystem off), *STBY* (subsystem in standby) and *ON* (subsystem active). The *Activity*×*Subsystems* matrix (Table 2.9) summarises, for each characteristic activity (Guiding, Resting, EVA and Sleeping), the operational status required for all subsystems. This formalisation forms the basis for estimating energy consumption and operational planning. In particular, *STBY* mode is a low-consumption mode in which energy consumption is assumed to be 30% of that in *ON* mode.

Activity	Locomotive	ECLSS	Comm	Thermal	Batteries	Panels
Driving	ON	ON	ON	ON	ON	OFF
Parking	OFF	ON	ON	ON	OFF	ON
EVA	OFF	STBY	ON	ON	OFF	ON
Sleep	OFF	ON	STBY	ON	OFF	ON

Table 2.9: Operating status of rover subsystems for each activity

In table 2.9, the *ON* and *STBY* modes relating to the locomotive system, the ECLSS, the communication system and the thermal control system indicate energy consumption. For the columns corresponding to batteries and solar panels, the *ON* mode indicates energy supply. In sunlight conditions, the batteries contribute to the energy supply exclusively during the driving phase. This constraint is linked to the fact that the solar panels, if fully deployed during movement, would have to withstand significant structural loads due to acceleration, vibrations and mechanical stresses generated by the rover on uneven terrain, which could compromise their

integrity. For this reason, during the driving phase, the solar panels are considered folded, and power is supplied by the batteries. During other operational phases, in the presence of sunlight, the solar panels can be deployed and supply power to the rover's subsystems. The matrix shown therefore represents an optimal lighting scenario. In the absence of light (night-time or shaded areas), the batteries must guarantee the supply of energy to all subsystems for all phases of the mission, ensuring the continuous operation of the rover even in the absence of solar radiation.

2.4 System design

The architecture of the pressurised rover is based on a set of interdependent subsystems, each with a specific function. This subdivision allows the project to be managed in a modular manner, making it possible to modify or refine individual subsystems without compromising the entire structure of the vehicle.[9] Each subsystem is designed based on a set of characteristic parameters that make the entire model parametric, allowing different rover configurations to be analysed and compared. These parameters, together with the mission parameters, constitute the inputs for the sizing models of the individual subsystems, allowing for a flexible and scalable design process. The rover's organisation includes the following main subsystems:

- Locomotive system;
- Structure
- Energy system
- Environmental support system
- Thermal control system

The simulation and design environment was developed in MATLAB. In the implemented model, each subsystem is represented by an independent MATLAB function called within the main routine. The primary outputs of these models are the subsystem mass and the corresponding power requirements. These quantities allow the local performance of each module to be evaluated while also providing the key inputs for the iterative convergence of the rover total mass. The criteria and procedures adopted in the development of the individual functions are described in the following sections, together with the characteristic parameters used as inputs for the sizing models. This structure highlights the design methodology and illustrates how each subsystem contributes to the overall architecture and performance of the vehicle. The quantitative and qualitative results are obtained from a reference mission whose main parameters are reported in Table 2.10. To

verify the reliability of the models, several design parameters were systematically varied, enabling parametric analyses. This process allows us to assess the system's sensitivity to variations in the main parameters, identify potential limitations or unexpected behaviors, and provide a clearer assessment of the robustness and expected performance of the subsystems.

Operating Parameters

Parameter	Symbol	Value	Unit
Number of astronauts	N_{crew}	2	–
Average speed	v_{avg}	10	km/h
Maximum speed	v_{max}	15	km/h
Average distance	d_{avg}	20	km
Maximum mission distance	d_{max}	50	km
Payload	m_{payload}	300	kg

Environmental Parameters

Parameter	Symbol	Value	Unit
External temperature (hot case)	$T_{\text{ext,hot}}$	294	K
External temperature (cold case)	$T_{\text{ext,cold}}$	40	K
Internal rover temperature	T_{int}	293.15	K

Time Parameters

Parameter	Symbol	Value	Unit
Mission duration	t_{mission}	14	days
Hours of darkness	t_{dark}	0	h
Driving hours	t_{drive}	2	h
Sleeping hours	t_{sleep}	8	h
EVA hours	t_{EVA}	6	h
Stop hours	t_{stop}	8	h

Mobility System Parameters

Parameter	Symbol	Value	Unit
Number of wheels	N_{wheels}	4	–
Wheel diameter	D	1.2	m
Wheel thickness	b	0.5	m

Structural Parameters

Parameter	Symbol	Value	Unit
Rover radius	R_{rover}	2	m
Rover length	L_{rover}	$f(V, R)$	m
MLI layer thickness	t_{MLI}	1.6×10^{-4}	m
External shield thickness	t_{shield}	2×10^{-3}	m
Pressurisation load	P_{press}	0.1013	MPa
Structure material	–	Al 7075-T73	–
Material density	ρ_{mat}	2800	kg/m^3

Terrain Parameters

Parameter	Symbol	Value	Unit
Terrain type	–	Flat	–
Slope	θ	0	deg

Energy System Parameters

Parameter	Symbol	Value	Unit
Cell capacity	C_{cell}	3.5	Ah
Nominal cell voltage	V_{cell}	3.6	V
Bus voltage	V_{bus}	120	V
Battery energy density	E_{dens}	259	Wh/kg

Thermal Control Parameters

Parameter	Symbol	Value	Unit
Main fluid flow rate	$\dot{m}_f$	0.8	kg/s
Specific heat	c_p	4200	J/kgK
Fluid density	ρ_f	1050	kg/m^3
Loop inlet temperature	T_{in}	296	K
Radiator emissivity	ε_{rad}	0.97	–

Table 2.10: Parameters for the example mission

By evaluating the operation of the individual subsystems in the different mission phases and calculating the power required by each of them, according to the reference mission reported in Table 2.10, it is possible to obtain the power profile associated with the individual operational phases over a 24-hour day, shown in Figure 2.2.

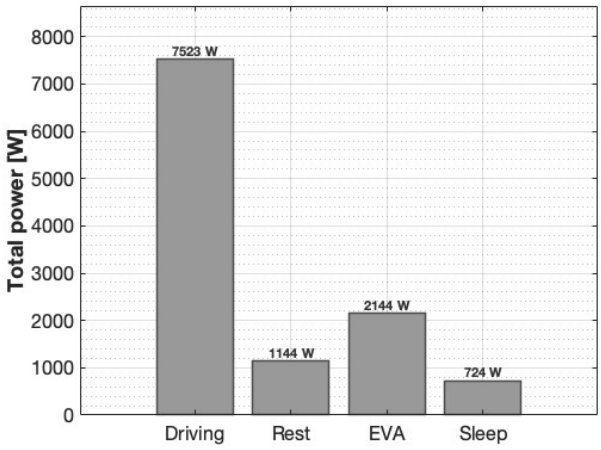

Figure 2.2: Power profile for a standard mission day

It can be seen that the phase in which the rover requires the most power is driving, while the least energy-intensive phase is sleep, when overall consumption is minimal. This profile highlights the variations in energy requirements throughout the day and allows batteries and solar panels to be sized appropriately to cover the most critical phases of the mission.

2.4.1 Locomotive system

The mobility system defines the vehicle's ability to move safely and efficiently on the lunar terrain. It is designed to provide the driving force necessary for the rover to move forward, as well as stability and safety while driving. The model was developed using a parametric approach based on physical models of terra-mechanics [10], which allows the effect of the main geometric and dynamic parameters on energy consumption and total system weight to be analysed.
The model is based on a set of simplifying assumptions. It is assumed that the static load is distributed evenly among the wheels, that the mechanical properties of the ground are homogeneous and isotropic over the entire surface considered, that the wheel can be modelled as smooth, and that the motion occurs at constant speed. These assumptions reduce the complexity of the problem while ensuring a realistic description of the behaviour of the locomotive system in the preliminary design phase. The model also assumes that all wheels are driven and actively contribute to the generation of traction. Consequently, each wheel is powered by its own dedicated electric motor, a configuration that allows for uniform power distribution. The characteristic parameters of the ground used in the model are listed in Table 2.11 and are derived from classical studies of lunar soil.[5]

Symbol	Parameter	Unit
c_{rr}	Rolling resistance coefficient	-
ϕ	Angle of inertial friction	rad
k_c	Soil cohesion modulus	$\mathrm{N/m^2}$
k_θ	Soil friction modulus	$\mathrm{N/m^3}$
K_c	Soil deformation cohesion modulus	-
K_g	Soil deformation density modulus	-
c	Soil cohesion	$\mathrm{N/m^2}$
γ	Soil weight density	$\mathrm{N/m^3}$
n	Settlement law exponent (Bekker)	-

Table 2.11: Mechanical and geometric parameters of lunar soil

The wheel–soil interaction model adopted is based on the representation of the ground as a non-linear spring, according to the classical formulation of soil mechanics introduced by Bekker. In this approach, the soil reacts to wheel penetration by producing a vertical pressure proportional to the sinkage z:

$$W_{\mathrm{wheel}} = \frac{W}{N_{\mathrm{wheels}}} \tag{2.1}$$

$$P = \frac{W_{\mathrm{wheel}}}{A} = kz^n \tag{2.2}$$

$$k = \frac{k_c}{b} + k_\phi \tag{2.3}$$

where W_{wheel} is the weight acting on a single wheel, P is the applied pressure and A is the contact area between the wheel and the ground. Combining Equation 2.2 and 2.3, we obtain:

$$P = \left(\frac{k_c}{b} + k_\phi\right) z^n \tag{2.4}$$

Resistances acting on the rover

To ensure the rover's forward motion, the locomotive system must be designed to generate a traction force at least equal to the sum of all resistive contributions due to the interaction between the wheel and the ground and the slope of the terrain. In accordance with the adopted soil mechanics model, the resistances acting on the rover include:

1. Soil compression resistance R_{c},

2. Bulldozing resistance R_{b},
3. Rolling resistance R_{r},
4. Gravitational component along the slope R_{g}

Therefore, the total resistive force can be expressed as:

$$R_{\mathrm{tot}} = R_{\mathrm{c}} + R_{\mathrm{b}} + R_{\mathrm{r}} + R_{\mathrm{g}} \tag{2.5}$$

Soil compression resistance

The soil compression resistance R_c represents the force required to compress the soil under the vertical load of the wheel. This resistance depends directly on the sinking z, the mechanical properties of the soil and the size of the wheel. The compression resistance for each wheel can be calculated using the following equation:

$$R_{c,\ \mathrm{wheel}} = 0.85854 \cdot \left(\frac{W_{\mathrm{wheel}}^4}{(k_c + bk_\theta)D^2} \right)^{\frac{1}{3}} \tag{2.6}$$

The total compression resistance of the rover is given by:

$$R_{\mathrm{c}} = N_{\mathrm{wheels}} \cdot R_{c,\ \mathrm{wheel}}, \tag{2.7}$$

Bulldozing resistance

The bulldozing resistance R_{b} arises from the accumulation and displacement of regolith in front of the wheel during motion. The resistance per wheel can be expressed as:

$$\begin{aligned} R_{\mathrm{b,\ wheel}} = {} & \frac{b\,\sin(\alpha+\phi)}{2\,\sin(\alpha)\,\cos(\phi)} \Big(2z\,c\,K_c + \gamma\,z^2 K_g \Big) + \frac{\gamma\,l_0^3}{3} \left(\frac{\pi}{2} - \phi \right) \\ & + c\,l_0^2 \left(1 + \tan\left(\frac{\pi}{4} + \frac{\phi}{2} \right) \right) \end{aligned} \tag{2.8}$$

where

$$\alpha = \arccos(1 - 2z/D), \quad l_0 = z\,\tan^2\left(\frac{\pi}{4} - \frac{\phi}{2} \right) \tag{2.9}$$

The total contribution is obtained by summing the contributions of the front wheels, which are most affected by the phenomenon of ground thrust.

$$R_{\mathrm{b}} = N_{\mathrm{front}} \cdot R_{\mathrm{b,\ wheel}} \tag{2.10}$$

where N_{front} is the number of front wheels.

Rolling resistance

Rolling resistance R_{r} represents a simplified model of energy losses due to the cyclic deformation of the ground and the wheel during motion. It can be calculated using the following equation:

$$R_{\mathrm{r}} = c_{\mathrm{rr}}\, W\, \cos(\theta) \tag{2.11}$$

where θ is the angle of inclination of the ground.

Gravitational resistance

Gravitational resistance R_{g} is due to the component of the rover's weight along the direction of motion when the vehicle is on a slope. It can be calculated using the following equation:

$$R_{\mathrm{g}} = W\, \sin(\theta) \tag{2.12}$$

Electrical power and mass of the system

To keep the rover moving at a constant speed, the locomotive system must provide sufficient mechanical power to overcome all the resistive forces opposing its forward motion. The mechanical power required can be expressed as:

$$P_{\mathrm{mecc}} = R_{\mathrm{tot}} \cdot v \tag{2.13}$$

where R_{tot} represents the total resistive force, obtained as the sum of the individual resistances (Equation 2.5) and v is the constant speed of the rover. To determine the electrical power required from the power supply system, the efficiencies of the main drive-train components must be taken into account, as illustrated in the powertrain diagram in Figure 2.3.

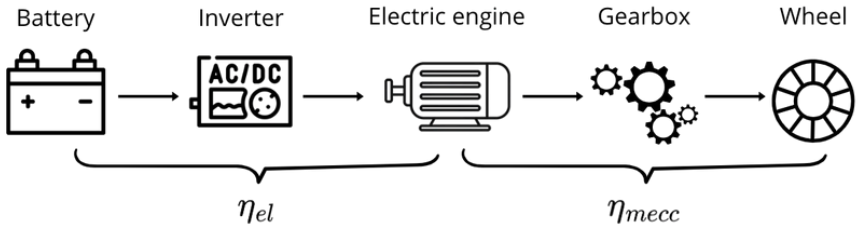

Figure 2.3: Powertrain diagram

In particular, two efficiency terms are considered: the electrical efficiency η_{el}, associated with losses along the battery-inverter-motor path, and the mechanical efficiency η_{mecc}, which accounts for the losses in the motor-reduction-wheel transmission chain. These losses reduce the power effectively available at the wheel.

Therefore, denoting by P_{mecc} the mechanical power required for vehicle motion, the electrical power supplied by the battery can be written as:

$$P_{\text{el}} = \frac{P_{\text{mecc}}}{\eta_{\text{el}} \cdot \eta_{\text{mecc}}} \tag{2.14}$$

where η_{el} and η_{mecc} represent the electrical and mechanical efficiencies defined above.

Once the electrical power required for motion has been determined, the next step is to calculate the mass of the entire locomotive system. The sizing of the motors in terms of mass is based on the specific power, which represents the amount of power available per unit of motor mass. In particular, the mass of each motor can be estimated using the following equation:

$$m_{\text{motors}} = \frac{P_{\text{mecc}}}{p_{\text{spec}}} \tag{2.15}$$

The mass of the wheels was estimated by analogy with those of the Lunar Roving Vehicle used in the Apollo 15 and Apollo 17 missions, taking as a reference the equivalent volumetric density ρ_{eq}, defined as the ratio between the total mass of the wheel and its external geometric volume.[11] These wheels had a lattice structure made of high-strength harmonic steel wires, without conventional tyres. The volume was calculated as a cylinder with a diameter and thickness relative to those of the wheel. The total mass of the wheels can therefore be calculated as:

$$m_{\text{wheels}} = N_{\text{wheels}} \cdot V_{\text{wheel}} \cdot \rho_{\text{eq}} \tag{2.16}$$

where V_{wheel} is the geometric volume of a single wheel. An additional contribution due to the chassis and mechanical elements directly connected to the single locomotive unit is added, considering a percentage analogy with already existing rover projects.[12][9]

Results

The results in Figure 2.4 illustrate the influence of the number of wheels on both the total mass of the mobility system and the electrical power required for motion. As expected, increasing the number of wheels leads to a higher mass of the mobility subsystem. From an energy perspective, one might expect the power requirement to increase as a consequence of the higher vehicle mass. However, the analysis reveals the opposite trend: the electrical power decreases as the number of wheels increases. This behaviour can be explained by the reduction in ground pressure due to the distribution of the vehicle load over a larger contact area, which results in lower mechanical resistance to motion.

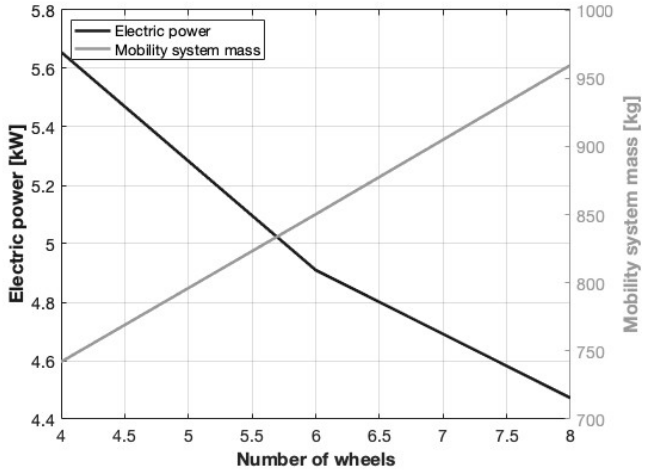

Figure 2.4: Influence of the number of wheels on the mass and electrical power required by the locomotive system

Figure 2.5 illustrates how the electrical power required by the rover changes with the geometric characteristics of the wheels, particularly diameter and thickness. In the model, these parameters directly influence the wheel sinking into the ground and the main resistances to motion, affecting the overall power demand. Increasing the wheel diameter generally reduces sinking z because a larger wheel spreads the load over a greater contact area, lowering the average contact pressure and, consequently, the force needed to deform the soil. This also leads to a reduction in bulldozing resistance, as less soil is mobilized in front of the wheel. Wheel thickness affects resistance in two ways: by increasing the contact width with the soil and by slightly influencing wheel sinkage. There exists an optimal combination of diameter and thickness that minimizes these resistive forces and, consequently, the electrical power required to move the rover. Figure 2.5 illustrates how power varies with changes in wheel geometry.

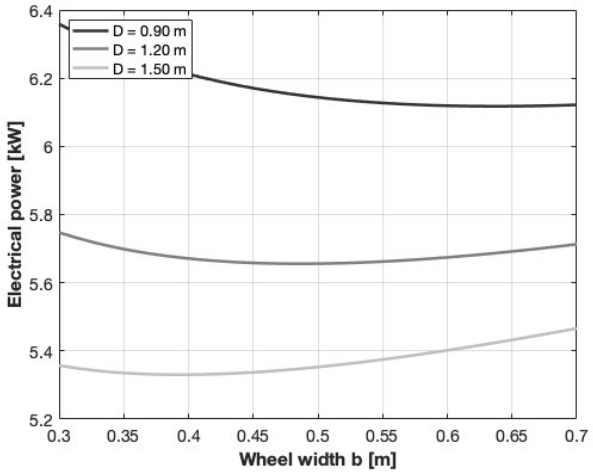

Figure 2.5: Influence of wheel geometric parameters on the electrical power required by the locomotive system

Finally, the values of the resistive components shown in Figure 2.6a indicate that gravitational resistance increases rapidly with terrain slope. As the inclination grows, this component eventually exceeds the terramechanical resistances, identifying an operational threshold beyond which rover motion becomes strongly penalized by the gravitational contribution.

This behaviour is further highlighted in the percentage analysis reported in Figure 2.6b, where the relative contribution of gravitational resistance progressively dominates as the slope increases.

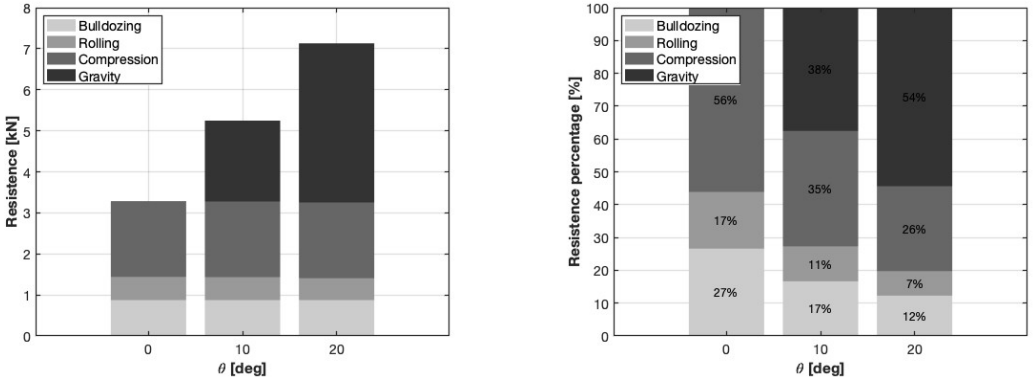

(a) **(b)**

Figure 2.6: Breakdown of resistances and evaluation of percentage contributions

2.4.2 Structure

The structural design of the pressurised rover is a fundamental element in ensuring the integrity of the habitable volume and the protection of the crew. Throughout the vehicle's entire life cycle, from launch to operations on the lunar surface, the rover is subject to various structural loads, the most severe of which occur inside the launcher. In this work, however, the analysis will be limited to the loads resulting from the pressurisation of the module, neglecting the others. The structure studied is divided into:

- Pressurised shell: this constitutes the main structure of the habitable volume and maintains the integrity of the cabin, allowing it to sustain the internal pressure necessary for the crew's life. The pressurised shell represents the inner layer of the structure and its thickness is dimensioned using a simplified analytical approach based on the theory of thin pressurised shells, which allows the estimation of the principal stresses, thicknesses and, consequently, the overall mass of the structure;[13]

- MLI: serves to thermally insulate the module, reducing the heat flow between the external environment and the pressurised interior. The thickness was determined based on the sizing of the passive thermal system to ensure adequate protection against extreme temperature variations on the lunar surface (Section 2.4.5);

- External anti-micrometeorite protection: this is the outer layer of the structure and is made of aluminium. It adopts the typical configuration of space systems, known as *Whipple Shield*, consisting of two aluminium walls separated by a cavity. This protection fragments micrometeorites on impact and disperses kinetic energy, significantly reducing damage to the rover's primary structure.

The volume considered is that of a thin-walled cylinder with two hemispherical caps at the ends. The structure is made of 7075-T73 aluminium alloy. [14] This alloy has been widely used in aerospace, particularly for the construction of pressurised modules.

Calculation of the Rover Pressurised and Habitable Volume

The habitable volume of the rover was estimated using an empirical–comparative method commonly adopted during preliminary design phases. The approach is based on the analysis of historical crewed spacecraft and habitats developed by NASA (Figure 2.7) [15].

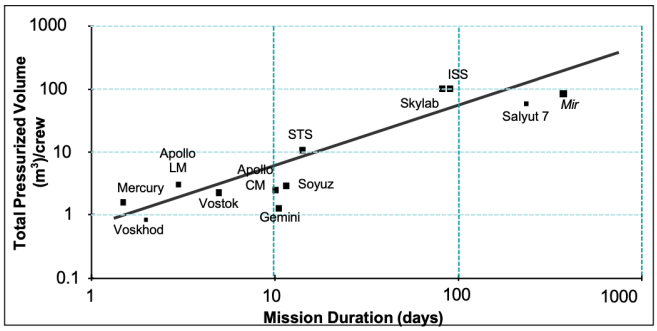

Figure 2.7: Pressurised volume of historic NASA spacecraft.

Based on the analysis of historical missions and terrestrial analogues, an empirical relationship can be derived to estimate the pressurised volume per crew member as a function of mission duration. The logarithmic trend identified for crewed habitats can be expressed as

$$V_{\text{press,crew}} = 6.67 \cdot \ln(\text{duration [days]}) - 7.79 \tag{2.17}$$

The total pressurised volume of the rover is therefore obtained as

$$V_{\text{press}} = N_{\text{crew}} \cdot V_{\text{press,crew}} \tag{2.18}$$

However, not all the pressurised volume is directly usable by the crew. In this work the habitable volume is assumed to correspond to 75% of the total pressurised volume:

$$V_{\text{hab}} = 0.75\, V_{\text{press}} \tag{2.19}$$

It should be noted that the volume obtained through the empirical relationship represents a preliminary estimate of the required pressurised volume. For short-duration missions, the logarithmic relationship yields values that are either negative or unacceptably low; a minimum total pressurized volume of $10\,\text{m}^3$ is therefore imposed, independently of the formula result:

$$V_{\text{press}} = \max\left(V_{\text{press}},\ 10\,\text{m}^3\right) \tag{2.20}$$

In the analyses preceding the optimisation, the rover radius is fixed and the rover lenght is determined so as to satisfy this habitable volume requirement. The actual rover geometry will then be determined in the optimisation phase in Chapter 5, which takes into account additional geometric constraints and the integration of subsystems.

Hemispherical cap

For a sphere subjected to internal pressure p, the principal stresses are equal and uniform:

$$\sigma_\theta = \sigma_\phi = \frac{p\,r}{2t}, \tag{2.21}$$

where r is the radius of the dome and t is the wall thickness.

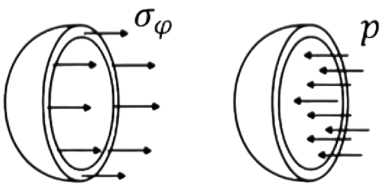

Figure 2.8: Stresses in the hemispherical shell

Cylinder

In the cylindrical section, the principal stresses due to internal pressure p are given by:

- Circumferential stress:

$$\sigma_\theta = \frac{p\,r}{t} \tag{2.22}$$

- Longitudinal stress:

$$\sigma_z = \frac{p\,r}{2t} \tag{2.23}$$

where r is the radius of the cylinder and t is the wall thickness.

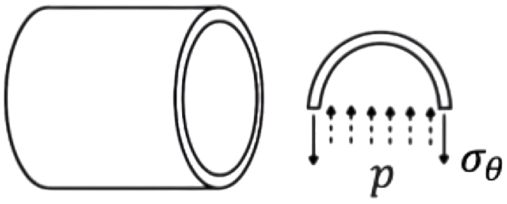

Figure 2.9: Stresses in the cylinder

Tresca Yield Criterion

The design of the pressurized structure requires the adoption of a yield criterion that allows verification of whether the stress state induced by the internal pressurization is compatible with the mechanical properties of the material. In this study, the Tresca criterion is adopted, widely used in the aerospace field for ductile materials such as aluminum alloys. The three-dimensional stress state at a point is described by the stress tensor σ:

$$\sigma = \begin{bmatrix} \sigma_{xx} & \tau_{xy} & \tau_{xz} \\ \tau_{xy} & \sigma_{yy} & \tau_{yz} \\ \tau_{xz} & \tau_{yz} & \sigma_{zz} \end{bmatrix},$$

whose principal stresses are the eigenvalues of the tensor, denoted as:

$$\sigma_1 \geq \sigma_2 \geq \sigma_3. \tag{2.24}$$

The Tresca criterion states that the onset of plastic deformation occurs when the maximum shear stress reaches a critical value. In terms of principal stresses:

$$\tau_{\max} = \frac{\sigma_1 - \sigma_3}{2} \leq \tau_e \tag{2.25}$$

where τ_e is the allowable shear stress, related to the material's yield stress:

$$\tau_e = \frac{\sigma_y}{2\,SF_y}, \tag{2.26}$$

with SF_y the safety factor chosen for yielding. From these relations, the operational form of the criterion is obtained:

$$\sigma_1 - \sigma_3 \leq \sigma_e, \quad \text{with} \quad \sigma_e = \frac{\sigma_y}{SF_y}. \tag{2.27}$$

In the case of cylindrical shells or hemispherical caps subjected to internal pressure p, the principal stresses can be calculated as:

- Hemispherical cap: $\sigma_\phi = \sigma_1 = \frac{pr}{2t}$, $\sigma_\theta = \sigma_\phi = \sigma_2$, $\sigma_3 = \frac{-p}{2}$.
- Cylinder: $\sigma_\theta = \frac{pr}{t}$, $\sigma_z = \frac{pr}{2t}$, with $\sigma_3 \approx 0$.

Substituting these values into the Tresca criterion gives the expressions for the minimum thicknesses:

$$t_{\text{cap}} = \frac{p\,r}{2(\sigma_e - p/2)}, \tag{2.28}$$

$$t_{\text{cylinder}} = \frac{p\,r}{\sigma_e - p/2}. \tag{2.29}$$

The presented formulations permit the direct incorporation of both the safety factor and internal pressure in the determination of wall thickness, thereby ensuring structural integrity under yielding conditions. While the Tresca-based criterion provides the theoretical minimum thickness required to prevent yielding, the resulting values are often negligible. Consequently, a conservative lower bound of 1.5 mm has been adopted in accordance with UG-16 of the ASME Boiler and Pressure Vessel Code, Section VIII, Division 1 [16]. In instances where the analytical calculation indicates a smaller value, the design thickness is set to this minimum to ensure adherence to established pressure vessel design standards.

Results

The results shown in Figure 2.10 allow analysis of the structure's mass behavior as a function of the main geometric parameters, such as the rover's length and radius. In particular, parametric studies highlight how the total mass increases both with the elongation of the structure and with the increase in its radius, providing useful information on the project's sensitivity to dimensional choices and overall scalability of the structure.

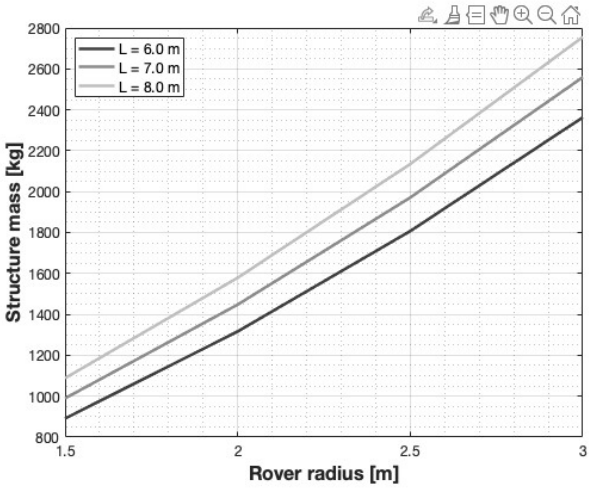

Figure 2.10: Influence of geometric parameters on the structure's weight

Furthermore, as the radius increases, the thickness of both the hemispherical cap and the cylinder increases to maintain resistance to internal pressure (Figures 2.11 and 2.12). This trend is predicted by thin shell theory, which we used for the design: the required thickness grows proportionally to the radius so that stresses remain within the material's allowable limits. However, for the same radius, the cylinder's thickness is greater than that of the hemispherical cap. This is due to the cap distributing the internal pressure more uniformly over the curved surface, reducing the maximum local stress compared to the cylinder.

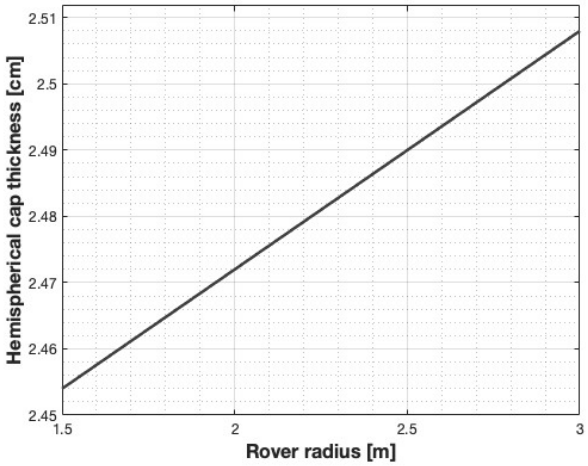

Figure 2.11: Thickness of the hemispherical cap as a function of radius.

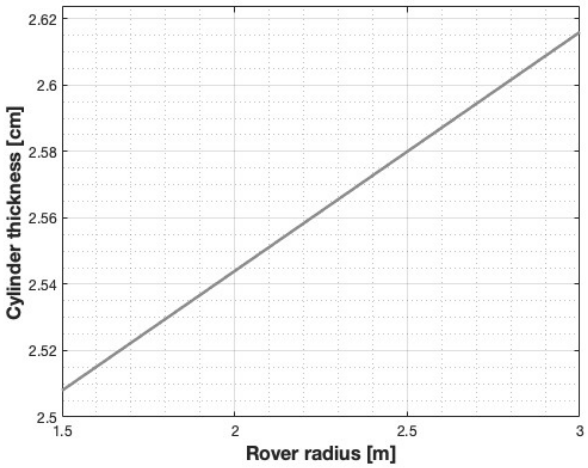

Figure 2.12: Thickness of the cylinder as a function of radius.

2.4.3 Energy System

The rover's energy system ensures continuous power supply to all systems throughout the entire mission. It is designed as a hybrid architecture, composed of batteries and solar panels. Batteries provide constant energy during driving phases, eclipse periods, and emergency situations, while photovoltaic panels ensure energy production during operational phases in illumination conditions, recharging the batteries and meeting the vehicle's daily energy demand.[17]

Battery Sizing

The energy demand of the battery pack is determined through a time-domain simulation of the mission energy balance. The photovoltaic array output power P_{solar} is first established through a global energy balance (Section 2.4.3), and the battery energy balance is then simulated over the full mission timeline:

$$\Delta E_{\text{batt}}(t + \Delta t) = \Delta E_{\text{batt}}(t) + \Big(P_{\text{gen}}(t) - P_{\text{load}}(t)\Big) \cdot \Delta t, \quad \Delta E_{\text{batt}}(0) = 0 \tag{2.30}$$

The simulation is initialised at zero so that negative excursions of $\Delta E_{\text{batt}}(t)$ directly represent the energy debt that the battery must cover. The maximum energy deficit E_{deficit}, which drives the battery sizing, is then identified as the deepest negative excursion over the full mission duration. The instantaneous power generation $P_{\text{gen}}(t)$ depends on two time-varying vectors defined over the full mission duration: *light*(t), which encodes the illumination condition at each instant (either sunlit or dark) and *activity*(t), which specifies the operational phase being performed at each instant, such as driving, EVA, stop, or sleep. Solar generation is active only when the rover is in sunlight and not driving:

$$P_{\text{gen}}(t) = \begin{cases} P_{\text{solar}} & \text{if } \textit{light}(t) = \textit{sun} \text{ and } \textit{activity}(t) \neq \textit{drive} \\ 0 & \text{otherwise} \end{cases} \tag{2.31}$$

The maximum energy deficit is defined as the largest negative excursion of the battery energy balance, corresponding to the most demanding period of consecutive low-generation hours the batteries must bridge before being recharged by the solar array:

$$E_{\text{deficit}} = \max_{t} \left(-\Delta E(t)\right) \tag{2.32}$$

An emergency energy margin is added, corresponding to a return maneuver to base at maximum speed $v_{\max}$ from the maximum reachable distance $r_{\max}$:

$$E_{\text{emerg}} = P_{\text{drive}} \cdot \frac{r_{\max}}{v_{\max}} \tag{2.33}$$

The total energy required from the battery pack is therefore:

$$E_{\text{req}} = E_{\text{deficit}} + E_{\text{emerg}} \tag{2.34}$$

The required battery capacity, accounting for the maximum depth of discharge (DoD), end-of-life capacity degradation (*fade*), and the battery round-trip efficiency η_{batt}, is:

$$E_{\text{batt,req}} = \frac{E_{\text{req}}}{\text{DoD} \cdot (1 - \textit{fade}) \cdot \eta_{\text{batt}}} \tag{2.35}$$

The battery pack is assembled by connecting N_s cells in series to achieve the required bus voltage V_{bus}, and N_p such strings in parallel to meet the required capacity. The example of series-parallel configuration is illustrated in Figure 2.13.

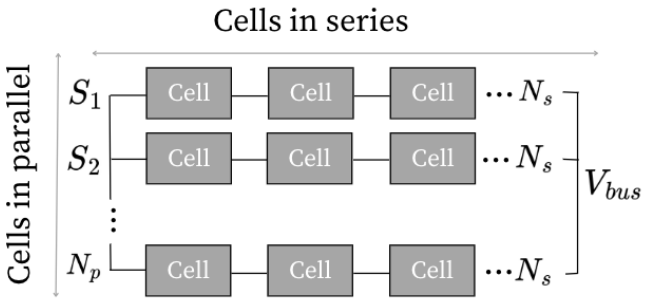

Figure 2.13: Series and parallel configuration of the battery pack

The number of cells in series required to ensure the nominal bus voltage is:

$$N_s = \left\lceil \frac{V_{\text{bus}}}{V_{\text{cell}}} \right\rceil \tag{2.36}$$

The number of parallel cells is determined by imposing two constraints:

- Energy constraint:

$$N_{p,E} = \left\lceil \frac{E_{\text{batt,req}}}{N_s \cdot E_{\text{cell}}} \right\rceil \tag{2.37}$$

- Max cell current constraint:

$$I_{\text{bus}} = \frac{P_{\text{max}}}{V_{\text{bus}} \cdot \eta_{\text{el}}}, \quad N_{p,I} = \left\lceil \frac{I_{\text{bus}}}{I_{\text{cell,max}}} \right\rceil \tag{2.38}$$

The final number of parallel cells is:

$$N_p = \max\left(N_{p,E},\, N_{p,I}\right) \tag{2.39}$$

The total number of cells in the battery pack and the resulting usable energy are:

$$N_{\text{tot}} = N_s \cdot N_p, \quad E_{\text{usable}} = N_{\text{tot}} \cdot E_{\text{cell}} \tag{2.40}$$

where:

$$E_{\text{cell}} = C_{\text{cell}} \cdot V_{\text{cell}} \tag{2.41}$$

Finally, the mass and volume of the battery pack are calculated as:

$$m_{\text{pack}} = \gamma \cdot N_{\text{tot}} \cdot m_{\text{cell}}, \quad V_{\text{pack}} = N_{\text{tot}} \cdot V_{\text{cell}} \tag{2.42}$$

where γ is the *mass packing factor*, representing the ratio between the total battery pack mass and the mass of the cells alone, including all additional components required for the pack to function. In the case of total eclipse, no solar generation is available ($t_{\text{sun}} = 0$) and the battery pack must supply the entire energy demand of the mission:

$$E_{\text{deficit}} = E_{\text{tot}} \tag{2.43}$$

Solar Panel Sizing

The photovoltaic system serves as the rover's sole energy source. Since the batteries function merely as a temporary buffer, storing energy during illuminated periods and releasing it during darkness, eclipses, or driving phases, the solar array must be capable of supplying the total energy required for the entire mission, including the energy consumed when the panels are inactive while recharging the batteries.

The required array output power is determined by a global energy balance over the full mission duration:

$$P_{\text{solar}} = \frac{E_{\text{tot}}}{t_{\text{sun}}} \tag{2.44}$$

where E_{tot} is the total energy consumed by all subsystems over the mission:

$$E_{\text{tot}} = \int_{t_0}^{t_f} P_{\text{load}}(t)\, dt \tag{2.45}$$

and t_{sun} is the total time during which the panels are operational. In the case of total eclipse, $t_{\text{sun}} = 0$ and no panels are sized ($A_{\text{array}} = 0$), with the entire energy demand covered by the battery pack alone.

The required array area is then:

$$A_{\text{array}} = \frac{P_{\text{solar}}}{G_{\text{mean}} \cdot \eta_{\text{cell}} \cdot \eta_{\text{sys}}} \tag{2.46}$$

where G_{mean} is the mean solar irradiance, η_{cell} the photovoltaic cell efficiency, and η_{sys} the overall system efficiency. The total mass of the array is:

$$M_{\text{array}} = \gamma_{\text{pv}} \cdot A_{\text{array}} \tag{2.47}$$

where γ_{pv} is the specific mass of the photovoltaic system.

Results

The results of this section are derived from parametric studies carried out by varying certain cell characteristics. The Figure 2.14 highlights the advantage of using cells with higher capacity: for a given usage time, a battery pack composed of higher-capacity cells results in a lower total pack mass.

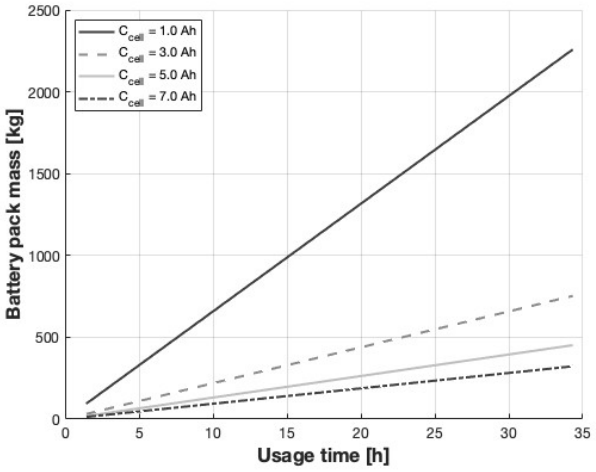

Figure 2.14: Battery pack mass as a function of usage time for different cell capacity.

In particular, the Figure 2.15 clearly shows the direct relationship between the total pack mass and the capacity of each cell. This behavior is closely linked to the number of cells required to meet the power demand of the mission. The number of cells in series remains constant, as it depends solely on the bus voltage, while the number of cells in parallel decreases as the capacity of individual cells increases, leading to a lower total number of cells and, consequently, a lighter overall pack mass.

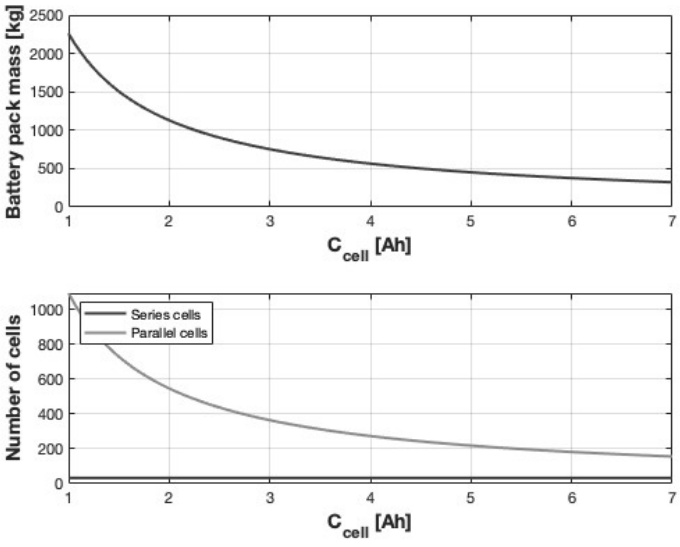

Figure 2.15: Battery pack mass as a function of cell capacity.

2.4.4 Environmental Control and Life Support System (ECLSS)

The ECLSS is one of the most critical subsystems for the survival and operational capability of astronauts inside a pressurized lunar rover. Its function is to maintain internal conditions compatible with human presence, ensuring control of atmospheric composition, temperature, pressure, and humidity, as well as the supply of oxygen, water, and waste management. In this study, two possible system architectures are considered:

- Non-regenerative solution, based on the use of consumables. In this configuration, vital resources such as oxygen, water, and chemical absorbers for carbon dioxide removal are replenished regularly.
- Regenerative solution, which employs systems capable of recycling a portion of the consumed resources. This approach reduces the total mass of support materials required for the mission but demands electrical power, thermal management capacity, and a higher level of functional and operational complexity.

Non-regenerative system

The non-regenerative system relies entirely on pre-supplied resources without any recycling: oxygen, water, food, and chemical absorbers (LiOH) are transported in sufficient quantity to ensure crew survival and operational capability throughout the mission. The total system mass therefore depends linearly on the number of crew members N and the mission duration d in days.[19] For this configuration, the power required and the heat produced by the system are considered negligible. The daily requirements are reported in Table 2.12, while the mass of tanks and associated support materials (Equivalent System Mass, ESM) is shown in Table 2.13. All data are expressed in units of $\mathrm{kg}/(\mathrm{CM} \cdot \mathrm{d})$, where CM (Crew Member) indicates a single crew member and d one mission day. Thus, the numerical value in the table indicates the quantity of resource required for *one crew member per day of mission*.

Output / Input	Mass [kg/CM-d]
Crew requirements	
Oxygen for crew	0.84
Solid food	0.62
Drinking and food preparation water	3.52
Urine discharge water	0.50
Wash water	1.29
Crew waste	
Carbon dioxide	1.00
Condensate from respiration and perspiration	2.28
Urine and wastewater	2.00
Used wash water	1.29
Total system outputs	6.77
Total system inputs	6.57

Table 2.12: ECLSS outputs and inputs in kg/CM-d.

Parameter	Mass [kg/CM-d]
Oxygen tanks	0.34
Water tanks	1.06
LiOH and packaging	1.75
Total	3.15

Table 2.13: Mass of tanks and materials for a non-regenerative ECLSS configuration (kg/CM-d).

$$M_{\text{non-reg}} = ((O_{2,\text{req}} + O_{2,\text{tank}} + H_2O_{\text{req}} + H_2O_{\text{tank}} + \text{LiOH} + \text{LiOH}_{\text{canister}} + \text{M}_{\text{food}}) \cdot N_{\text{crew}} \cdot t_{\text{mission}}) \cdot 1.3 \tag{2.48}$$

The equation above estimates the total mass of the non-regenerative life support system. It sums the daily requirements of oxygen, water, LiOH, solid food, and the mass of associated tanks and containers. The result is then multiplied by the number of crew members N_{crew} and mission duration t_{mission}, including a 30% margin for safety. This margin accounts for variations in consumable usage due

to unforeseen events, ensuring that life support capability is maintained under non-nominal conditions.[20]

Regenerative system

The regenerative system aims to reduce the overall transported mass by recycling consumed resources, thus decreasing dependency on consumables. However, it requires a more complex architecture compared to the non-regenerative solution.

For mass estimation of the regenerative system, the Equivalent System Mass method was used, similarly to the non-regenerative configuration.[21] In this case, only the mass of subsystem components is considered, without including contributions from electrical power or cooling, as these are evaluated separately in dedicated systems.

The subsystems considered were adapted from those on the ISS to the operational conditions of a lunar rover, and the mass, volume, and number of units were sized according to the number of crew members for the mission (Table 2.13). The main devices analyzed and their primary functions are:

- CDRA: removes carbon dioxide from the rover's atmosphere, maintaining breathable concentrations for the crew.
- CRS: converts part of the removed CO_2 into water or other byproducts, reducing the need for waste disposal and consumables.
- OGS: produces oxygen from water via electrolysis, maintaining optimal levels.
- WPA: manages crew water, purifies wastewater, and recycles part of the water resources.
- UPA: processes urine and other liquid wastes, recovering potable water and reducing the need for fresh resources.[22]

The equivalent mass of the k-th subsystem is defined as:

$$m_k^{eq} = \alpha \, m_k \tag{2.49}$$

where:

- m_k is the nominal mass of the subsystem,
- α is the redundancy factor, considered equal to 2. [21]

The equivalent mass normalized per crew member is:

$$ESM_k = \frac{m_k^{eq}}{CM_k} \tag{2.50}$$

Acronym	CM	Mass [kg]	Volume [m^3]	Power [kW]	Cooling [kW]	Logistics [kg/CM-d]
CDRA	4	201	0.39	0.86	0.86	0
CRS	4	18	0.75	0.05	0.27	0
OGS	7	113	0.14	1.47	1.47	0
WPA	10	476	2.25	0.30	0.30	0.13
UPA	8	128	0.37	0.09	0.09	0.06
O_2 storage	4	1088	–	–	–	0
H_2O storage	4	106	0.52	–	–	0

Table 2.14: Regenerative ECLSS subsystems derived from the ISS: capacity, mass, and energy requirements.

The total equivalent mass per crew member is given by the sum of all subsystem contributions:

$$ESM_{\mathrm{CM}} = \sum_{k=1}^{n} ESM_k \tag{2.51}$$

where n is the total number of ECLSS subsystems considered.

The daily logistics term per crew member is defined as:

$$L_{\mathrm{CM,day}} = \sum_{k=1}^{n} L_k \tag{2.52}$$

The total mass of the regenerative system for a mission of duration t_{mission} is then:

$$M_{\mathrm{reg}} = N_{\mathrm{crew}} \cdot ESM_{\mathrm{CM}} \; + \; N_{\mathrm{crew}} \cdot t_{\mathrm{mission}} \cdot (L_{\mathrm{CM,day}} + M_{\mathrm{food}}) \tag{2.53}$$

Risultati

The initial results, shown in the graphs below, highlight how the overall mass of the ECLSS varies as a function of mission duration and crew size, allowing also a comparison between the regenerative and non-regenerative solutions.

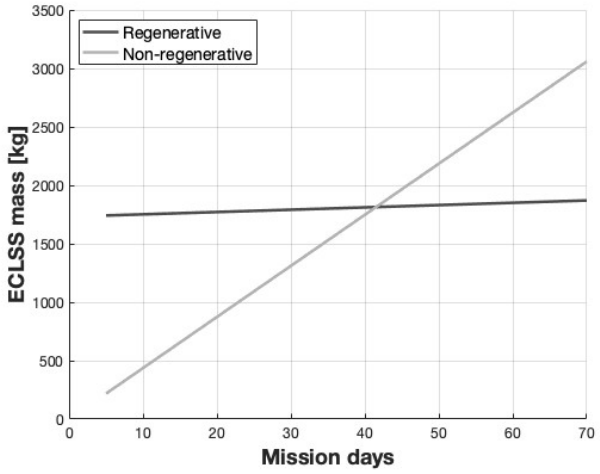

Figure 2.16: Effect of the number of mission days on the ECLSS system mass for both configurations

From the analysis of the data presented in Figure 2.16, it can be observed that the total system mass increases with the number of mission days in both configurations considered. However, the increase is more pronounced for the non-regenerative system, while in the regenerative system the growth is more contained. This behavior is directly related to the operating principles of the two systems: in the non-regenerative system, the mass depends proportionally on the amount of consumable resources required for the mission duration; consequently, as the number of mission days increases, the total mass to be transported also grows. In contrast, in the regenerative system, the mass is primarily determined by the regenerative devices, sized according to the number of crew members, while the influence of mission duration is limited to spare parts or periodic maintenance of the subsystems.

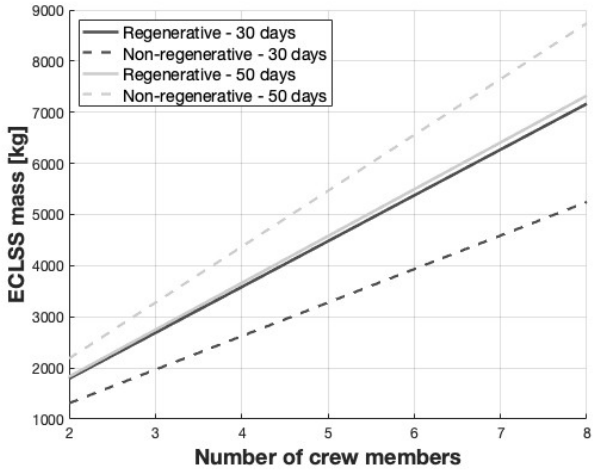

Figure 2.17: Effect of crew size on the ECLSS system mass for both configurations

Analyzing the behavior of the system mass in both configurations as the number of crew members varies, the graph in Figure 2.17 is obtained. It can be observed that, for both solutions, the mass increases linearly with the number of astronauts. In particular, for the regenerative system, it is evident that the mass is more sensitive to crew size than to mission duration, highlighting that team size is the predominant factor in determining the overall system mass for this configuration.

Considering the example mission, whose data are provided in Table 2.10, the resulting configuration is the non-regenerative one, since the mission lasts 14 days. From Figure 2.18 it can be seen how the residual mass of the system progressively decreases over the course of the mission. This trend reflects the daily consumption of life support materials such as oxygen, water, food, and LiOH, used daily by the astronauts.

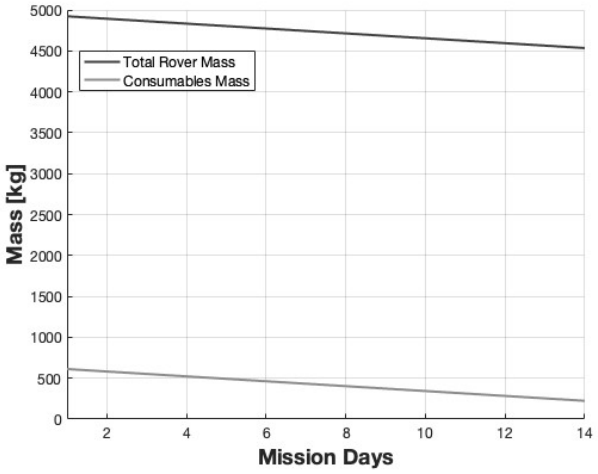

Figure 2.18: Trend of consumables mass reduction over the mission days

2.4.5 Thermal Control System

The thermal control system of the pressurized rover is of fundamental importance to ensure crew survival and proper subsystem operation in an extreme environment such as the lunar surface. The Moon's surface is characterized by very large temperature fluctuations, absence of atmosphere, and direct solar radiation that varies drastically between lunar day and night. These conditions require precise control of the vehicle's internal temperature.

The thermal system is therefore composed of two main components:

1. Passive systems, such as MLI, which reduce heat transfer to the outside, limiting losses during cold phases and protecting against thermal extremes during hot phases.

2. Active systems regulate the rover's internal temperature by removing waste heat from the MLI and that produced by subsystems and astronauts. This system consists of a fluid loop in which coolant is circulated by a pump. The liquid transports the heat to a radiator that dissipates it to the outside.[23]

Passive Thermal Control System

MLI represents one of the main passive thermal control tools used in space applications.[24] MLI consists of alternating layers of reflective films and insulating spacers:

- The reflective films, typically made of metallized polyimide, reduce thermal radiation between layers and toward the external environment.

- The separators/spacers maintain a minimum distance between layers, limiting conduction through the stack. These spacers are generally made of lightweight, thermally insulating materials; for this application, Dacron (polyester) was chosen.

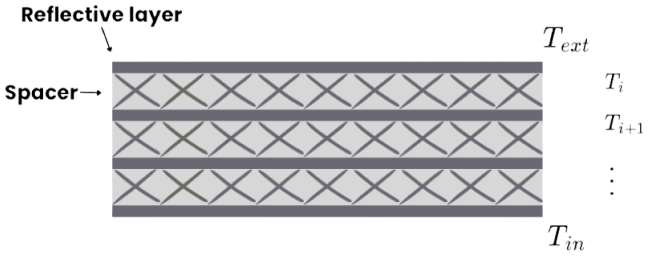

Figure 2.19: Schematic representation of the MLI

MLI can be modeled as a network of thermal resistances, where conduction and radiation between layers are represented as series resistances.[25] The simplified model assumes that heat transfer occurs in a steady, one-dimensional manner, providing an effective estimate of the insulation's thermal performance. The heat flux through each MLI layer can be expressed as the sum of radiative and conductive contributions:

$$q_i = K_i^{\text{tot}} \left(T_{i+1} - T_i\right) \tag{2.54}$$

where q_i is the heat flux through layer i, T_i and T_{i+1} are the temperatures at the layer boundaries, and K_i^{tot} is the total thermal conductance of the layer. The total thermal conductance is given by the sum of the radiative and conductive contributions:

$$K_i^{\text{tot}} = K_i^{\text{rad}} + K_i^{\text{cond}} \tag{2.55}$$

The radiative contribution, which depends on the emissive properties of the films, is calculated as:

$$K_i^{\text{rad}} = \frac{\sigma \left(T_i + T_{i+1}\right)\left(T_i^2 + T_{i+1}^2\right)}{\frac{1}{\varepsilon_i} + \frac{1}{\varepsilon_{i+1}} - 1} \tag{2.56}$$

The conductive contribution, associated with the spacers between layers, is:

$$K_i^{\text{cond}} = \frac{C_1 \, f \, k_{\text{sp}}(T_i)}{\Delta x_i} \tag{2.57}$$

Finally, the total heat flux through the MLI is determined by summing the thermal resistances of all layers:

$$q = \frac{T_h - T_c}{\sum_{i=1}^{N} \frac{1}{K_i^{\text{tot}}}} \tag{2.58}$$

To determine a suitable number of layers N, the reduction in heat flux $q(N)$ is evaluated as the number of layers increases. The discrete variation of the heat flux is calculated as

$$\Delta q_i = q(N_{i+1}) - q(N_i) \tag{2.59}$$

where $q(N_i)$ is the heat flux computed for i layers. As the number of layers grows, the marginal benefit in terms of heat flux reduction diminishes while the associated mass and thickness increase. A threshold ϵ is therefore introduced to identify the point beyond which additional layers provide negligible thermal improvement:

$$|\Delta q_i| < \epsilon. \tag{2.60}$$

The selected number of layers N_{sel} corresponds to the first N_i satisfying this condition, and the associated heat flux is

$$q_{\text{sel}} = q(N_{\text{sel}}). \tag{2.61}$$

The corresponding MLI thickness is

$$L_{\text{tot}} = N_{\text{sel}} \cdot t_{\text{MLI}} \tag{2.62}$$

where t_{MLI} is the thickness of a single layer.

Active Thermal Control System

The rover's active thermal system is designed to regulate the internal temperature of components and the cabin, ensuring crew comfort and proper subsystem operation under extreme conditions. The developed model considers a loop using a water-glycol heat transfer fluid, which circulates through a pump and passes through cold plates in contact with the components to be cooled. The loop manages heat generated by subsystems such as the ECLSS, avionics, batteries, and mobility system motors, in addition to heat generated by the astronauts and residual heat not dissipated by the MLI. The heat is estimated as follows:

- ECLSS: the heat is calculated differently depending on whether the configuration is non-regenerative or regenerative. For the non-regenerative case, it is assumed that no heat is generated by the system, while for the regenerative configuration, reference is made to the heat produced by the system's active components, as reported in Table 2.14;
- Communication system and computers: a heat generation of 600 W is assumed. This value is consistent with the data reported in *Design of a Pressurized Lunar Rover: Final Report* [9], which indicates an equivalent electric power consumption. The assumption is based on the principle that, in an electronic system without moving mechanical parts, nearly all the consumed electrical power is dissipated as heat via Joule effect;

- Batteries: the heat comes from internal losses of lithium-ion cells, calculated as
$$P_{\text{heat}} = P_{\text{input}} \cdot (1 - \eta_{\text{el}})$$
where η_{el} is the battery efficiency (typically 85–95 %), already used for battery pack sizing (Section 2.4.3);

- Mobility system electric motors: the heat is computed from the overall electrical–mechanical efficiency of the motor η_{engine}, which depends on the electrical efficiency η_{el} and transmission efficiency η_{trans}. The unconverted power is dissipated as heat:
$$P_{\text{heat}} = P_{\text{electric}} \cdot (1 - \eta_{\text{engine}})$$
For typical brushless motors, $\eta_{\text{engine}} \approx 90 - 95\,\%$;

- Astronauts: body heat generated by the astronauts is considered constant, with a thermal power of 138.9 W per person.[26]

- Residual MLI: heat not dissipated by the MLI is considered as residual flux toward the pressurized volume, calculated as described in Section 2.4.5.

The mass flow rate of the active thermal control loop $\dot{m}_f$ is assumed by analogy with existing space systems described in the literature, designed to dissipate a thermal load of the same order of magnitude considered here.[27] The fluid temperature drop is calculated as:

$$\Delta T_{\text{fluid}} = T_{\text{in}} - T_{\text{out}} = \frac{Q}{\dot{m}_f \, c_p} \tag{2.63}$$

where Q is the thermal power to dissipate and c_p is the fluid specific heat. For simplicity, it is assumed that:

$$\Delta T_{\text{fluid}} \approx \Delta T_{\text{radiator}}$$

i.e., the fluid temperature drop in the loop is equal to that across the radiator. This simplification is valid assuming a single-phase, constant-flow loop, with the radiator as the only heat dissipation element, negligible heat losses along pipes and other components, and steady-state operation. The radiator area is calculated using the equation [28]:

$$A_{\text{rad}} = \frac{Q_{\text{tot}}}{\varepsilon_{\text{rad}} \, \sigma \, \left(T_{\text{panel}}^4 - T_{\text{sink}}^4\right)} \tag{2.64}$$

where ε_{rad} is the surface emissivity, σ the Stefan-Boltzmann constant, T_{panel} the radiator surface temperature, and T_{sink} the external temperature seen by the radiator.

The total active thermal control system mass includes pumps, radiators, and a percentage margin accounting for pipes, heat exchangers, and coolant. The total system mass can be estimated as:

$$M_{\text{TCS}} = M_{\text{radiators}} + M_{\text{pumps}} + M_{\text{plus}} \tag{2.65}$$

The total pump mass in the main loop can be estimated using the empirical formula by Dexter and Haskin (adapted to SI units) [29]:

$$M_{\text{pumps}} = n_{\text{pumps}} \cdot k \left(\frac{\dot{m}_{\text{per pump}}}{\rho_{\text{f}}} \right)^{0.75} \tag{2.66}$$

where M_{pumps} is the total pump mass [kg], n_{pumps} is the number of required pumps (integer), $\dot{m}_{\text{per pump}}$ is the pump mass flow rate [kg/s], ρ_{f} is the fluid density [kg/m^3], and k is the empirical constant (adapted from Dexter & Haskin, typically 2700 for water/glycol).

The radiator mass is calculated assuming the mass per unit area proposed for *Composite Flow-Through Radiators*, equal to 8.21 kg/m^2.[30] The additional mass, M_{plus}, accounts for thermal system components not directly calculated, such as pipes, heat exchangers, and coolant. This choice is based on historical studies of pressurized rovers and compact landers [9], where these components typically account for 60% of the total active thermal control system mass.

In the cold case, thanks to the high efficiency of the MLI, components remain protected and additional electric heaters are not required. Therefore, the active thermal system is mainly oriented toward cooling, while passive insulation ensures protection against low external temperatures.

Results

The use of MLI allows reducing the heat flux from the external environment into the rover. In particular, increasing the number of layers leads to a higher total thermal resistance R_{tot} and, consequently, a lower heat flux through the wall. The resulting heat flux represents the power that must be dissipated or supplemented by the active thermal control system. In this way, the MLI serves as the first level of passive protection, while the active thermal control system, described in the following section, manages the residual variations, ensuring that the internal temperature remains within safety and comfort limits. The graph shown in Figure 2.20 illustrates how the heat flux through the wall decreases as the number of MLI layers increases, while the total system mass rises proportionally. This behavior highlights the classic trade-off between thermal insulation and added mass: more layers improve insulation efficiency, reducing heat flux, but also increase the mass, which must be accounted for in the overall vehicle sizing.

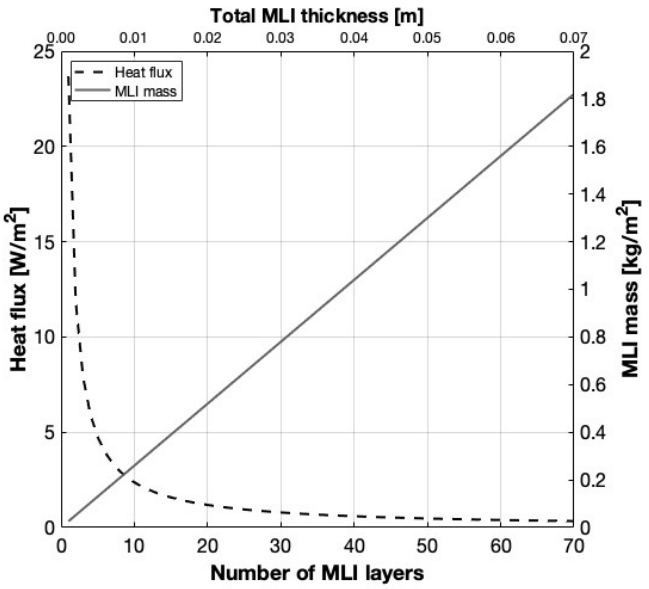

Figure 2.20: Trend of MLI mass and resulting heat flux as the number of layers increases

The Figure 2.21 shows the relationship between the radiator area and the fluid mass flow in the thermal loop. Lower flow rates result in a higher temperature of the fluid entering the radiator, leading to a larger temperature difference between the radiator and the external environment. Consequently, for the same thermal load to be dissipated, a smaller radiator area is required. Similarly, for a given fluid flow rate, an increase in the thermal load to be removed necessitates a larger radiator area, as intuitively expected.

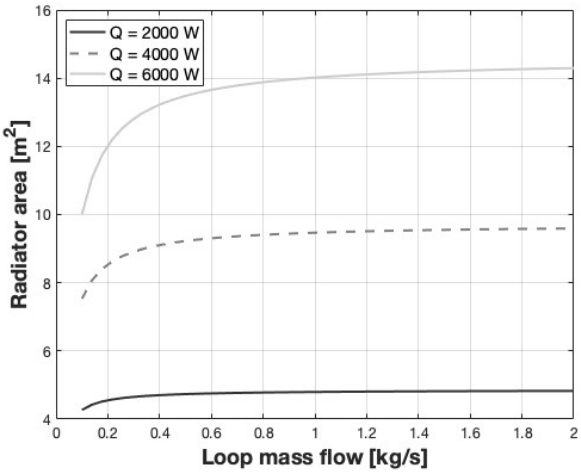

Figure 2.21: Radiator area as a function of fluid mass flow for different heat loads

Chapter 3

Sensitivity analysis

The purpose of this chapter is to evaluate how variations in key mission parameters influence the performance of the rover and its subsystems, considering their impact on mass, power consumption, and heat generation. Sensitivity analysis is useful for assessing the robustness of the model when input parameters vary and for identifying critical aspects that may affect the rover's performance. During the analysis, a coefficient was introduced representing the ratio between the total power required by the rover and the overall rover mass (P/M). This parameter represents the power required per unit mass of the vehicle. Lower values correspond to a more efficient configuration, as less power is required for each unit of rover mass. The minimum of the curve therefore identifies the configuration that achieves the most favorable balance between total power demand and vehicle mass. The main mission parameters investigated include the number of astronauts, mission duration and average rover speed. In addition, the influence of the external temperature was analysed in order to quantify the potential benefits of operating under less extreme environmental conditions. All analyses were performed considering a reference mission configuration whose parameters are reported in Table 2.10. For each case study, only the parameter under investigation was varied, while all the others were kept constant.

3.1 Effect of crew size

Pressurized rover missions reported in the literature generally assume a nominal crew of two astronauts, with the capability of accommodating up to four crew members for short-duration or contingency operations. Similar configurations have been proposed in the JAXA/Toyota pressurized rover concept [31] and in the NASA Space Exploration Vehicle (SEV) studies [32]. In these designs, life-support systems are primarily sized for two astronauts, while temporary extension to four crew

members is possible for limited periods. In the present study, a wider range of crew sizes was considered in order to better evaluate the impact of this parameter on rover performance. Each subsystem was sized according to the total number of astronauts so as to consistently account for the influence of crew size on mass, power consumption, and thermal loads. The results shown in Figure 3.1a indicate that the total rover mass increases approximately linearly with the number of astronauts. In particular, the ECLSS is the subsystem most affected, as additional consumables are required to sustain the crew during the 14-day mission. The variation of the individual subsystem masses is illustrated in Figure 3.1b. Other subsystems also increase in mass, although their contribution is less significant compared with the life-support system. The structural mass increases according to the habitable volume relationship described in Section 2.4.2. The battery mass also increases due to the higher energy demand associated with a larger crew (Figure 3.2a). Consequently, the mass of the mobility system must increase to support the additional weight, as well as that of the thermal control system, which is required to dissipate the greater thermal load (Figure 3.2b).

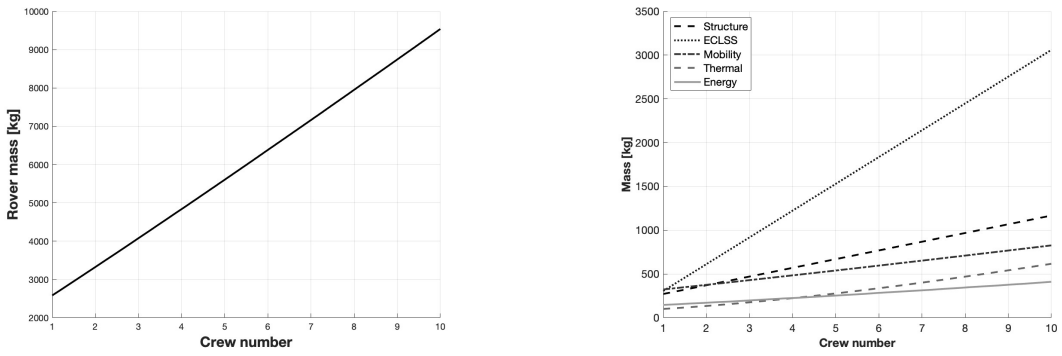

(a) **(b)**

Figure 3.1: Comparison of rover and subsystem mass as a function of crew size

Figures 3.2a and 3.2b show how the rover power consumption and heat generation vary with the number of astronauts. The increase in total rover mass requires greater traction effort, which results in a higher power demand from the mobility subsystem. The ECLSS power consumption is assumed to be negligible for this mission duration because a non-regenerative configuration is adopted. Similarly, the power required by the active thermal control system remains constant, as it depends only on the pump power needed to circulate the coolant in the thermal loop, which is determined by the design flow rate. The overall thermal load generated by the rover follows a trend consistent with the increase in subsystem activity and mass.

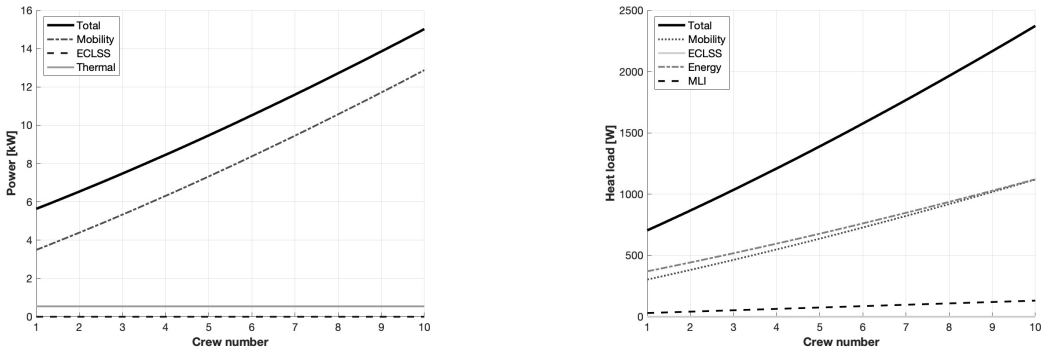

(a) **(b)**

Figure 3.2: Power consumption and heat generation as a function of crew size

The power-to-mass ratio as a function of crew size is shown in Figure 3.3. The trend is non-linear, reflecting the combined evolution of rover mass and subsystem power demand. As the number of astronauts increases, the mass grows faster than the required power, producing a decreasing ratio. However, beyond a certain crew size, the additional power demand associated with the larger crew dominates, causing the ratio to increase again. This produces a minimum, indicating that there exists an optimal crew size that achieves the most favourable balance between total power demand and vehicle mass.

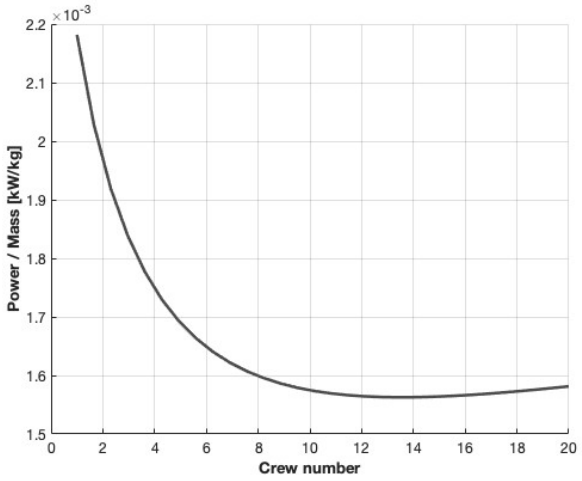

Figure 3.3: Influence of crew size on the power-to-mass coefficient

3.2 Effect of mission duration

Mission duration is a key parameter in the design of a pressurized rover, as it directly affects the sizing of several subsystems. By analysing different mission lengths it is possible to evaluate the penalties in terms of mass, power demand, and thermal loads associated with short-, medium-, and long-duration operations.

In this analysis the mission duration was extended up to 60 days in order to capture the transition from a non-regenerative ECLSS configuration, suitable for short missions, to a regenerative configuration required for longer operations. The results reported in Figure 2.16 indicate that a regenerative system becomes advantageous after approximately 42 days of mission duration. The total rover mass shown in Figure 3.4a exhibits a change in slope corresponding to this transition. In the non-regenerative configuration the mass grows more rapidly with mission duration, since consumables must be stored for the entire mission. Once the regenerative configuration is adopted, the increase in mass becomes less pronounced. The behavior of the individual subsystems is illustrated in Figure 3.4b. A pronounced step is observed in the battery mass curve. Prior to the transition, the energy demand of the ECLSS is negligible; however, in the regenerative configuration the system requires continuous power (Figure 3.5a). This change in power demand leads to the increase in battery mass represented by the step in the graph. The structural mass follows a logarithmic trend, consistent with the volumetric sizing methodology adopted for the rover (Section2.4.2). As the internal volume increases during the mission, the external surface area also increases, resulting in greater heat transfer through the MLI Consequently, the mass of the thermal control subsystem increases, also due to the increased heat produced by the batteries and the mobility system (Figure 3.5b). Finally, the mobility subsystem must adapt to the increased overall mass of the rover, resulting in an increase in its own mass.

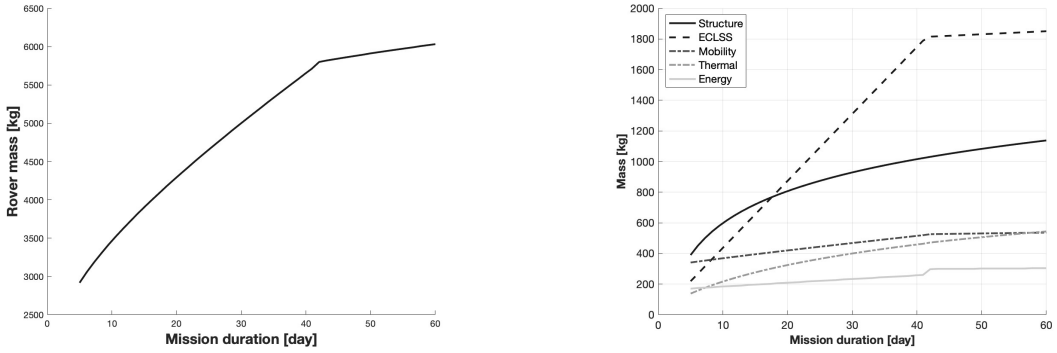

(a) **(b)**

Figure 3.4: Variation of rover and subsystem mass with mission duration

A similar transition to what occurs in the mass plots is visible in the power and heat generation trends (Figures 3.5a and 3.5b). Specifically, the ECLSS's power consumption increases from near zero to a constant value once the regenerative configuration is introduced. The power required by the thermal control system remains constant because it depends on the pump power needed to circulate the coolant within the thermal loop. The mobility subsystem's power varies with the rover's mass, following the trends discussed previously. The trend of the heat produced by the individual subsystems also follows the logic just analyzed.

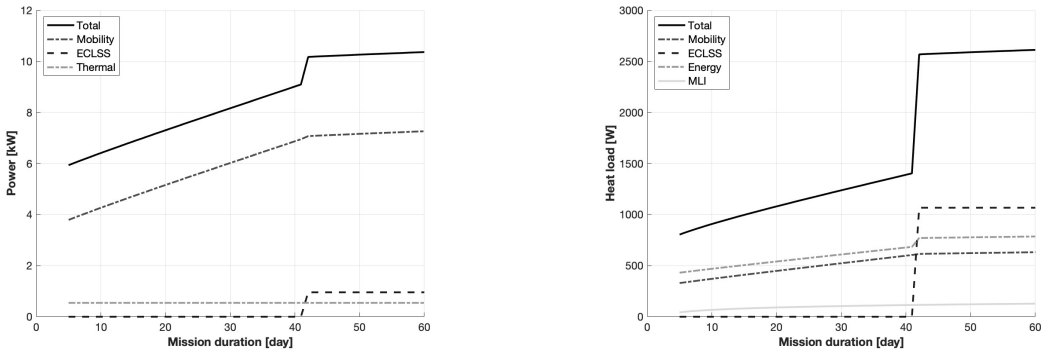

(a) **(b)**

Figure 3.5: Power consumption and heat generation as a function of mission duration

The power-to-mass ratio shown in Figure 3.6 reflects the technological transition of the life-support system. At the beginning of the analysis, before the introduction of the regenerative configuration, the rover mass increases faster than the total power demand, resulting in a decreasing ratio. Once the regenerative ECLSS is introduced, the required power increases more sharply, producing a peak in the ratio and marking the transition to a more energy-intensive configuration. For longer mission durations the total mass continues to increase while the power grows more gradually, leading again to a decreasing trend in the ratio.

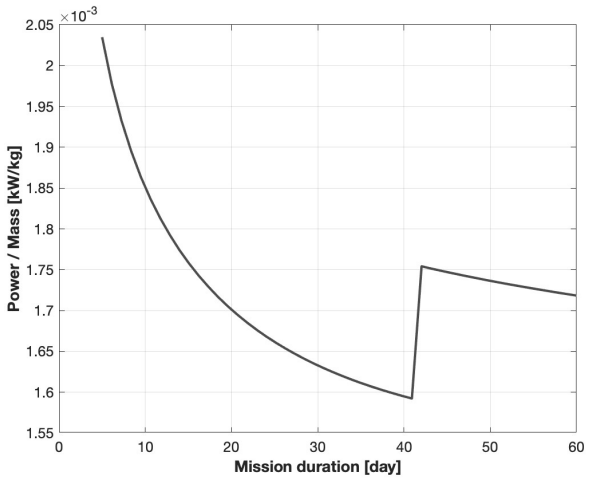

Figure 3.6: Influence of mission duration on the power-to-mass coefficient

3.3 Effect of average speed

The reference mission assumes a nominal rover speed typical of standard exploration operations. The present analysis investigates the trade-off between the operational advantages of higher travel speeds and the associated penalties in terms of mass, power demand, and thermal load. As shown in Figure 3.7a, the rover total mass increases with average speed. This behaviour is mainly driven by the mobility subsystem, which must be sized to provide higher traction power. In contrast, the structural subsystem and the ECLSS remain unaffected by speed variations, as illustrated in Figure 3.7b. The mass of the batteries also increases due to the increase in power required by the rover and consequently the active thermal system also increases its mass to cope with a greater thermal load as shown in Figures 3.8a and 3.8b.

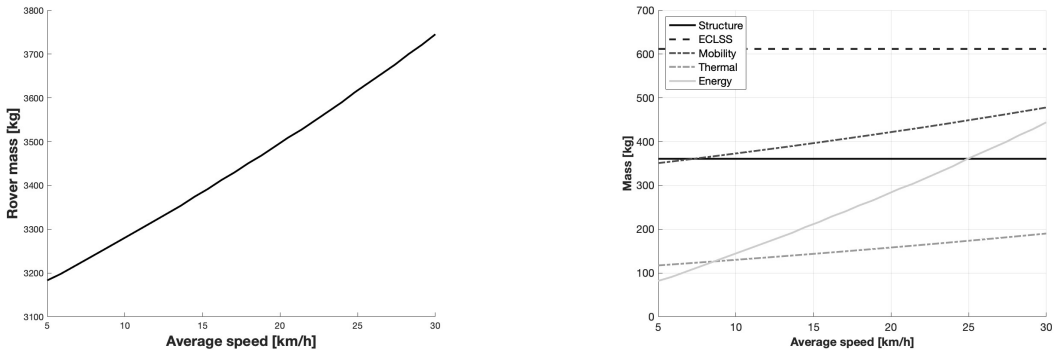

(a) **(b)**

Figure 3.7: Variation of rover and subsystem mass with average speed

As expected, the mobility subsystem shows the largest increase in power demand as the rover speed rises. The ECLSS power remains negligible for the considered mission duration, while the thermal control system requires a constant amount of power determined by the pump used to circulate the coolant. The thermal load generated by the rover follows the same general behaviour observed for the other parameters, with higher subsystem activity resulting in increased heat generation.

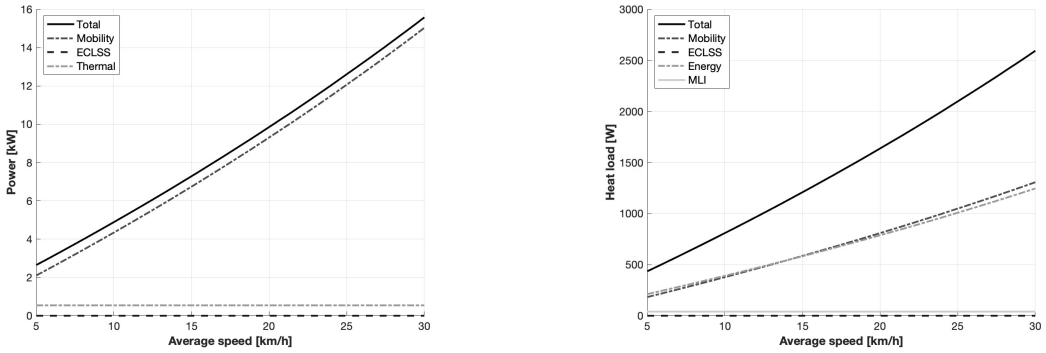

(a) **(b)**

Figure 3.8: Power consumption and heat generation as a function of average speed

The power-to-mass ratio shown in Figure 3.9 increases as the rover speed rises. This indicates that, for a given vehicle mass, the power required to ensure operation grows significantly. As a consequence, the rover becomes progressively more energy-intensive relative to its mass. This behaviour reveals a clear design trade-off: higher travel speeds can improve mission productivity by reducing travel times, but they require significantly larger energy resources and lead to a heavier rover design.

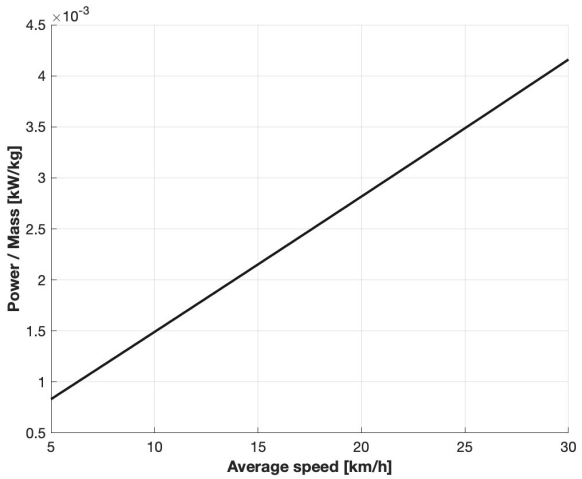

Figure 3.9: Influence of average speed on the power-to-mass coefficient

3.4 Effect of external temperature

Although external temperature is not a controllable mission parameter, analysing its influence is useful to estimate the benefits of operating under more favourable environmental conditions and to validate the thermal model. The analysis was performed considering extreme hot and cold temperature scenarios.

Figures 3.10a and 3.10b show that the rover mass reaches a minimum when the external temperature approaches the internal operating temperature of the vehicle. Under these conditions the required thickness of the multilayer insulation decreases, leading to a reduction in the mass of the thermal protection system and related subsystems.

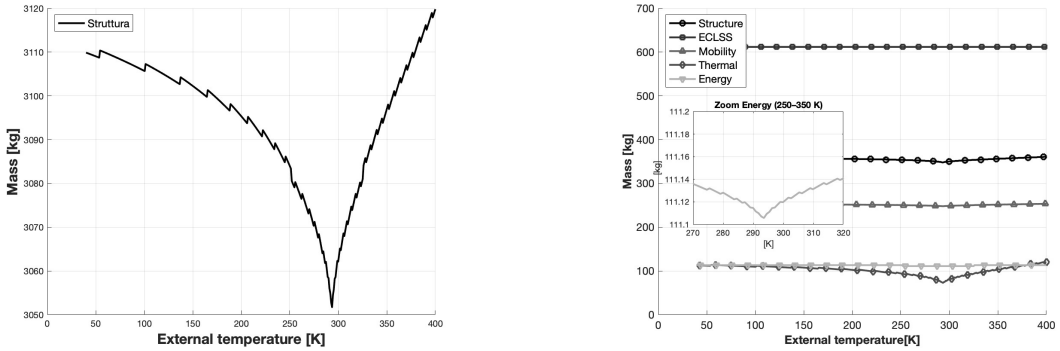

(a) **(b)**

Figure 3.10: Variation of rover and subsystem mass with external temperature

The same trend is observed for power consumption and heat generation, as shown in Figures 3.11a and 3.11b. In the optimal condition, the mobility system requires less power to support a smaller total rover mass. Similarly, the subsystems produce lower thermal loads for that temperature value.

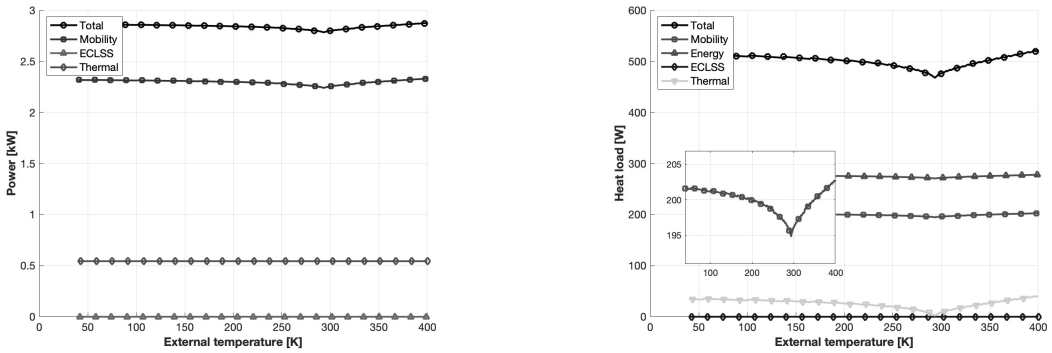

(a) **(b)**

Figure 3.11: Power consumption and heat generation as a function of external temperature

The power-to-mass ratio shown in Figure 3.12 reaches its minimum when the external temperature is close to the internal temperature of the rover. As expected for a given rover mass, it is less energetic when the external temperature is closer to that of the rover's interior.

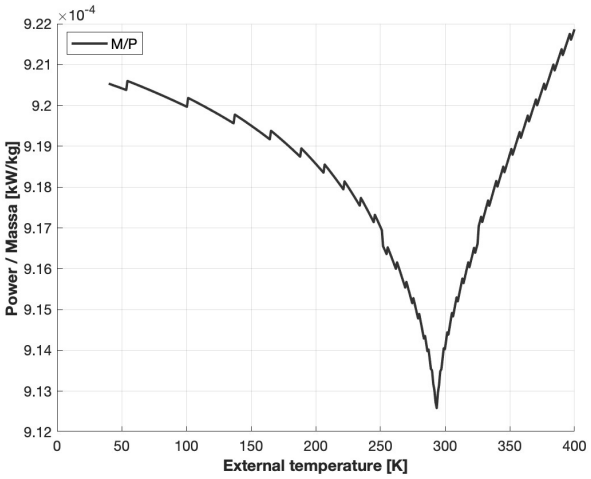

Figure 3.12: Influence of external temperature on the power-to-mass coefficient

Chapter 4

Mission Scenarios

After defining the mass convergence cycle methodology and the procedures that led to the sizing of the individual subsystems, it is possible to apply these results to different operational scenarios for the pressurized rover. A mission scenario represents a simulation of rover operations on the lunar surface, defined by considering mission parameters, illumination conditions, and terrain characteristics. The purpose of this chapter is to analyze the behavior of the vehicle under varying operational and environmental conditions, in order to evaluate the overall system performance and identify potential subsystem limitations. The analysis is developed in two phases. In the first phase, three mission scenarios characterized by different operational durations are considered, assuming a flat terrain. This assumption makes it possible to isolate the influence of energy conditions and mission duration on rover performance, without introducing additional complexities related to mobility on inclined terrain. The analyzed scenarios are the following:

- Short exploration mission: a short-duration scenario representing limited operations in the vicinity of the base. This case makes it possible to evaluate rover performance in the short term and to verify subsystem behavior under relatively moderate operational conditions.

- Medium exploration mission: an intermediate-duration scenario involving more prolonged operations on the lunar surface. This case allows the system behavior to be analyzed over a longer operational period and enables the evaluation of the impact of energy management in the medium term.

- Long exploration mission: a long-duration scenario representing extended rover operations on the lunar surface. This case is useful for evaluating the overall robustness of the system and the rover's capability to sustain extended missions while maintaining onboard functions operational.

For each of these scenarios, three different illumination conditions are also considered, related to the possible occurrence of eclipses during the mission. The analysis of these conditions allows the impact of solar energy availability on the rover's operational performance to be assessed. The illumination conditions considered are the following:

- No eclipse: continuous solar illumination, which ensures maximum energy production from the solar panels and optimal operating conditions for the rover.
- Partial eclipse: temporary interruptions of solar illumination, which lead to a reduction in energy production and require more careful management of operational activities.
- Total eclipse: prolonged absence of solar illumination, resulting in complete dependence on the energy stored in the batteries and possible limitations on the most energy-intensive operations.

In a second phase of the analysis, two more realistic mission scenarios are considered, located in specific regions of the lunar surface characterized by different terrain morphologies. This approach makes it possible to evaluate the impact of terrain slopes and topographical conditions on the performance of the rover's mobility system. The two lunar regions analyzed are:

- Mare Tranquillitatis: a region characterized by relatively regular terrain and generally moderate slopes, representative of conditions favorable to rover mobility.
- Nobile 1 Crater: an area located near the lunar south pole, characterized by more complex morphology and steeper slopes, representing more challenging conditions for the rover's mobility system.

4.1 Scenario Definition and Simulation Approach

For each combination of operational scenario and illumination condition, the mass convergence cycle is applied independently, producing an estimate of the total rover mass and its main subsystems. The obtained results allow for a comparison of system performance as mission duration and illumination conditions vary, highlighting the main criticalities associated with energy management in the different scenarios. The daily activity planning is based on a *day-based* configuration, in which the type of operations performed during the day depends on the nature of the day itself. The first and last days of the mission are always dedicated to driving,

representing departure from the base and return, respectively. Intermediate days alternate between driving and EVA days, with the introduction of a rest day every seven operational days, in analogy with established practices aboard the International Space Station.[33] During rest days, the rover remains stationary, and the energy profile is equivalent to that of a downtime day, with only life support, communication, and thermal control systems active. In all cases, the structure of a 24-hour day includes a sleep phase at the beginning and end, with break periods before and after the main activity, which is concentrated in the central part of the day. The typical daily operational structure is shown in Figure 4.1, while the weekly activity cycle is shown in Figure 4.2.

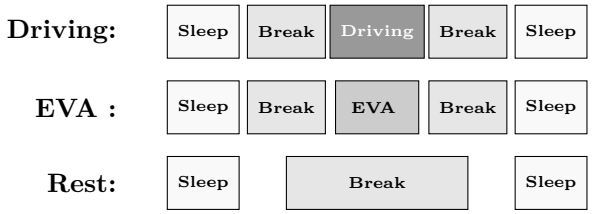

Figure 4.1: Typical daily schedule during mission operations.

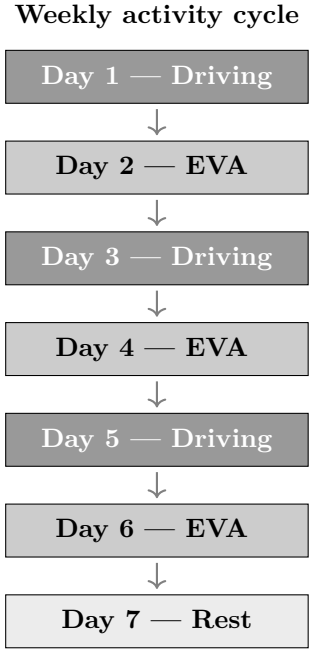

Figure 4.2: Weekly operational cycle of the mission activities.

Illumination conditions are modeled by overlaying an hourly illumination state on the activity timeline, distinguishing between sunlight (SUN) and darkness (DARK). In the no-eclipse case, all mission hours are considered illuminated, ensuring

maximum solar energy availability. In the total eclipse case, the entire day is classified as dark for the full mission duration. In the partial eclipse case, a single daily dark period of random duration between 8 and 12 hours is simulated, positioned randomly within the 24-hour day. This modeling allows a statistically variable representation of eclipse impact on solar energy availability, avoiding the assumption of a fixed or periodic illumination profile.

Lunar surface illumination strongly depends on geographic location and terrain morphology. At the lunar equator, the solar cycle lasts approximately 29.5 Earth days: a rover operating in this region may benefit from roughly 14 consecutive days of sunlight, followed by a comparable period of total darkness. In polar regions, particularly near the south pole, some areas on crater rims experience near-permanent illumination, while complex terrain creates periodic or permanent shadow zones due to high crater walls. The analysis considers three illumination conditions that cover a wide spectrum of realistic operational scenarios without assuming a specific landing site in advance.

Operational Parameter	Symbol	Value	Unit
Crew size	N_{crew}	2	–
Average speed	v_{avg}	8	km/h
Maximum speed	v_{max}	10	km/h
Daily range	d_{day}	25	km
Maximum mission range	d_{max}	40	km
Payload	m_{payload}	300	kg
Environmental Parameter	**Symbol**	**Value**	**Unit**
External temperature (hot case)	$T_{\text{ext,hot}}$	400	K
Internal rover temperature	T_{int}	293.15	K
Time Parameter	**Symbol**	**Value**	**Unit**
Mission duration	t_{mission}	5	days
Driving hours per day	t_{drive}	3.1	h/day
EVA hours per day	t_{EVA}	6	h/day
Sleeping hours per day	t_{sleep}	8	h/day

Table 4.1: Mission parameters short range scenario.

Operational Parameter	Symbol	Value	Unit
Crew size	N_{crew}	3	–
Average speed	v_{avg}	10	km/h
Maximum speed	v_{max}	15	km/h
Daily range	d_{day}	40	km
Maximum mission range	d_{max}	80	km
Payload	m_{payload}	500	kg
Environmental Parameter	**Symbol**	**Value**	**Unit**
External temperature (hot case)	$T_{\text{ext,hot}}$	400	K
Internal rover temperature	T_{int}	293.15	K
Time Parameter	**Symbol**	**Value**	**Unit**
Mission duration	t_{mission}	20	days
Driving hours per day	t_{drive}	4.0	h/day
EVA hours per day	t_{EVA}	6	h/day
Sleeping hours per day	t_{sleep}	8	h/day

Table 4.2: Mission parameters medium range scenario.

Operational Parameter	Symbol	Value	Unit
Crew size	N_{crew}	4	–
Average speed	v_{avg}	15	km/h
Maximum speed	v_{max}	20	km/h
Daily range	d_{day}	80	km
Maximum mission range	d_{max}	150	km
Payload	m_{payload}	800	kg
Environmental Parameter	**Symbol**	**Value**	**Unit**
External temperature (hot case)	$T_{\text{ext,hot}}$	400	K
Internal rover temperature	T_{int}	293.15	K
Time Parameter	**Symbol**	**Value**	**Unit**
Mission duration	t_{mission}	42	days
Driving hours per day	t_{drive}	5.3	h/day

EVA hours per day	t_{EVA}	6	h/day
Sleeping hours per day	t_{sleep}	8	h/day

Table 4.3: Mission parameters long range scenario

4.2 Effect of the Scenario

The results obtained in the no-eclipse case represent the reference scenario, in which illumination conditions are optimal and solar power generation is continuous throughout the mission. The analysis of the *mass breakdown* for the three mission types highlights common trends and significant differences primarily related to operational duration.

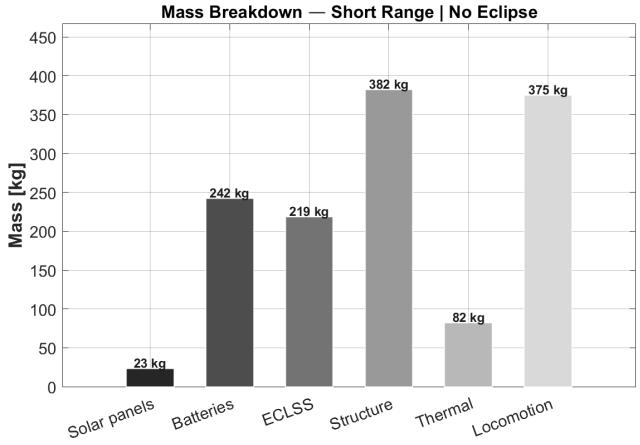

(a) Short mission

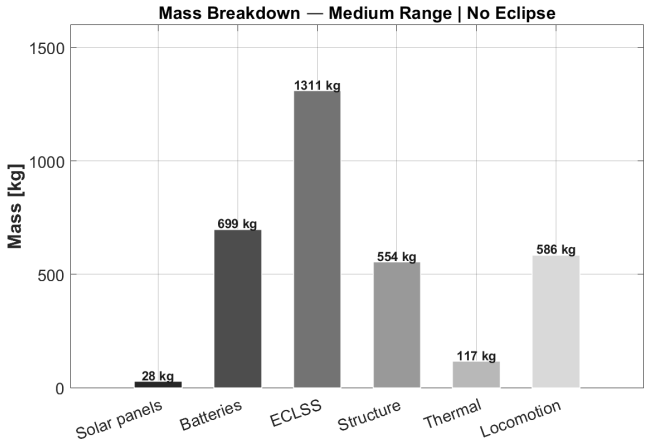

(b) Medium mission

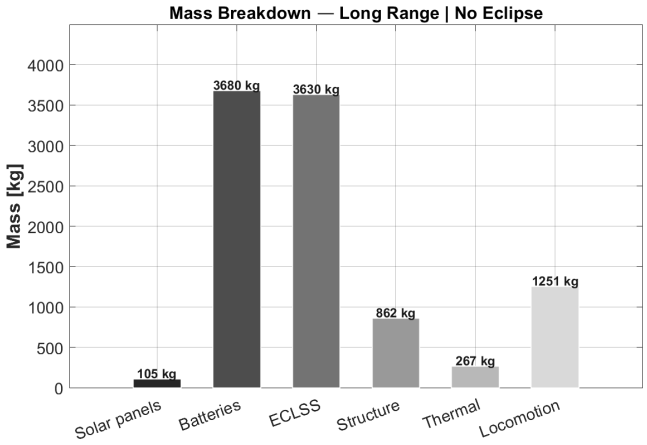

(c) Long mission

Figure 4.3: Mass breakdown for the no-eclipse scenario

In all three scenarios, the dominant subsystem varies with mission duration. In the short mission scenario (Figure 4.3a), structure and locomotion are the main contributors, with masses of 382 kg and 375 kg, respectively, while the batteries reach 242 kg and the solar panels are limited to only 23 kg. This reflects the short operational duration, which keeps the overall energy demand relatively low and allows for a limited sizing of the energy storage system. In the medium-duration mission (Figure 4.3b), the ECLSS becomes dominant, with a mass of 1311 kg, surpassing structure and locomotion at 554 kg and 586 kg, respectively. Battery mass increases significantly to 699 kg, reflecting the higher total energy demand associated with the longer mission duration. Solar panels remain relatively small, at 28 kg, indicating that the required power increases moderately and that full illumination is assumed throughout the mission. In the long-duration mission (Figure 4.3c), both the ECLSS and the energy storage system become the predominant subsystems, with nearly equal masses of 3630 kg and 3680 kg. This substantial increase is due to the high overall energy demand needed to sustain extended operations on the lunar surface. The locomotion system mass also increases to 1251 kg, as it must carry the heavier rover, while solar panels reach 105 kg. In this scenario, subsystem sizing is strongly driven by the need to ensure energy autonomy and life support for extended missions. The total rover mass grows with mission duration, reaching 3023 kg for the short mission, 5295 kg for the medium mission, and 11795 kg for the long mission, demonstrating the predominant role of operational duration in overall sizing. The increased energy demand requires larger batteries, which generate more heat and necessitate larger, heavier radiators. At the same time, the structural mass increases according to a logarithmic relation of the pressurized volume of the rover relative to mission

duration. The locomotion system is also scaled up, with larger motors and frames capable of supporting higher weights, ensuring optimal mobility throughout the mission.

4.3 Effect of Illumination Conditions

The introduction of eclipses in the simulation modifies the mission energy balance and primarily affects the power generation and energy storage systems.

4.3.1 Short mission

In the case of the short mission, the transition from no eclipse to partial eclipse leads to an increase in battery mass from 242 kg to 349 kg and in solar panel mass from 23 kg to 39 kg. The reduction in available illumination hours requires both a greater energy storage capacity and higher power output from the solar panels during the illuminated periods. In the case of a total eclipse, solar panels are eliminated and the batteries must cover the entire mission energy demand, reaching a mass of 1559 kg. Despite this significant increase, the mission remains feasible thanks to the short operational duration, which limits the total energy demand to a level that can still be managed with a battery-only configuration. The total rover mass therefore increases from 3023 kg to 3178 kg and up to 4542 kg in the total eclipse case.

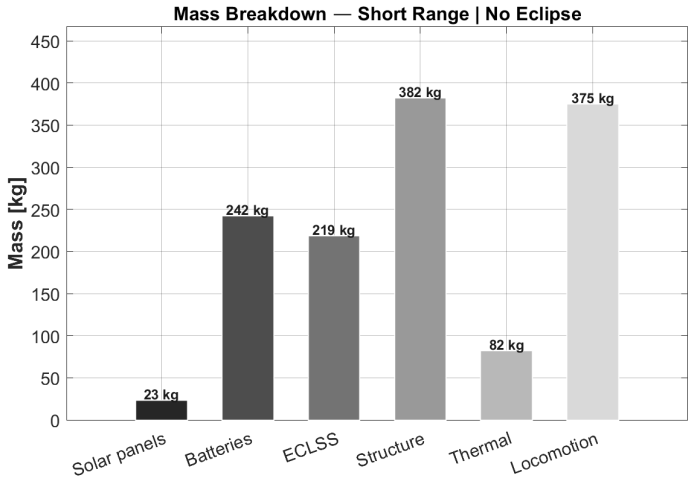

(a)

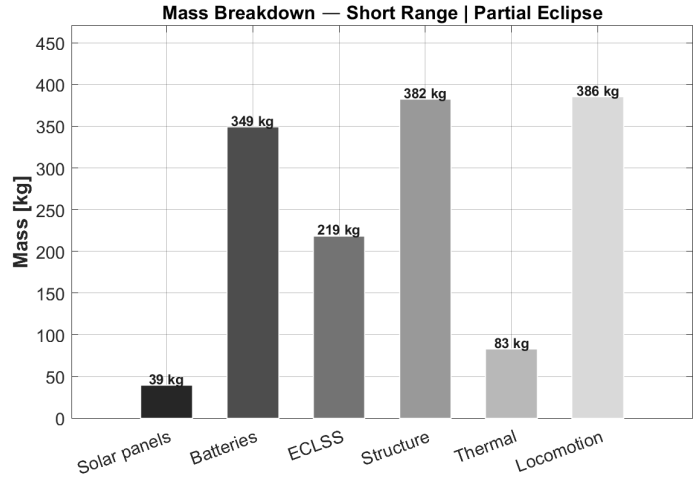

(b)

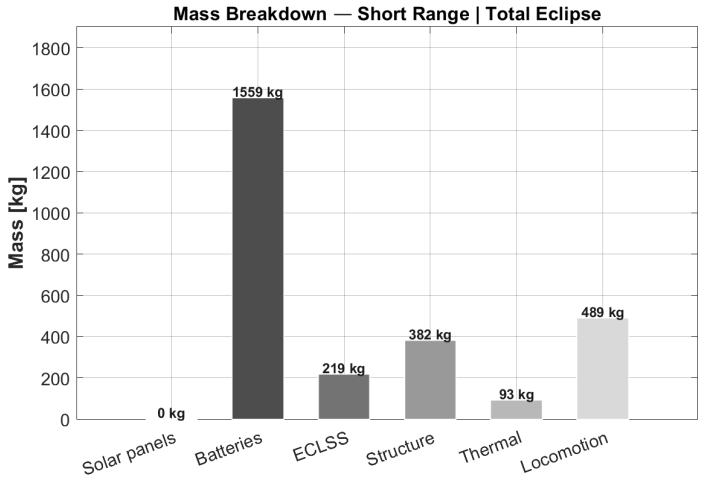

(c)

Figure 4.4: Mass breakdown for the short mission across eclipse scenarios

4.3.2 Medium mission

For the medium-duration mission, the effect of partial eclipses is more pronounced: battery mass increases from 699 kg to 844 kg, while solar panel mass rises from 28 kg to 47 kg. In the case of a total eclipse, the energy system becomes entirely dominated by batteries, which reach a mass of 19878 kg, corresponding to about 83% of the total rover mass. This result highlights how a medium-duration mission under total eclipse conditions approaches the feasibility limit when relying exclusively on a battery-based architecture. The positive feedback cycle between rover mass

and energy demand significantly slows the convergence of the iterative process, producing a technically convergent solution that is nevertheless engineering-wise unrealistic due to the excessive mass penalty.

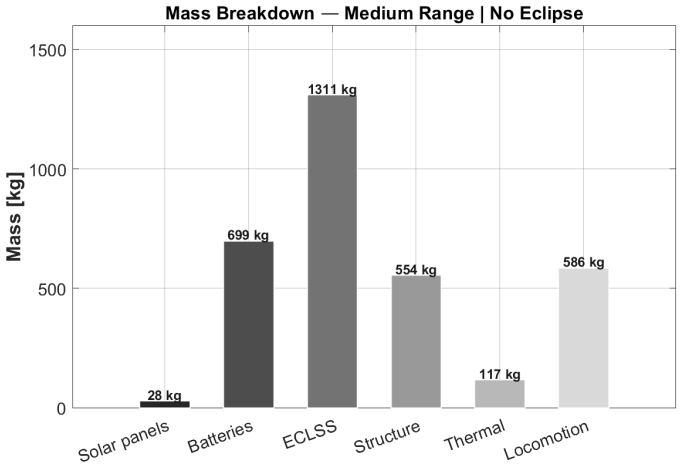

(a)

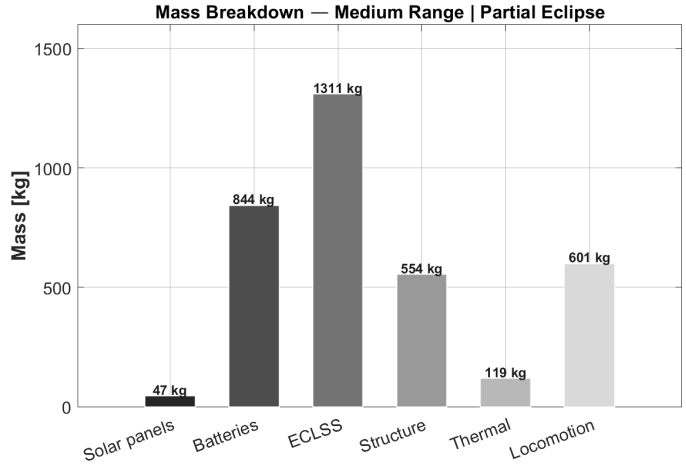

(b)

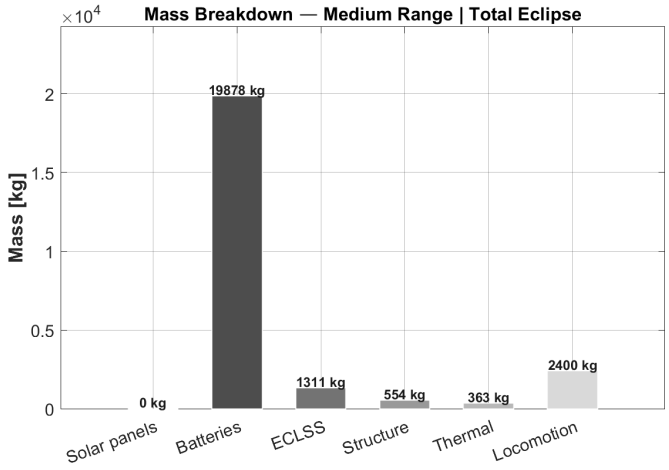

(c)

Figure 4.5: Mass breakdown for the medium mission across eclipse scenarios

4.3.3 Long mission

For the long mission scenario, partial eclipses result in an increase in battery mass from 3680 kg to 4102 kg and solar panel mass from 105 kg to 176 kg, without compromising mission feasibility. In the case of total eclipse, however, the iterative process does not converge. The battery mass required to cover the entire energy demand of such a long mission generates a large increase in the overall rover mass, which in turn increases energy consumption and requires additional batteries. This mechanism triggers a divergent feedback loop that prevents convergence of the model. The long mission under total eclipse conditions is therefore classified as not feasible with the adopted energy architecture. Such scenarios would require the introduction of an alternative energy source, for example a RTG. Radioisotope power systems provide continuous power independent of solar illumination through the radioactive decay of plutonium-238, and they have been successfully adopted in numerous long-duration space missions or in environments where solar energy is insufficient.[34] This extensive operational heritage supports the hypothesis that for lunar missions experiencing prolonged total eclipses, a nuclear-based power system may represent a viable solution when solar panels and batteries alone are insufficient.

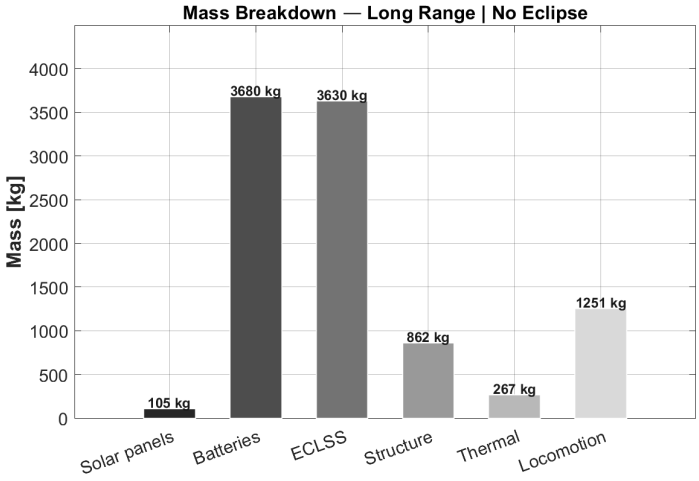

(a)

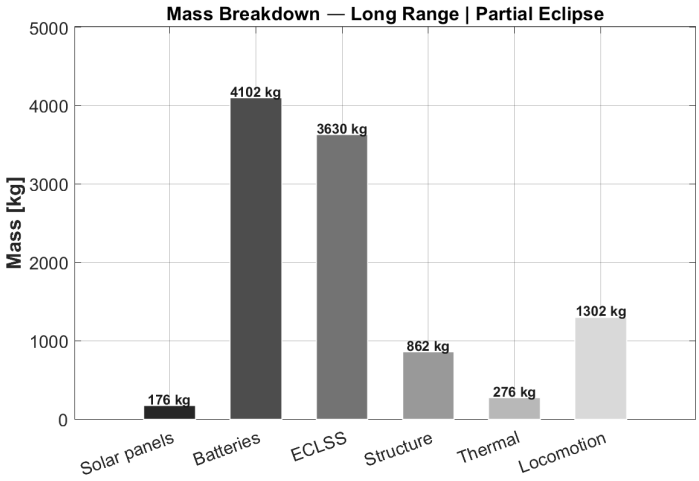

(b)

Figure 4.6: Mass breakdown for the no-eclipse scenario for short, medium and long missions.

4.4 Real Mission Scenarios

In a second phase of the analysis, two more realistic mission scenarios are considered, located in specific regions of the lunar surface characterized by different morphological and environmental terrain conditions. This approach allows the evaluation of the impact of slopes, topographical features, and thermal and illumination conditions on the performance of the rover mobility system, as well as on the overall energy requirements of the mission. The two lunar areas analyzed are the *Mare Tranquillitatis* and the *Nobile Crater*. The parametric analysis conducted in the previous phase revealed that a battery-powered configuration is more advantageous for short- or medium-duration missions, provided that eclipse conditions remain limited. As the mission duration and the duration of the eclipse increase, the mass of the batteries required to meet the rover's energy needs increases significantly, penalizing the rover's overall mass budget. Indeed, the planned missions will be short- or medium-duration, also depending on the availability of illumination in the relevant lunar region. The following sections present the geological characteristics, environmental conditions, and mission-oriented motivations underlying the selection of each region.

4.4.1 Methodology for Path Definition

The definition of the mission paths for the realistic scenarios was carried out using *Lunar QuickMap*, a high-resolution lunar cartographic visualization tool that integrates topographic, altimetric, and illumination data derived from the Lunar Reconnaissance Orbiter Camera (LROC). [35] [36] Starting from the identification of two landing sites (described in the following Sections 4.4.2 and 4.4.3), the paths corresponding to the scientific objectives of the mission were manually traced. For each trajectory, elevation data were extracted point by point, from which the instantaneous slopes along the path were calculated. These data were exported in `.csv` format and directly used in the simulation model to compute instantaneous traction power as a function of the actual terrain slope. The identified paths do not represent optimized trajectories but rather approximate routes consistent with the mission's scientific objectives. This approximation is considered acceptable within the context of a conceptual-level study such as the one presented here, whose purpose is to evaluate system requirements parametrically rather than to define detailed operational planning. Furthermore, the visualization of Permanently Shadowed Regions (PSR) in the lunar South Pole available in *Lunar QuickMap* allowed the identification of permanently shadowed areas intersecting the selected paths. This made it possible to derive the mission illumination timeline and to identify phases of total eclipse to be considered in the energy balance.[37]

4.4.2 Sea of Tranquillity

The *Mare Tranquillitatis* is a vast basaltic region located in the north-eastern hemisphere of the Moon, which belongs to the so-called *maria*, large volcanic basins formed during the late stages of lunar formation, with wide, regular surfaces with slopes typically less than 5° and a relatively uniform layer of regolith. [38] These characteristics make the area a favourable environment for rover mobility, with fewer risks associated with topographical obstacles or high crater walls. The mission starts from the Apollo 11 landing site (0.67°N, 23.47°E), the first manned moon landing on 20 July 1969 [39], and covers a distance of approximately 1014 km in 13 operational days, as shown in Table 4.4. The primary scientific objective of the mission is to investigate the geological history of Mare Tranquillitatis through the direct sampling and characterization of key surface features, including collapse pits, lava domes, irregular mare patches, and impact craters. These sites have been selected to provide complementary evidence on the timing, composition, and mechanisms of lunar volcanism, as well as the subsurface structure of the region. The individual extravehicular activities are planned as follows:

- Southwest Mare Tranquillitatis Pit (Day 2): circular collapse structure (*pit*), i.e. a depression formed when the roof of an underground cavity collapses, potentially exposing access to volcanic cavities or deep layers of regolith. The extravehicular activity (EVA) involves inspecting the edge of the pit and sampling the surrounding regolith in order to characterise the local composition and obtain information on the subsurface structure of the region.[40]

- Lamont (Day 3): circular structure approximately 70 km in diameter interpreted as the remnant of an ancient impact crater subsequently covered by lava flows. The area is of particular scientific interest because it features several Irregular Mare Patches (IMP)s, small, brighter regions with very few craters that could indicate relatively recent volcanic activity (< 1 Ga). The EVA aims to sample these structures to study their composition and determine their geological age.[41]

- Arago Domes (Day 4): an area characterised by dome-shaped volcanic reliefs formed by ancient lava eruptions. The domes belong to different periods in the Moon's history (approximately 3.7, 3.4 and 2.8 billion years ago), offering the opportunity to study how lunar volcanism has changed over time. The basalts of Mare Tranquillitatis are also rich in TiO_2. The EVA plans to sample domes of different ages to compare their composition and age.[42]

- Mare Tranquillitatis Pit (Day 8): a collapse depression approximately 105 m deep and 140 m wide, probably connected to an ancient underground lava tube. Recent radar data indicate the presence of a large cavity beneath the

surface. Structures of this type are of great interest because they could offer more stable and protected environments than the lunar surface. The EVA will involve close observation of the edge of the cavity and sampling of the surrounding regolith.[40]

- Maskelyne (Day 10): an impact crater approximately 22 km in diameter located between the basalt plains of the sea and the lunar highlands. Craters of this type expose different layers of the lunar crust, allowing materials from different depths to be studied. The EVA aims to sample this transition zone to analyse the composition and structure of the crust in the region.[42]

The overall mission route and the geographical distribution of the scientific targets are shown in Figure 4.7: it is clear that the five targets are spread over considerable distances, requiring several days of transfer between one target and another. On the transfer days between targets (Days 5, 6, 7, 9, 11, 12, 13), the route does not pass through areas of primary scientific interest that would justify dedicated EVAs. However, the rover makes regular intermediate stops during which the scientific payload on board operates in autonomous sampling mode along the entire route. This approach maximises the scientific coverage of the mission. Lighting conditions are particularly favourable: the mission is planned entirely during the lunar day, ensuring continuous solar illumination throughout the 13 operating days. This allows the solar panels to operate during all static phases (stops, EVAs, sleep), significantly reducing the energy requirements of the batteries compared to polar scenarios. Temperature variations, with temperatures ranging from approximately $-173\,^{\circ}\mathrm{C}$ at night to $127\,^{\circ}\mathrm{C}$ during the day, influence the design of the thermal control system. The daily division into operational phases, guidance, rest, EVA and sleep, is shown in the Gantt chart in Figure 4.8, which highlights the repetitive structure of transfer days compared to days dedicated to EVA s on the main targets.

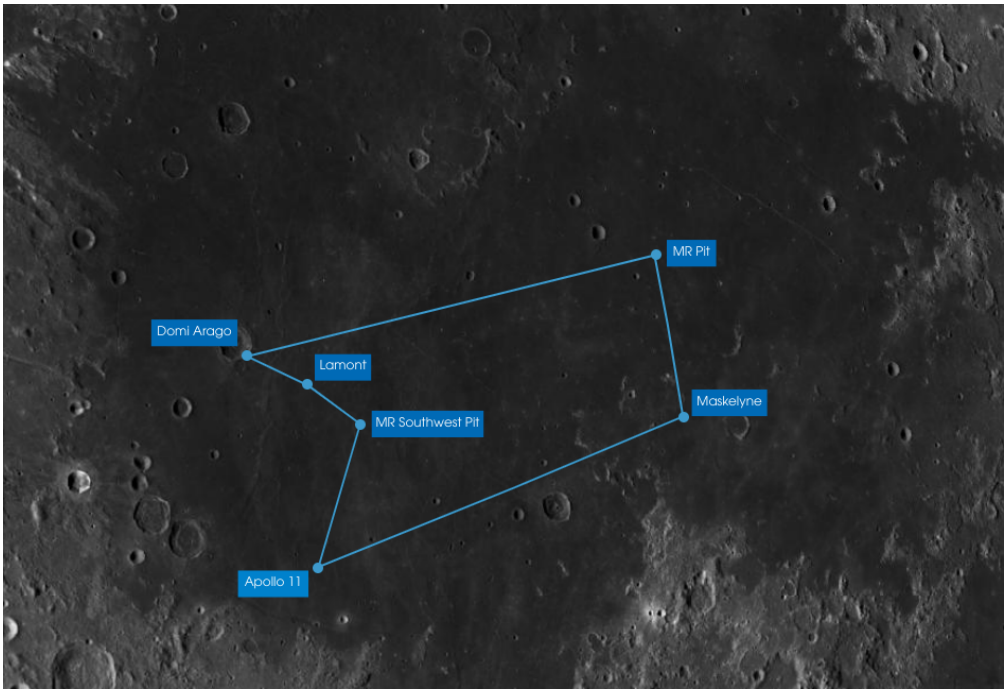

Figure 4.7: Planned rover traverse in Mare Tranquillitatis. Image background: NASA/GSFC/Arizona State University - LROC, via Lunar QuickMap.

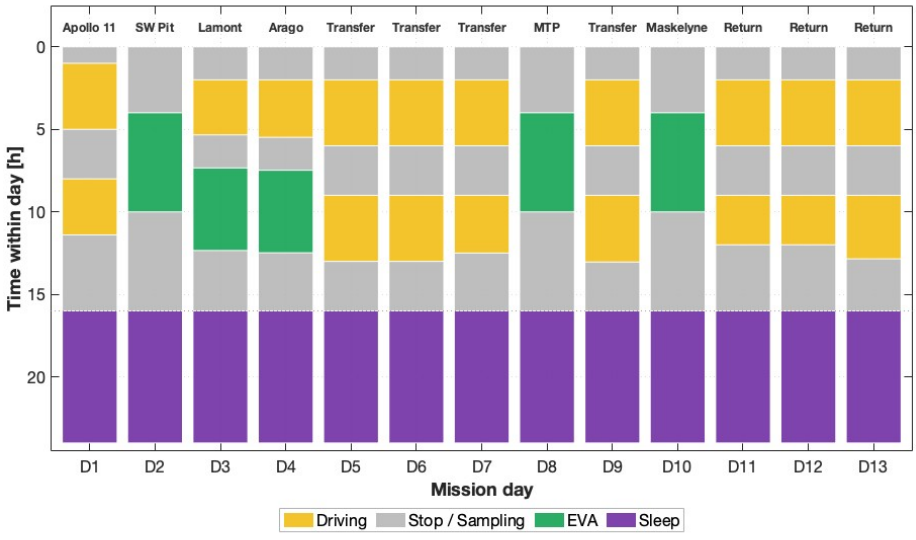

Figure 4.8: Gantt chart Mare Tranquillitatis mission timeline.

Operating Parameter	Symbol	Value	Unit
Number of astronauts	N_{crew}	2	–
Average speed	v_{avg}	15	km/h
Total mission distance	d_{tot}	1014	km
Payload	m_{payload}	100	kg
Environmental Parameter	**Symbol**	**Value**	**Unit**
External temperature (hot case)	$T_{\text{ext,hot}}$	380	K
Internal rover temperature	T_{int}	295	K
Illumination	–	Continuous (SUN)	–
Time Parameter	**Symbol**	**Value**	**Unit**
Mission duration	t_{mission}	13	days
Total driving hours	t_{drive}	67.6	h
EVA hours per EVA	t_{EVA}	5–6	h
Sleeping hours per day	t_{sleep}	8	h
Number of EVA s	N_{EVA}	5	–
Mobility System Parameter	**Symbol**	**Value**	**Unit**
Number of wheels	N_{wheels}	6	–
Wheel diameter	D	1.2	m
Wheel width	b	0.3	m
Terrain Parameter	**Symbol**	**Value**	**Unit**
Terrain type	–	Mare Tranquillitatis	–
Slope range	θ	$[-5.8°,\ +4.6°]$	deg
Slope 5%–95% percentile	–	$[-1.3°,\ +1.2°]$	deg

Table 4.4: Mission parameters Mare Tranquillitatis scenario.

The slope profile and altitude profile along the route are shown in Figure 4.9. The slopes remain within $\pm 5°$ for almost the entire route, confirming the flat nature of the basalt terrain of the sea. The altimetric profile shows limited variations in altitude, with a total difference in height of approximately 1700 m distributed over more than 1000 km of route, which translates into very low average slopes and favourable mobility conditions for the entire mission.

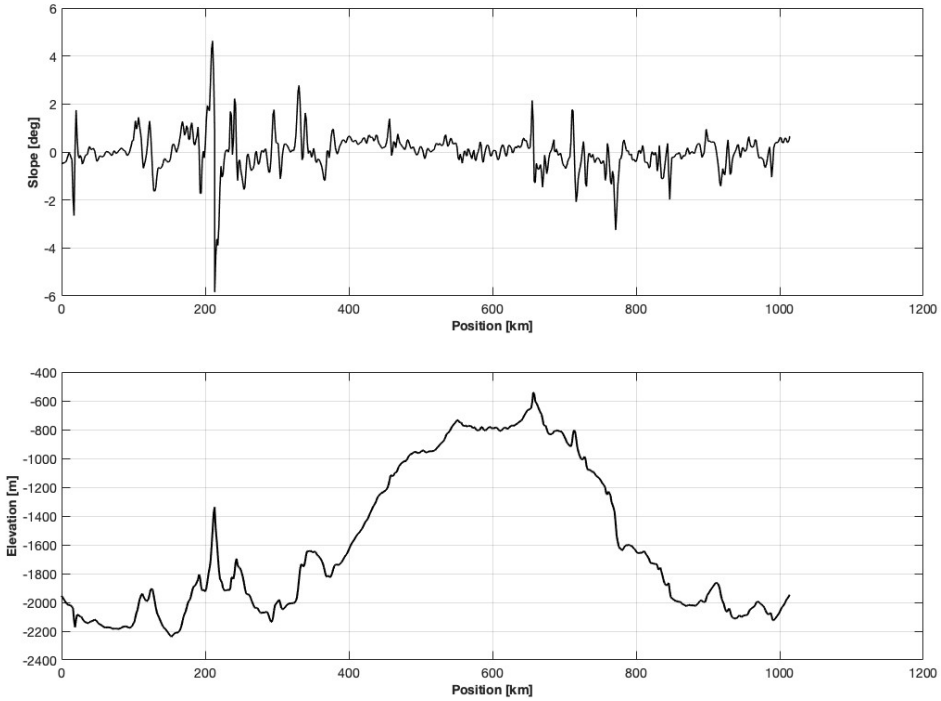

Figure 4.9: Slope profile (top) and elevation profile (bottom) along the Mare Tranquillitatis traverse.

The mass breakdown of the rover for the Mare Tranquillitatis mission is shown in Figure 4.10. The resulting total mass is approximately 2346 kg, dominated by the structural subsystem (757 kg) and the ECLSS (568 kg), which together account for more than half of the total mass. The batteries (382 kg) are significant despite the availability of continuous lighting: with approximately 67 hours of total driving time, the energy deficit accumulated during the mobility phases (when the solar panels are off) still requires considerable storage capacity. However, the most characteristic element of this scenario is the lightness of the solar panels (54 kg): thanks to continuous solar illumination throughout the mission, the time available for recharging is maximised.

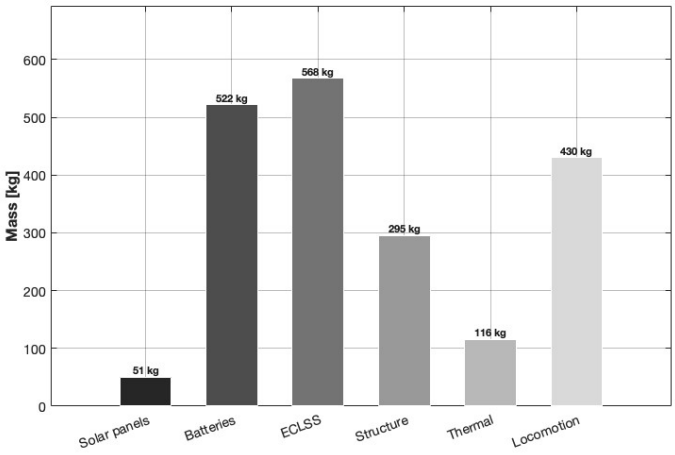

Figure 4.10: Mass breakdown of the rover for the Mare Tranquillitatis mission.

The actual profile of the battery energy balance $\Delta E_{\text{batt}}(t)$, initialised at zero, is shown in Figure 4.11. The simulation starts from zero so that negative excursions directly represent the energy debt that the battery must cover: the maximum energy deficit E_{deficit}, used to size the battery pack, corresponds to the deepest negative excursion, reached at the end of Day 1. The graph shows the variation in energy stored over time: the descents correspond to the driving phases, during which the solar panels are off and the batteries supply energy, while the ascents correspond to the static phases, i.e. stops, EVA and sleep, during which the panels recharge the batteries. The cycles have different amplitudes depending on the operational mix of each day. On transfer days, driving hours are at their maximum and ΔE_{batt} does not fully recover between driving phases on the same day, generating cycles with wider excursions. On EVA days, driving hours are reduced and the long static phases allow for more complete recharging, producing more pronounced rises.

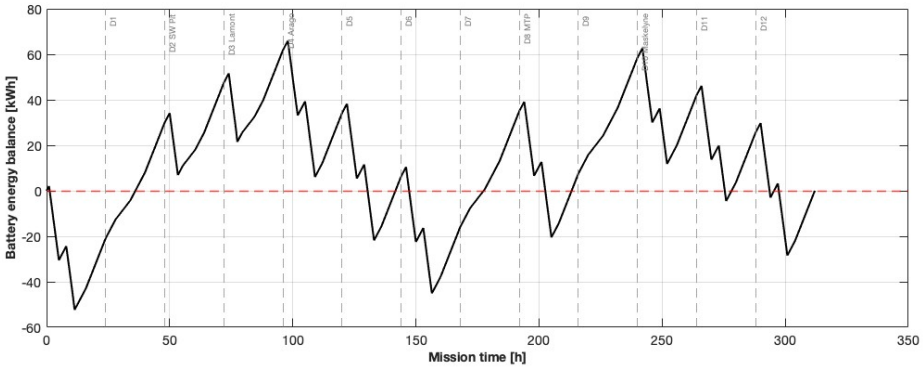

Figure 4.11: Battery energy balance profile over the Mare Tranquillitatis mission

Figure 4.12 shows the power profile for Day 6 of the Mare Tranquillitatis mission. The day includes two driving phases separated by a rest period, followed by a final rest and sleep phase. During driving, the consumed power reaches approximately 9 kW, with small fluctuations reflecting the slight terrain variations characteristic of the mare region. Solar generation drops to zero during driving, as the panels are inactive while the rover is in motion, but resumes immediately during all static phases since the mission operates under continuous solar illumination throughout the entire lunar day. During the sleep phase, consumption drops to its minimum value, while the solar panels continue to recharge the batteries.

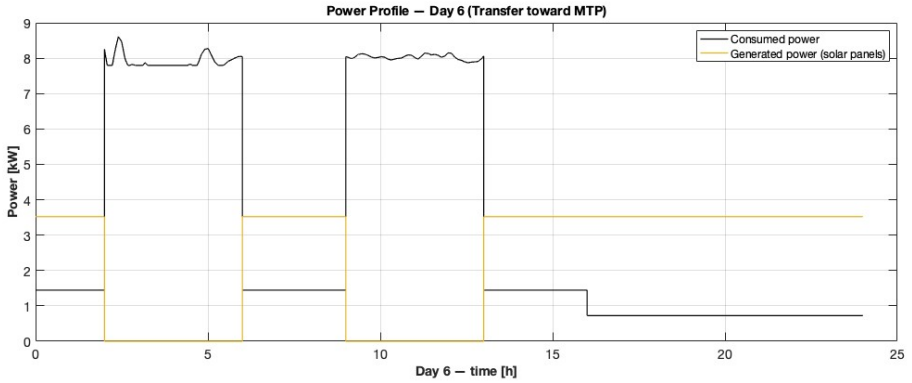

Figure 4.12: Power profile for Day 6 of the Mare Tranquillitatis mission

4.4.3 Nobile Crater

The *Nobile Crater* is located near the lunar south pole, at approximately 85° south latitude, and is characterised by a complex morphology typical of polar regions. The crater was formed by a high-energy impact and has a complex morphological structure, with discontinuous crater rims and a floor that remains

permanently in shadow in some areas. The combination of steep slopes and uneven terrain poses a significant challenge for rover mobility systems, which must ensure adequate traction, stability and power management even in challenging topographical conditions. From an environmental point of view, the region is characterised by an uneven distribution of sunlight. Some portions of the crater rim may benefit from prolonged periods of exposure to light, while large areas of the floor and inner walls fall within the so-called PSR, where direct solar radiation never reaches the surface. These conditions require particularly careful energy management of the rover. In addition, PSRs are also of considerable scientific interest, as the extremely low temperatures that characterise these regions allow for the possible preservation of water ice and other volatile compounds in the subsoil.[37]

In the scenario analysed, the rover's route starts from one of the landing sites identified for the Artemis programme in 2024, located on the rim of the Nobile crater.[43] The main parameters of the mission are shown in Table 4.5. From the landing site (Nobile Rim 1), the rover travels along the crater rim, connecting three extravehicular activity (EVA) sites. The route involves a descent along the inner walls of the crater to reach three PSR, before climbing back up and returning to the starting site. The total distance of the journey is approximately 63 km, spread over four operational days. As mentioned above, the PSRs have conditions that favour the preservation of water ice and other volatiles in the surface regolith. For this reason, the three EVA sites have been deliberately selected in these areas, with the aim of sampling the regolith and verifying its ice content, a resource of great interest for future manned lunar missions. Along the route, there are sections with slopes that can reach values of around $\pm 30°$, with frequent transitions between illuminated and shaded areas. The route of the Nobile Rim mission is illustrated in Figure 4.13. The green box shows an enlargement of the starting area at the edge of the crater, while the red outlines highlight the permanently shaded regions crossed by the rover. The daily breakdown of activities is shown in the Gantt chart in Figure 4.14.

Operating Parameter	Symbol	Value	Unit
Number of astronauts	N_{crew}	2	–
Average speed	v_{avg}	10	km/h
Total mission distance	d_{tot}	63	kilometres
Payload	m_{payload}	50	kilograms
Environmental Parameter	**Symbol**	**Value**	**Unit**
External temperature (hot case)	$T_{\text{ext,hot}}$	100	K
Internal rover temperature	T_{int}	295	K
Illumination	–	Mixed (SUN/DARK)	–
Time Parameter	**Symbol**	**Value**	**Unit**
Mission duration	t_{mission}	4	days
Total driving hours	t_{drive}	6.27	h
EVA hours per EVA	t_{EVA}	6	h
Sleeping hours per day	t_{sleep}	8	h
Number of EVA s	N_{EVA}	3	–
Mobility System Parameter	**Symbol**	**Value**	**Unit**
Number of wheels	N_{wheels}	6	–
Wheel diameter	D	1.2	m
Wheel width	b	0.3	m
Terrain Parameter	**Symbol**	**Value**	**Unit**
Terrain type	–	Nobile Rim	–
Slope range	θ	$[-30°,\ +30°]$	deg
Slope 5%–95% percentile	–	$[-26°,\ +25°]$	deg

Table 4.5: Mission parameters Nobile Rim scenario.

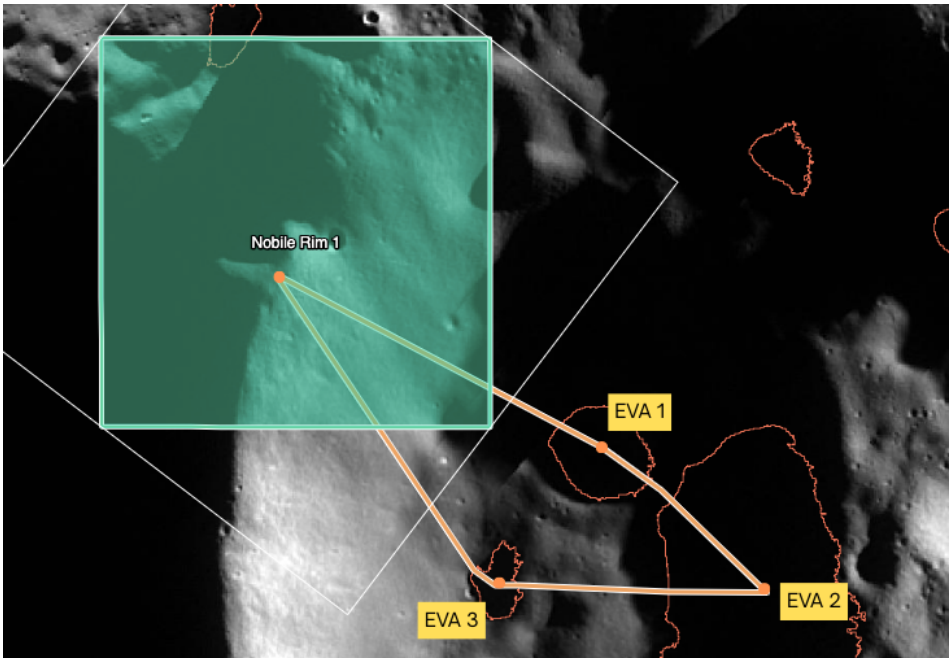

Figure 4.13: Planned rover traverse along the Nobile Rim. Image background: NASA/GSFC/Arizona State University - LROC, via Lunar QuickMap.

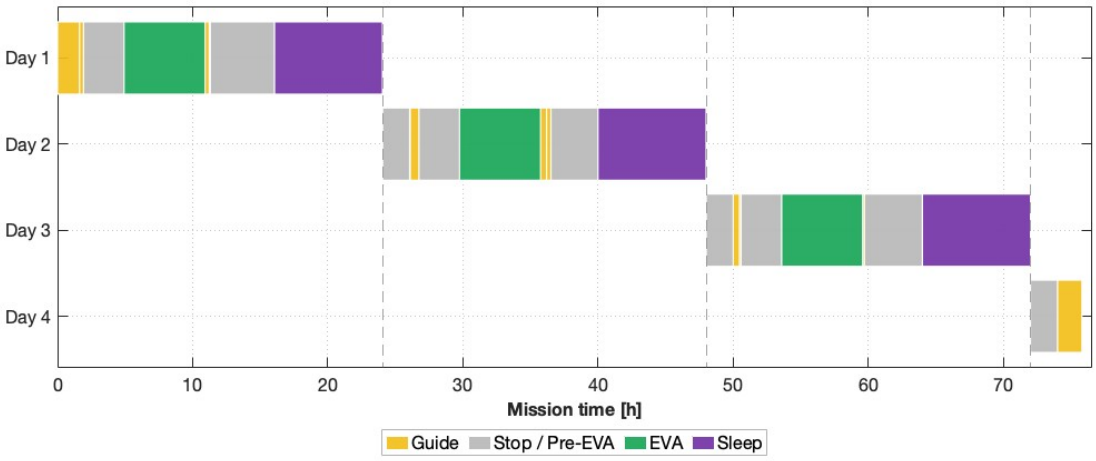

Figure 4.14: Gantt chart Nobile Rim mission timeline

The slope profile and altimetric profile along the route of the Nobile Crater are shown in Figure 4.15. The altitude profile clearly shows the morphological structure of the crossing: the rover starts from the crater rim at about 6000 m, descends to the bottom at about -1000 m along the inner walls, crosses the valley floor in the PSR areas and finally climbs back up the side to the starting point. The total elevation difference is approximately 7000 m distributed over only 63 km of route.

The slope profile reflects this morphology with significant variations: the initial descent and final ascent phases have steep slopes, with values reaching ±30°, while the central area of the valley floor has more moderate but still irregular slopes, typical of crater terrain.

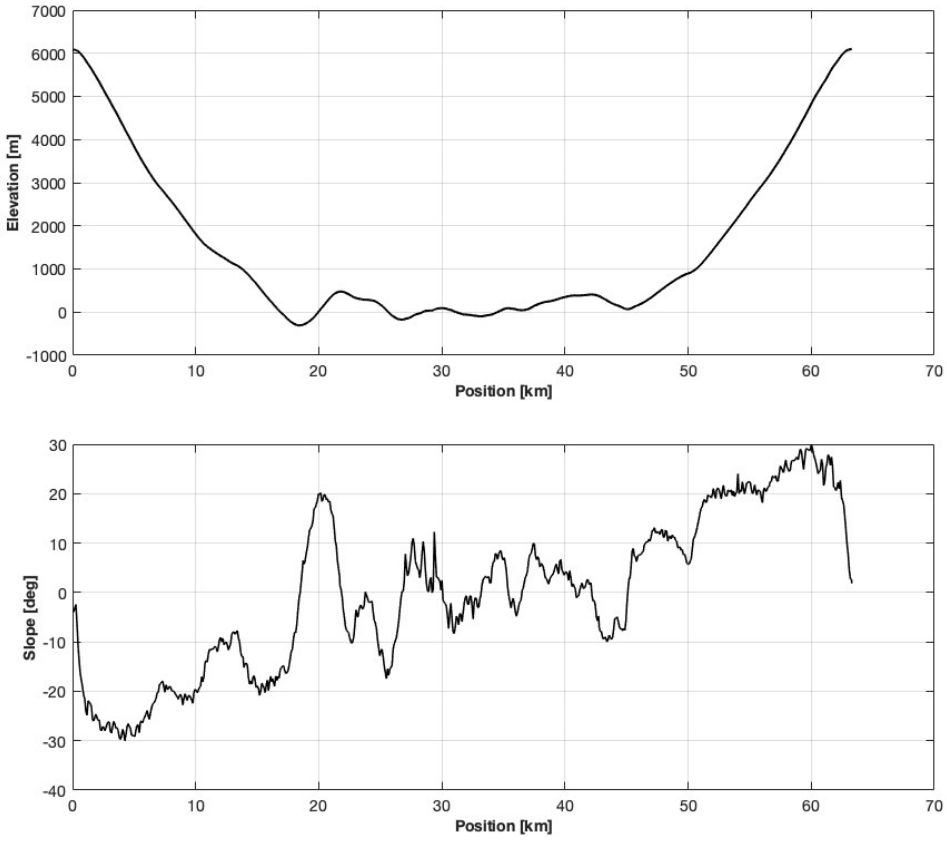

Figure 4.15: Elevation profile (top) and slope profile (bottom) along the Nobile Rim traverse. The route covers approximately 63 km, descending from the crater rim to the floor and returning to the departure point.

The mass breakdown of the rover for the Nobile Rim mission is shown in Figure 4.16. The total mass converges to approximately 1324 kg. The structural subsystem (382 kg) and the locomotion subsystem (397 kg) represent the dominant

contributions, with locomotion exceeding the structure due to steep slopes up to ±30° that require greater traction capacity than flat terrain. The ECLSS (175 kg) is contained due to the short operational duration of 4 days. The solar panels (45 kg) and batteries (196 kg) reflect the energy balance of a short mission with partial illumination.

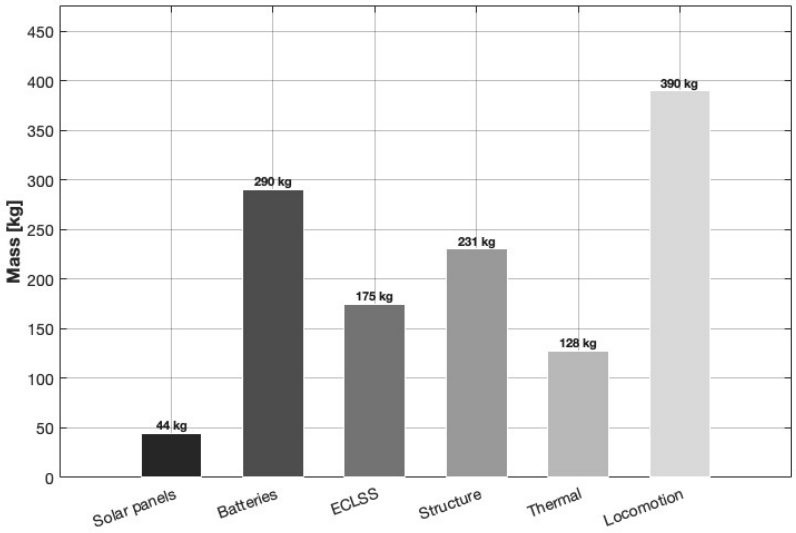

Figure 4.16: Mass breakdown of the rover for the Nobile Rim mission.

The battery energy balance $\Delta E_{\text{batt}}(t)$ for the Nobile Rim mission, initialised at zero, is shown in Figure 4.17. The deepest negative excursion, corresponding to the maximum energy deficit, is reached at the end of Day 1 at approximately 11 h, corresponding to the longest driving phase.

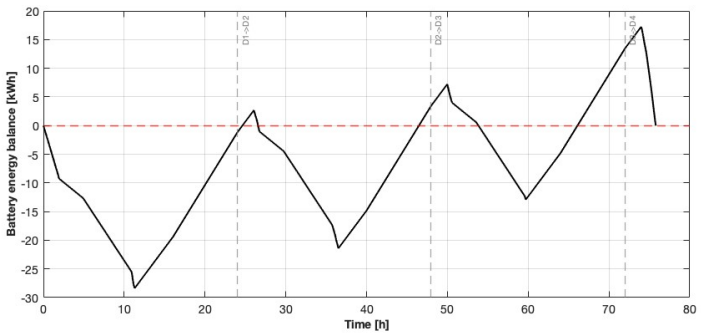

Figure 4.17: Battery energy balance $\Delta E_{\text{batt}}(t)$ over the Nobile Rim mission

The profile shows a cyclical trend over four operating days, with descents during driving phases and ascents during stops, EVAs and sleep. In the following days,

ΔE_{batt} tends to recover progressively: the end-of-day stops and sleep phases were deliberately planned to coincide with the illuminated sections of the route, allowing the solar panels to recharge the batteries during hours of inactivity. This approach maximises the available energy recovery and explains the pronounced rises during the stop and sleep phases.

Figure 4.18 presents the power profile for Day 2 of the Nobile Rim mission. The two driving phases are clearly distinguishable by the sharp spikes in power consumption. The jagged nature of the profile during these periods reflects variations in terrain slope: steeper segments demand greater traction, causing instantaneous peaks in the locomotion subsystem's power requirements. During driving, solar generation drops to zero, as the panels are assumed to be inactive while the rover is in motion. During the EVA phase, power consumption stabilizes at an intermediate level, supporting life support, communications, and scientific instruments. Solar generation is active only when illumination conditions allow. Finally, the sleep phase at the end of the day exhibits the lowest power demand, corresponding to minimal subsystem activity, while the solar panels continue to recharge the batteries in preparation for the next day.

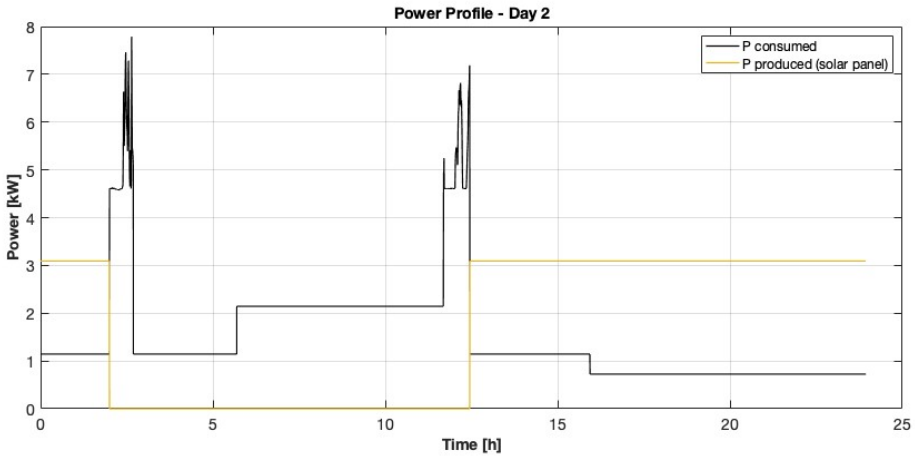

Figure 4.18: Power profile for Day 2 of the Nobile Rim mission

Chapter 5

Optimisation

This chapter presents the formulation and solution of the optimisation problem developed to determine the minimum-mass configuration of the crewed lunar rover. The mathematical model, design variables, constraints, and the numerical strategy adopted for the global minimum search are described. The optimisation framework implemented in this work can be interpreted as a multidisciplinary design optimisation (MDO) problem, in which several subsystem sizing models, including structural, thermal, mobility, and energy systems, are coupled through the rover mass and energy balance [6]. Such approaches are commonly adopted in conceptual design studies where interactions among subsystems introduce nonlinear dependencies between design variables and system-level performance.

5.1 Problem Formulation

5.1.1 Objective Function

The objective of the optimisation process is the minimisation of the total rover mass, evaluated through the function

$$\min_{\mathbf{x}} \; f(\mathbf{x}) = m_{\text{rover}}(\mathbf{x}) \tag{5.1}$$

where $\mathbf{x}$ denotes the vector of design variables and $m_{\text{rover}}(\mathbf{x})$ is computed using the integrated multidisciplinary analysis model developed in this work.

The total rover mass is expressed as the sum of the masses of the main subsystems:

$$m_{\text{rover}} = M_{\text{fixed}} + M_{\text{structure}} + M_{\text{mobility}} + M_{\text{thermal}} + M_{\text{energy}} + M_{\text{ECLSS}} + M_{\text{payload}} \tag{5.2}$$

Each subsystem mass is evaluated using the analytical and semi-empirical models described in Chapter 2. These models are internally coupled, since several subsystem masses depend on the total vehicle mass through power demand and structural loading. The multidisciplinary analysis therefore includes an internal iterative sizing loop to converge the rover mass (Chapter 2).

5.1.2 Design Variables

The design variable vector consists of five geometric parameters related to the wheel geometry and to the overall geometry of the pressurised rover structure. Each variable is subject to lower (lb) and upper (ub) bounds defined by mission requirements.

Table 5.1: Design variables, bounds, and initial point

Sym.	Variable	Description	Unit	lb	ub	x_0
x_1	D_{wheels}	Wheel diameter	m	0.5	1.2	1.0
x_2	b_{wheels}	Wheel width	m	0.2	0.5	0.3
x_3	R_{rover}	Rover radius	m	1.1	2.5	1.6
x_4	L_{rover}	Rover length	m	3.0	7.0	5.0
x_5	h_{floor}	Floor height	m	0.1	0.8	0.7

The initial point x_0 represents a first engineering estimate consistent with short-range mission requirements, ensuring feasibility of the initial configuration and facilitating solver convergence.

5.1.3 Constraints

The optimisation problem is subject to four nonlinear inequality constraints. These constraints derive directly from habitability standards and subsystem accommodation requirements. The internal volume of the rover is divided into two regions:

- an upper volume, corresponding to the habitable compartment accessible to the crew;
- a sub-floor volume, located below the internal floor and used to accommodate technical subsystems such as batteries and the Environmental Control and Life Support System (ECLSS).

The habitable compartment must satisfy the minimum volume requirements derived in Section 2.4.2, while the sub-floor region must provide sufficient space for the integration of the required subsystems. The minimum floor area constraint (c_2) imposes a walkable surface of $S_{\min} = 4\,\text{m}^2$ per crew member. Although no

dedicated standard exists for pressurised rover floor area, this value is consistent with the minimum living space of $4\,\mathrm{m}^2$ per person recommended by the Council of Europe for confined multi-occupancy environments intended for prolonged human habitation [44]. The headroom constraint (c_3) requires that at least 75 % of the floor area has a clear height of at least 2 m above the floor level, ensuring that the crew can stand upright and perform daily operational and scientific activities throughout the habitable compartment.[15]. In the optimisation formulation, the constraints are expressed in the standard inequality form:

$$c_i(\mathbf{x}) \leq 0 \qquad i = 1, \ldots, 4 \tag{5.3}$$

where $\mathbf{x}$ is the vector of design variables. A configuration is considered feasible when all constraints satisfy this condition.

Constraint	Mathematical expression
Minimum habitable volume	$V_{\text{upper}} \geq V_{\text{hab}}(t_{\text{mission}}) \cdot N_{\text{crew}}$
Minimum floor area	$S_{\text{floor}} \geq S_{\text{min}} \cdot N_{\text{crew}}$
Minimum headroom	$A_{h \geq 2\,\text{m}} \geq 0.75 \cdot S_{\text{floor}}$
Sub-floor accommodation	$V_{\text{sub}} \geq V_{\text{bat}} + V_{\text{ECLSS}}$

Table 5.2: Design constraints

For implementation within the optimisation solver, the previous conditions are reformulated as nonlinear constraint functions:

$$c_1(\mathbf{x}) = V_{\text{hab}}(t_{\text{mission}}) N_{\text{crew}} - V_{\text{upper}} \leq 0 \tag{5.4}$$
$$c_2(\mathbf{x}) = S_{\text{min}} N_{\text{crew}} - S_{\text{floor}} \leq 0 \tag{5.5}$$
$$c_3(\mathbf{x}) = 0.75\, S_{\text{floor}} - A_{h \geq 2\,\text{m}} \leq 0 \tag{5.6}$$
$$c_4(\mathbf{x}) = V_{\text{bat}} + V_{\text{ECLSS}} - V_{\text{sub}} \leq 0 \tag{5.7}$$

5.2 Optimisation Method

5.2.1 Sequential Quadratic Programming (SQP) Algorithm with `fmincon`

The optimisation problem is solved in the MATLAB environment using the `fmincon` solver [45] with the SQP algorithm [46]. SQP is particularly well suited for nonlinear optimisation problems with differentiable objective functions, constraints and a moderate number of design variables. At each iteration the method solves a quadratic approximation of the Lagrangian function subject to a linearisation

of the constraints. The Hessian of the Lagrangian is approximated using the BFGS update formula, and convergence is certified through satisfaction of the Karush-Kuhn-Tucker optimality conditions. The solver configuration adopted is:

- `MaxFunctionEvaluations` = 2000
- `MaxIterations` = 1000
- `OptimalityTolerance` = 10^{-6}
- `ConstraintTolerance` = 10^{-6}
- `StepTolerance` = 10^{-8}

5.2.2 MultiStart Strategy for Global Minimum Search

The objective function is highly nonlinear because several subsystem models introduce strong couplings and nonlinear behaviours. As a result, the optimisation landscape may contain multiple local minima.

To improve the robustness of the optimisation process, the MultiStart algorithm from the MATLAB Global Optimization Toolbox is adopted [47].

This strategy generates multiple starting points within the feasible domain [lb, ub], launches an independent local optimisation from each point using `fmincon`, and finally selects the best feasible solution among all local optima found. Computing is enabled through the option `UseParallel = true`, allowing the local optimisations to be distributed across the available processor cores. A value of $N_{\text{start}} = 500$ was adopted as a reasonable compromise between solution quality and computational cost.

The overall optimisation process is illustrated in Figure 5.1. For each combination of eclipse condition and number of wheels, the MultiStart algorithm generates a set of starting points and launches independent SQP runs. Each evaluation of the objective function triggers a complete multidisciplinary analysis of the rover, including the sizing of all subsystems and the verification of the constraints. The best feasible solution across all local runs is then stored and used to produce the mass breakdown results.

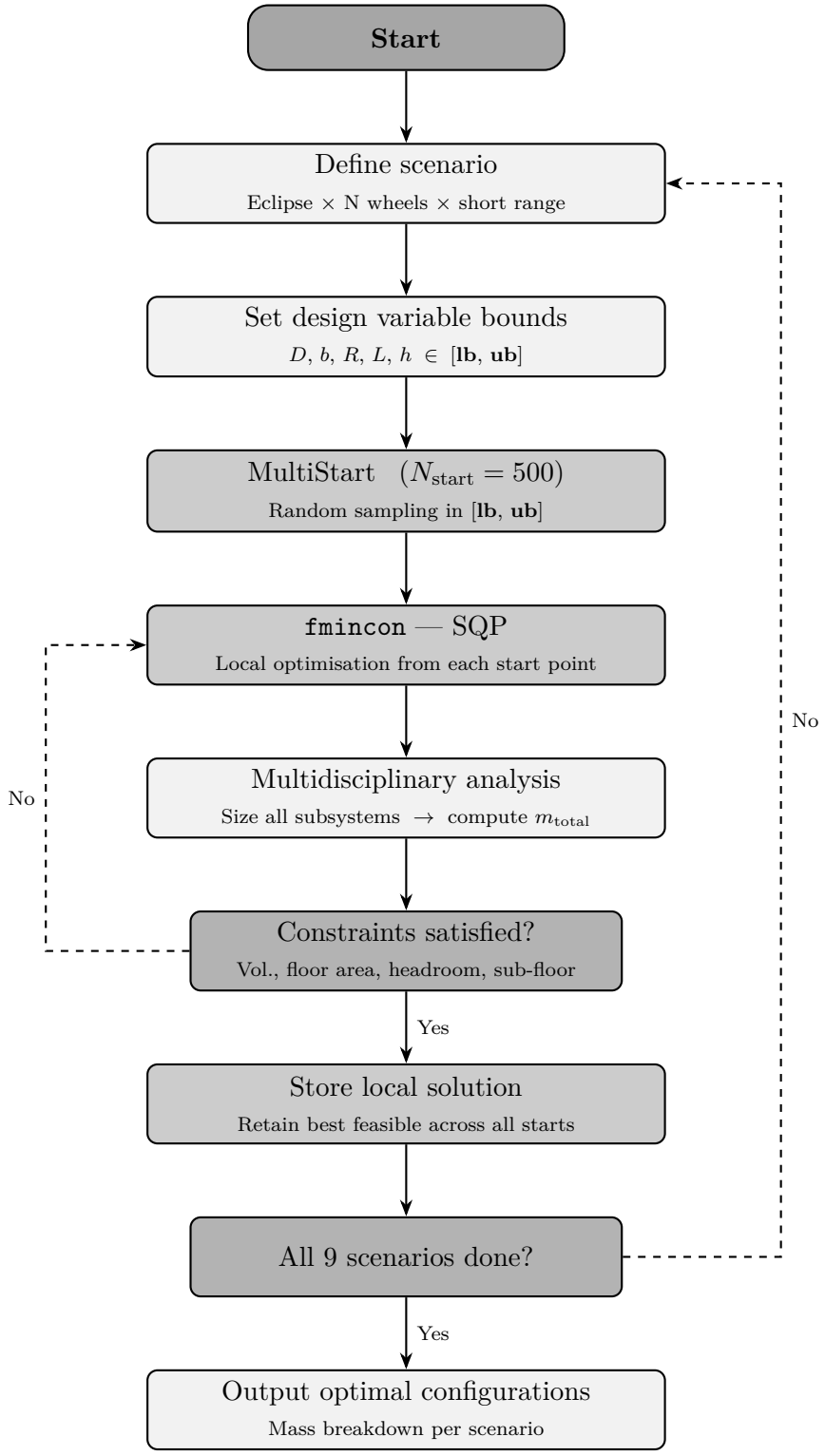

Figure 5.1: Optimisation process flowchart.

5.3 Mission Parameters

The optimisation is performed over a matrix of nine scenarios, defined by the combination of three eclipse conditions and three wheel configurations, all within the short-range mission. Table 5.3 summarises the combinations explored.

Dimension	**Values**
Mission type	Short range
Eclipse condition	No eclipse, Partial eclipse, Total eclipse
Number of wheels	4, 6, 8
Total combinations	**9**

Table 5.3: Optimisation scenario matrix.

The short-range mission parameters are those defined in Table 4.1. The eclipse condition determines the hours of darkness per day and directly drives the battery sizing: in the no-eclipse scenario the batteries are sized only to cover the driving phase, while in the partial and total eclipse scenarios they must additionally guarantee the energy supply to all subsystems during the unavailability of solar radiation. The number of wheels affects the mobility system mass and the traction performance on the lunar regolith, as discussed in Section 2.4.1.

5.4 Results

This section presents the results of the optimisation campaign conducted over the nine scenarios defined in Section 5.3. For each combination of eclipse condition and wheel configuration, the optimal design variable values, total rover mass, and subsystem mass breakdown are reported and discussed.

Table 5.4 summarises the optimal total mass and design variable values obtained for each of the nine scenarios.

Eclipse	**Wheels**	m^* [kg]	D^* [m]	b^* [m]	R^* [m]	L^* [m]	h^* [m]
No eclipse	4	4747	0.904	0.202	1.316	6.183	0.633
No eclipse	6	4740	0.624	0.201	1.324	6.123	0.648
No eclipse	8	4733	0.613	0.207	1.327	6.165	0.653
Partial	4	4829	0.777	0.201	1.311	6.227	0.622
Partial	6	4798	0.834	0.203	1.255	6.751	0.511
Partial	8	4790	0.559	0.205	1.324	6.131	0.646
Total	4	6635	0.999	0.353	1.321	6.527	0.551
Total	6	6503	0.769	0.289	1.261	6.708	0.521
Total	8	5359	1.091	0.202	1.317	6.214	0.629

Table 5.4: Optimal total mass and design variable values for all nine scenarios.

5.4.1 Effect of Number of Wheels

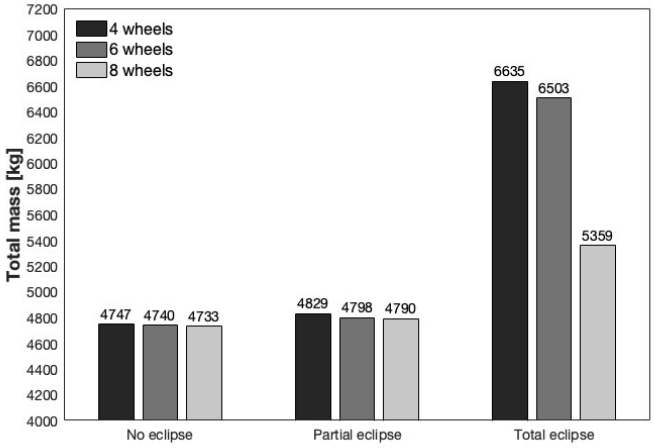

Figure 5.2: Rover mass as a function of wheel configuration.

Figure 5.2 compares the total rover mass across the three wheel configurations for each eclipse condition. In all scenarios, increasing the number of wheels reduces the total mass, making the 8-wheel configuration optimal for the short-range mission. This trend arises because more wheels lower the load per wheel, decreasing contact pressure on the regolith and resistance to motion, which reduces the electrical power required by the locomotion system and, consequently, the energy system mass through the iterative mass convergence loop. The effect is particularly pronounced in the total eclipse scenario, where the energy system dominates the rover mass. A preliminary parametric sweep on the short-range mission baseline (Figure 5.3) confirms this monotonic decrease independently of the eclipse condition.

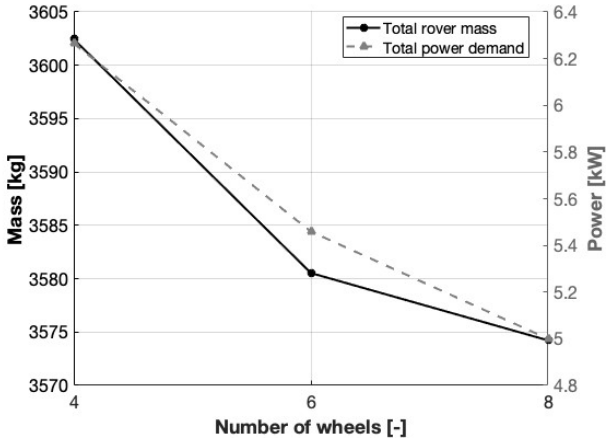

Figure 5.3: Total mass and total power as a function of wheel configuration.

5.4.2 Effect of Wheel Geometry

The optimal wheel diameter D^* and width b^* do not show a clear trend across scenarios. Unlike the number of wheels, these variables are not monotonically related to total rover mass. For a given number of wheels and a fixed wheel width b, a well-defined wheel diameter D exists that minimizes the total rover mass, and the optimiser consistently identifies this optimum. This behaviour is illustrated in Figure 5.4 for the short-range mission with 4 wheels.

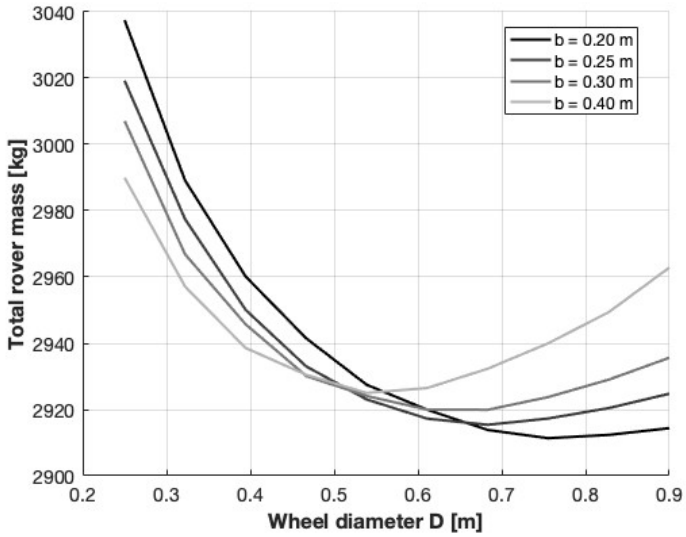

Figure 5.4: Total rover mass as a function of wheel diameter D for several values of wheel width b, short-range mission baseline with 4 wheels.

5.4.3 Effect of Rover Geometry

The optimal values of rover radius R^*, rover length L^*, and floor height h^* do not exhibit a clear trend across scenarios. Unlike the wheel geometry variables, these parameters are primarily governed by the habitability and sub-floor accommodation constraints, which force the optimiser to recover feasible configurations rather than to follow a monotonic minimisation path. Figure 5.5 shows the three-dimensional geometry of the optimal pressurised hull for the no-eclipse, 4-wheel scenario, corresponding to the values $R^* = 1.316\,\mathrm{m}$, $L^* = 6.183\,\mathrm{m}$, and $h^* = 0.633\,\mathrm{m}$.

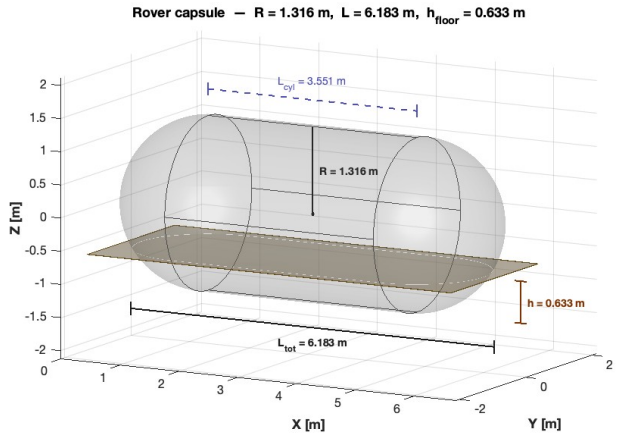

Figure 5.5: Three-dimensional geometry for the no-eclipse, 4-wheel scenario.

Chapter 6

Conclusions

This thesis presented a MDO framework for a pressurized lunar rover, intended to support long-duration manned surface exploration missions under the Artemis program. The work fills a gap identified in the existing literature: the absence of an integrated parametric tool capable of simultaneously sizing the rover's main subsystems, managing their mutual interdependencies, and incorporating a level of optimization already in the conceptual design phase.

6.1 Summary of Contributions

The framework was developed around an iterative mass convergence methodology inspired by multidisciplinary design practices typical of aeronautical engineering [6] and adapted to the specific constraints of the lunar environment. Starting from a set of operational, environmental, and performance requirements, the model sizes five interdependent subsystems: the locomotion system, the pressurized structure, the power system, the ECLSS, and the thermal control system, and iterates until the total mass balance converges.

The model operates at the conceptual design level, and several simplifications have been introduced to maintain computational efficiency. The tool's modular architecture, implemented entirely in MATLAB, allows each subsystem to be refined independently without compromising the consistency of the overall design. The parametric nature of the model allows for rapid exploration of the design space across a wide range of mission scenarios, making it suitable for comparative evaluation of different configurations during the preliminary design phase. A sensitivity analysis was conducted to assess the influence of key mission parameters, such as crew size, mission duration, average speed, and external temperatures, on the rover's total mass and energy requirements. Several mission scenarios were also simulated: three educational ones and two more realistic ones, namely a crossing

of the Mare Tranquillitatis region and an excursion to Nobile Crater at the lunar south pole. Finally, a system-level optimization was performed for the short-range mission scenario, considering three eclipse conditions and three wheel configurations, for a total of nine cases. The optimization minimized the total mass of the rover, while respecting habitability and volumetric constraints, using a SQP algorithm integrated into a global MultiStart search strategy. [47].

6.2 Key Results

The sensitivity analysis highlighted several key design drivers affecting the rover configuration. Crew size introduces a non-linear effect on the power-to-mass ratio: as the number of astronauts increases, the mass initially grows faster than the power demand, up to a threshold beyond which the additional power required for a larger crew dominates. This produces a minimum that identifies an optimal crew size, balancing total power demand and vehicle mass. Similarly, mission duration drives a structural transition in the ECLSS configuration: non-regenerative systems are sufficient for missions up to approximately 42 days, whereas longer missions benefit from a regenerative architecture. This transition leads to a noticeable step increase in battery mass, as the regenerative system imposes a continuous and significant power demand that must be met by the energy storage system. Average speed also influences the power-to-mass ratio, increasing it monotonically and revealing a clear design trade-off: higher travel speeds reduce transit times and improve mission productivity but require substantially larger energy resources, resulting in a heavier overall rover dominated by the mobility and energy subsystems.

The three reference scenarios highlight how the total rover mass increases significantly with mission duration. In the absence of eclipses, short-range missions are primarily governed by the structural and locomotion subsystems. As mission duration increases, the ECLSS progressively becomes the dominant contributor to the overall mass. For the longest missions, the energy storage system grows to a level comparable to the ECLSS, reflecting the increasing importance of sustaining long-term operations.

The introduction of eclipses has a strong impact on the energy system. Reduced solar availability requires larger battery capacity even for short missions, while a total eclipse eliminates solar power generation entirely, forcing the batteries to supply the full mission energy demand and significantly increasing the overall rover mass. This effect becomes particularly severe for medium-duration missions, where the energy storage system alone can represent the majority of the total vehicle mass. As a result, a battery-based architecture remains feasible primarily for short- to medium-duration missions with limited eclipse exposure, while its practicality progressively decreases as mission duration increases and solar availability

diminishes.

The system-level optimization, conducted across multiple combinations of eclipse conditions and wheel configurations for the short-range mission, consistently identified the configuration with the highest number of wheels as the minimum-mass solution. This result is explained by the reduced load carried by each wheel, which lowers contact pressure on the regolith and consequently decreases rolling resistance and locomotion power demand. Through the iterative coupling loop, the lower power requirement translates into a reduction of the energy subsystem mass, an effect that becomes particularly relevant under eclipse conditions.

6.3 Future Developments

From a modeling perspective, the models currently adopted are based on a quasi-static sizing approach. A progressive increase in model fidelity, introducing dynamic effects, thermal transients, and a more detailed description of the physical and chemical processes within the subsystems, would help reduce uncertainties in mass and power estimates during the more advanced design phases. Furthermore, at the operational scenario simulation level, it would be interesting to include algorithms of path planning such as A* that allow for the identification of the optimal route to the EVA site.[48] From an optimization perspective, extending the analysis to medium- and long-range missions and additional realistic scenarios would allow us to evaluate how the subsystem hierarchies identified in this thesis change under different operating conditions. Including an economic dimension, through estimates of development, production, and operating costs throughout the rover's entire life cycle, would complement the mass optimization with a more comprehensive assessment of the overall feasibility of the different configurations.

Bibliography

[1] I. A. Crawford, M. Anand, C. S. Cockell, H. Falcke, D. A. Green, R. Jaumann, and M. A. Wieczorek. «Back to the Moon: The Scientific Rationale for Resuming Lunar Surface Exploration». In: *Planetary and Space Science* (2012). URL: https://arxiv.org/abs/1206.0749.

[2] *NASA's Plan for Sustained Lunar Exploration and Development*. Tech. rep. National Aeronautics and Space Administration, 2020. URL: https://www.nasa.gov/wp-content/uploads/2020/08/a_sustained_lunar_presence_nspc_report4220final.pdf.

[3] S. K. Moore and J. Marmolejo. *Extravehicular Activity (EVA) Hardware and Operations Overview*. Tech. rep. JSC-CN-26431. Houston, TX: NASA Johnson Space Center, 2012. URL: https://ntrs.nasa.gov/citations/20120011735.

[4] J. J. Zakrajsek et al. *Exploration Rover Concepts and Development Challenges*. Tech. rep. NASA/TM-2005-213555. AIAA–2005–2525. Cleveland, Ohio: NASA Glenn Research Center, 2005. URL: https://ntrs.nasa.gov/api/citations/20050175879/downloads/20050175879.pdf.

[5] G. H. Heiken, D. T. Vaniman, and B. M. French, eds. *Lunar Sourcebook: A User's Guide to the Moon*. Cambridge, UK: Cambridge University Press, 1991. URL: https://www.lpi.usra.edu/publications/books/lunar_sourcebook/pdf/LunarSourceBook.pdf.

[6] J. R. R. A. Martins and A. B. Lambe. «Multidisciplinary Design Optimization: A Survey of Architectures». In: *AIAA Journal* 51.9 (2013), pp. 2049–2075. DOI: 10.2514/1.J051895.

[7] National Aeronautics and Space Administration. *NASA-STD-3001, Volume 1, Revision B: NASA Space Flight Human-System Standard: Crew Health*. NASA Technical Standard NASA-STD-3001. National Aeronautics and Space Administration, 2022. URL: https://www.nasa.gov/reference/nasa-std-3001v1/.

[8] D. Coan. *NASA Exploration EVA System Concept of Operations Summary for Artemis Phase 1 Lunar Surface Mission*. Tech. rep. EVA-EXP-0075. Houston, TX: NASA Johnson Space Center, 2020. URL: https://www.nasa.gov/wp-content/uploads/2020/01/topic_1-_eva_lunar_surface_concept_of_operations.pdf.

[9] M. Bhardwaj, V. Bulsara, D. Kokan, S. Shariff, E. Svarverud, and R. Wirz. *Design of a Pressurized Lunar Rover: Final Report*. Senior Design Project Report S 1/b. USRA/NASA/VPI&SU Collaboration. Advisors: Prof. A. Jakubowski and D. A. Hayness. Virginia Polytechnic Institute, State University, Department of Aerospace, and Ocean Engineering, 1992. URL: https://ntrs.nasa.gov/citations/19930008827.

[10] Z. Q. Li and L. K. Bingham. *Terramechanics for LTV Modeling and Simulation*. White Paper. National Aeronautics and Space Administration. URL: https://ntrs.nasa.gov/api/citations/20220010732/downloads/Terramechanics_white_paper.pdf.

[11] V. Asnani, D. Delap, and C. Creager. *The Development of Wheels for the Lunar Roving Vehicle*. Tech. rep. NASA/TM-2009-215798. Cleveland, Ohio, USA: National Aeronautics and Space Administration (NASA), 2009. URL: https://ntrs.nasa.gov/api/citations/20100000019/downloads/20100000019.pdf.

[12] S. J. Hoffman and L. Toups. *Evolvable Mars Campaign Development*. Presentation at the NSF Large Facility Workshop. Washington, DC: NASA Johnson Space Center and Science Applications International Corporation, 2016. URL: https://ntrs.nasa.gov/api/citations/20160006342/downloads/20160006342.pdf.

[13] W. C. Young and R. G. Budynas. *Roark's Formulas for Stress and Strain*. 8th ed. McGraw-Hill, 2012.

[14] The Aluminum Association, Inc. *Aluminum Standards and Data 2000*. The Aluminum Association, 2000. URL: https://asm.matweb.com/search/SpecificMaterial.asp?bassnum=MA7075T73.

[15] National Aeronautics and Space Administration. *Human Integration Design Handbook (HIDH)*. Revision 1. NASA/SP-2010-3407/REV1. Supersedes Baseline issued January 27, 2010. NASA. Washington, DC, 2014. URL: https://www.nasa.gov/wp-content/uploads/2015/03/human_integration_design_handbook_revision_1.pdf.

[16] American Society of Mechanical Engineers. *ASME Boiler and Pressure Vessel Code, Section VIII: Rules for Construction of Pressure Vessels, Division 1*. New York, NY: ASME, 2015.

[17] K. Cunningham, J. Carr, and B. Lewis. *MSFC Electrical Power Systems for Cubesats*. Tech. rep. National Aeronautics and Space Administration, Nov. 2018. URL: https://ntrs.nasa.gov/api/citations/20180007969/downloads/20180007969.pdf.

[18] B. McKissock, P. Loyselle, and E. Vogel. *Guidelines on Lithium-ion Battery Use in Space Applications*. Tech. rep. NASA/TM-2009-215751. Cleveland, Ohio: NASA Glenn Research Center, 2009. URL: https://ntrs.nasa.gov/api/citations/20090023862/downloads/20090023862.pdf.

[19] H. W. Jones. *Design and Analysis of a Flexible, Reliable Deep Space Life Support System*. Tech. rep. Moffett Field, CA, 94035-0001: NASA Ames Research Center. URL: https://ntrs.nasa.gov/api/citations/20160005782/downloads/20160005782.pdf.

[20] National Aeronautics and Space Administration. *Guidelines for the Assessment of Chemicals and Materials for Impacts to Environmental Control and Life Support Systems and Habitable Volumes of Crewed Spacecraft*. Technical Report JSC-66869 Baseline. Houston, Texas: Lyndon B. Johnson Space Center, Sept. 2015. URL: https://www.nasa.gov/wp-content/uploads/2023/03/eclss-assessments-sep-2015-baseline-signed.pdf.

[21] H. W. Jones. «Much Lower Launch Costs Make Resupply Cheaper Than Recycling for Space Life Support». In: *47th International Conference on Environmental Systems (ICES)*. ICES-2017-87. NASA Ames Research Center. Charleston, South Carolina, July 2017. URL: https://ntrs.nasa.gov/api/citations/20170010337/downloads/20170010337.pdf.

[22] G. J. Gentry and J. Cover. «International Space Station (ISS) Environmental Control and Life Support (ECLS) System Overview of Events: 2010–2014». In: *45th International Conference on Environmental Systems*. ICES-2015-155. 2015. URL: https://ntrs.nasa.gov/api/citations/20150022318/downloads/20150022318.pdf.

[23] J. Meseguer, I. Pérez-Grande, and A. Sanz-Andrés. *Spacecraft Thermal Control*. Woodhead Publishing in Mechanical Engineering. Woodhead Publishing, 2012. URL: https://ndl.ethernet.edu.et/bitstream/123456789/32329/1/97.pdf.

[24] M. M. Finckenor and D. Dooling. *Multilayer Insulation Material Guidelines*. Tech. rep. NASA/TP-1999-209263. Marshall Space Flight Center, Alabama, USA: NASA Marshall Space Flight Center, 1999. URL: https://ntrs.nasa.gov/api/citations/19990047691/downloads/19990047691.pdf.

[25] K. Li, J. Chen, X. Tian, and Y. He. «Study on the Performance of Variable Density Multilayer Insulation in Liquid Hydrogen Temperature Region». In: *Energies* (2022). DOI: 10.3390/en15249267. URL: https://www.mdpi.com/1996-1073/15/24/9267.

[26] M. K. Ewert, T. T. Chen, and C. D. Powell. *Life Support Baseline Values and Assumptions Document*. NASA Technical Publication, TP-2015-218570/REV2. Lyndon B. Johnson Space Center, Houston, Texas, USA: National Aeronautics and Space Administration, 2015. URL: https://ntrs.nasa.gov/api/citations/20210024855/downloads/BVAD_2.15.22-final.pdf.

[27] R. C. van Benthem, W. de Grave, J. van Es, J. Elst, R. Bleuler, and T. Tjiptahardja. *Development of a Mechanically Pumped Fluid Loop for 3–6 kW Payload Cooling*. Technical Report NLR-TP-2009-459. Nationaal Lucht- en Ruimtevaartlaboratorium (NLR), 2010. URL: https://reports.nlr.nl/server/api/core/bitstreams/a17706c4-d297-49ad-8b4a-1b192fe9d10d/content.

[28] H. L. Peabody. *Thermal Design for Spaceflight*. Presentation, Spacecraft Thermal Engineering Course. NASA GSFC - Code 545. Greenbelt, MD, USA, 2022. URL: https://ntrs.nasa.gov/api/citations/20230003714/downloads/Thermal%20Design%20for%20Spaceflight.pptx.pdf.

[29] K. R. Sridhar and M. Gottmann. *Thermal Control Systems for Low-Temperature Heat Rejection on a Lunar Base*. Semiannual Status Report. Tucson, AZ 85721, 1992. URL: https://ntrs.nasa.gov/api/citations/19920011027/downloads/19920011027.pdf.

[30] A. J. Hanford and M. K. Ewert. *Advanced Active Thermal Control Systems Architecture Study*. Technical Memorandum 104822. Houston, Texas, USA: NASA Lyndon B. Johnson Space Center, 1996. URL: https://ntrs.nasa.gov/api/citations/19970001606/downloads/19970001606.pdf.

[31] Japan Aerospace Exploration Agency (JAXA) and Toyota Motor Corporation. *Pressurized Rover Mission Concepts and Expected Capabilities*. 2019. URL: https://humans-in-space.jaxa.jp/biz-lab/news/item/004353/Appendix.pdf.

[32] National Aeronautics and Space Administration. *Space Exploration Vehicle Concept Fact Sheet*. 2011. URL: https://www.nasa.gov/wp-content/uploads/2015/08/464826main_sev_factsheet_508.pdf?emrc=0855ca.

[33] B. Kosobud, M. Perry, and N. Schwanbeck. *What to Expect During In-flight Operations*. NASA Technical Reports Server, Accessed: March 2026. 2017. URL: https://ntrs.nasa.gov/api/citations/20170000487/downloads/20170000487.pdf.

[34] R. L. Cataldo and G. L. Bennett. «U.S. Space Radioisotope Power Systems and Applications: Past, Present and Future». In: *Radioisotopes – Applications in Physical Sciences*. Ed. by N. Singh. InTech, 2011. Chap. 18. URL: https://ntrs.nasa.gov/api/citations/20120000731/downloads/20120000731.pdf.

[35] G. Chin et al. «Lunar Reconnaissance Orbiter Overview: The Instrument Suite and Mission». In: *Space Science Reviews* (2007). DOI: 10.1007/s11214-007-9153-y.

[36] LROC Team, Arizona State University. *QuickMap – Lunar Reconnaissance Orbiter Camera*. https://quickmap.lroc.asu.edu. 2024.

[37] H. Brown, A. Boyd, B. Denevi, M. Henriksen, M. Manheim, M. Robinson, E. Speyerer, and R. Wagner. «Resource potential of lunar permanently shadowed regions». In: *Icarus* (2022). DOI: 10.1016/j.icarus.2021.114874.

[38] H. Bhatt, P. Chauhan, and P. Solanki. «Compositional mapping and the evolutionary history of Mare Tranquillitatis». In: *Journal of Earth System Science* 129 (2020), p. 45. DOI: 10.1007/s12040-019-1302-7.

[39] NASA Manned Spacecraft Center. *Apollo 11 Mission Report*. Tech. rep. MSC-00171. Houston, Texas, 1969. URL: https://www.nasa.gov/wp-content/uploads/static/apollo50th/pdf/A11_MissionReport.pdf.

[40] W. Whittaker. *Technologies Enabling Exploration of Skylights, Lava Tubes and Caves*. Tech. rep. NNX11AR42G. Pittsburgh, Pennsylvania: Astrobotic Technology, 2012. URL: https://www.nasa.gov/wp-content/uploads/2017/07/niac_2011_phasei_whittaker_lavatubesandcaves_tagged.pdf.

[41] F. Zhang, M.-H. Zhu, R. Bugiolacchi, Q. Huang, G. R. Osinski, L. Xiao, and Y. L. Zou. «Diversity of basaltic lunar volcanism associated with buried impact structures: Implications for intrusive and extrusive events». In: *Icarus* 307 (2018), pp. 216–234. DOI: 10.1016/j.icarus.2017.10.039. URL: https://www.sciencedirect.com/science/article/pii/S0019103516306790.

[42] L. Qiao, J. Head, L. Wilson, J. Chen, and Z. Ling. «Mare Domes in Mare Tranquillitatis: Identification, Characterization, and Implications for Their Origin». In: *Journal of Geophysical Research: Planets* 126 (2021). DOI: 10.1029/2021JE006888.

[43] NASA. *NASA Provides Update on Artemis III Moon Landing Regions*. https://www.nasa.gov/news-release/nasa-provides-update-on-artemis-iii-moon-landing-regions/. 2022.

[44] Council of Europe – Committee for the Prevention of Torture (CPT). *Living Space per Prisoner in Prison Establishments: CPT Standards*. Tech. rep. CPT/Inf (2015) 44. 2015. URL: https://rm.coe.int/16806cc447.

[45] MathWorks. *fmincon*. MATLAB Optimization Toolbox documentation. 2024. URL: https://www.mathworks.com/help/optim/ug/fmincon.html.

[46] The MathWorks, Inc. *Constrained Nonlinear Optimization Algorithms*. MATLAB Optimization Toolbox Documentation. 2024. URL: https://it.mathworks.com/help/optim/ug/constrained-nonlinear-optimization-algorithms.html.

[47] MathWorks. *MultiStart*. MATLAB Global Optimization Toolbox documentation. 2024. URL: https://www.mathworks.com/help/gads/multistart.html.

[48] W. Liu, G. Wan, J. Liu, and D. Cong. «Path Planning for Lunar Rovers in Dynamic Environments: An Autonomous Navigation Framework Enhanced by Digital Twin-Based A*-D3QN». In: *Aerospace* 12.6 (2025), p. 517. DOI: 10.3390/aerospace12060517. URL: https://www.mdpi.com/2226-4310/12/6/517.

Acknowledgements

Desidero esprimere la mia sincera gratitudine ai miei professori, Giuseppe Palaia e Karim Abu Salem, per la loro preziosa guida, il costante sostegno e le opportunità che mi hanno offerto al di fuori del contesto della tesi. Desidero inoltre ringraziare la mia famiglia e i miei amici per essere sempre stati al mio fianco e per aver reso questi anni di studio più sereni e leggeri. Il loro sostegno, la loro pazienza e il loro affetto hanno rappresentato per me un punto di riferimento prezioso in ogni momento.